

Generalizations of the Kerr-Newman solution

Contents

1	Topics	703
1.1	ICRANet Participants	703
1.2	Ongoing collaborations	703
1.3	Students	703
2	Brief description	705
3	Introduction	707
4	The general static vacuum solution	709
4.1	Line element and field equations	709
4.2	Static solution	711
5	Stationary generalization	713
5.1	Ernst representation	713
5.2	Representation as a nonlinear sigma model	714
5.3	Representation as a generalized harmonic map	716
5.4	Dimensional extension	720
5.5	The general solution	723
6	Motion of charged test particles in Reissner–Nordström spacetime	727
6.1	Introduction	727
6.2	Circular motion	729
6.2.1	Coulomb potential approximation	732
6.3	Black holes	732
6.3.1	Stability	745
6.4	Naked singularities	747
6.4.1	Case $\epsilon > 1$	753
6.4.2	Case $0 < \epsilon < 1$	754
6.4.3	Case $\epsilon < -1$	755
6.4.4	Case $-1 < \epsilon < 0$	757
6.4.5	Stability	758
6.5	Velocity of test particles in a RN naked singularity	762
6.6	Remarks	768
7	Equatorial circular motion in Kerr spacetime	773
7.1	Introduction	773

7.2	Circular orbits	774
7.3	Black holes	776
7.3.1	Stability	781
7.4	Naked singularities	788
7.4.1	The case $a \geq (3\sqrt{3}/4)M$	789
7.4.2	The case $M < a < (3\sqrt{3}/4)M$	796
7.4.3	Orbits with zero angular momentum	805
7.4.4	Summary of the naked singularity and black hole cases	807
7.5	Remarks	809
8	On the search for interior solutions	813
8.1	The Hartle-Thorne metrics	815
8.2	Fock's approximate method	819
8.3	Matching with the Kerr solution	821
8.4	The exact Quevedo-Mashhoon metric	823
9	Matching with an interior solution	827
9.0.1	Matching conditions	828
9.0.2	An interior solution	831
9.1	Concluding remarks	835
	Bibliography	837

1 Topics

- Generalizations of the Kerr-Newman solution

1.1 ICRANet Participants

- Donato Bini
- Andrea Geralico
- Roy Kerr
- Remo Ruffini

1.2 Ongoing collaborations

- Hernando Quevedo (Universidad Nacional Autónoma de México, Mexico)

1.3 Students

- Kuantay Boshkayev (IRAP PhD, Kazakhstan)
- Orlando Luongo (Rome University PhD, Italy)
- Daniela Pugliese (Rome University PhD, Italy)

2 Brief description

One of the most important metrics in general relativity is the Kerr-Newman solution that describes the gravitational and electromagnetic fields of a rotating charged mass. For astrophysical purposes, however, it is necessary to take into account the effects due to the moment of inertia of the object. To attack this problem we have derived exact solutions of Einstein-Maxwell equations which possess an infinite set of gravitational and electromagnetic multipole moments.

To study the physical relevance of such solutions in the context of relativistic astrophysics we analyze the particular case of a rotating mass with an arbitrary quadrupole moment. The investigation of the motion of test particles in the corresponding gravitational field shows that the quadrupole drastically affects the structure of spacetime. In particular, effects associated with repulsive gravity take place due to the presence of naked singularities. We perform an analytical study of circular motion around naked singularities in the specific case of the Reissner-Nordström and the Kerr spacetime. To study the physical effects of repulsive gravity in an invariant manner we propose to use the eigenvalues of the curvature tensor which are scalar quantities and provide physically reasonable results in the case of naked singularities with black hole counterparts as well as in the case of naked singularities generated by higher multipole moments.

We study the problem of matching stationary and axisymmetric exterior and interior solutions, and propose an invariant approach based upon the use of curvature invariants. We study the problem of the interior solution for a rotating mass with quadrupole moment. In particular, we show that the approximate interior Hartle-Thorne solution can be matched with an approximate exterior solution which is a particular case of the exact Mashhoon-Quevedo exterior solution. The quadrupole parameter is interpreted as an additional degree of freedom that can be used to attack the problem of finding physically reasonable interior solutions. We study the Zipoy-Voorhees static solution and find a particular interior counterpart which is described by a static perfect fluid with quadrupole moment.

3 Introduction

It is hard to overemphasize the importance of the Kerr geometry not only for general relativity itself, but also for the very fundamentals of physics. It assumes this position as being the most physically relevant rotating generalization of the static Schwarzschild geometry. Its charged counterpart, the Kerr-Newman solution, representing the exterior gravitational and electromagnetic fields of a charged rotating object, is an exact solution of the Einstein-Maxwell equations.

Its line element in Boyer-Lindquist coordinates can be written as

$$\begin{aligned}
 ds^2 = & \frac{r^2 - 2Mr + a^2 + Q^2}{r^2 + a^2 \cos^2 \theta} (dt - a \sin^2 \theta d\phi)^2 \\
 & - \frac{\sin^2 \theta}{r^2 + a^2 \cos^2 \theta} [(r^2 + a^2) d\phi - a dt]^2 \\
 & - \frac{r^2 + a^2 \cos^2 \theta}{r^2 - 2Mr + a^2 + Q^2} dr^2 - (r^2 + a^2 \cos^2 \theta) d\theta^2, \quad (3.0.1)
 \end{aligned}$$

where M is the total mass of the object, $a = J/M$ is the specific angular momentum, and Q is the electric charge. In this particular coordinate system, the metric functions do not depend on the coordinates t and ϕ , indicating the existence of two Killing vector fields $\xi^I = \partial_t$ and $\xi^{II} = \partial_\phi$ which represent the properties of stationarity and axial symmetry, respectively.

An important characteristic of this solution is that the source of gravity is surrounded by two horizons situated at a distance

$$r_{\pm} = M \pm \sqrt{M^2 - a^2 - Q^2} \quad (3.0.2)$$

from the origin of coordinates. Inside the interior horizon, r_- , a ring singularity is present which, however, cannot be observed by any observer situated outside the exterior horizon. If the condition $M^2 < a^2 + Q^2$ is satisfied, no horizons are present and the Kerr-Newman spacetime represents the exterior field of a naked singularity.

Despite of its fundamental importance in general relativity, and its theoretical and mathematical interest, this solution has not been especially useful for describing astrophysical phenomena, first of all, because observed astrophysical objects do not possess an appreciable net electric charge. Furthermore, the limiting Kerr metric takes into account the mass and the rotation, but does not consider the moment of inertia of the object. For astrophysi-

cal applications it is, therefore, necessary to use more general solutions with higher multipole moments which are due not only to the rotation of the body but also to its shape. This means that even in the limiting case of a static spacetime, a solution is needed that takes into account possible deviations from spherical symmetry.

4 The general static vacuum solution

In general relativity, stationary axisymmetric solutions of Einstein's equations [1] play a crucial role for the description of the gravitational field of astrophysical objects. In particular, the black hole solutions and their generalizations that include Maxwell fields are contained within this class.

This type of exact solutions has been the subject of intensive research during the past few decades. In particular, the number of known exact solutions drastically increased after Ernst [2] discovered an elegant representation of the field equations that made it possible to search for their symmetries. These studies lead finally to the development of solution generating techniques [1] which allow us to find new solutions, starting from a given seed solution. In particular, solutions with an arbitrary number of multipole moments for the mass and angular momentum were derived in [3] and used to describe the gravitational field of rotating axially symmetric distributions of mass.

The first analysis of stationary axially symmetric gravitational fields was carried out by Weyl [4] in 1917, soon after the formulation of general relativity. In particular, Weyl discovered that in the static limit the main part of the vacuum field equations reduces to a single linear differential equation. The corresponding general solution can be written in cylindrical coordinates as an infinite sum with arbitrary constant coefficients. A particular choice of the coefficients leads to the subset of asymptotically flat solutions which is the most interesting from a physical point of view. In this section we review the main properties of stationary axisymmetric gravitational fields. In particular, we show explicitly that the main field equations in vacuum can be represented as the equations of a nonlinear sigma model in which the base space is the 4-dimensional spacetime and the target space is a 2-dimensional conformally Euclidean space.

4.1 Line element and field equations

Although there exist in the literature many suitable coordinate systems, stationary axisymmetric gravitational fields are usually described in cylindrical coordinates (t, ρ, z, φ) . Stationarity implies that t can be chosen as the time coordinate and the metric does not depend on time, i.e. $\partial g_{\mu\nu} / \partial t = 0$. Consequently, the corresponding timelike Killing vector has the components δ_t^μ .

A second Killing vector field is associated to the axial symmetry with respect to the axis $\rho = 0$. Then, choosing φ as the azimuthal angle, the metric satisfies the conditions $\partial g_{\mu\nu}/\partial\varphi = 0$, and the components of the corresponding spacelike Killing vector are δ_φ^μ .

Using further the properties of stationarity and axial symmetry, together with the vacuum field equations, for a general metric of the form $g_{\mu\nu} = g_{\mu\nu}(\rho, z)$, it is possible to show that the most general line element for this type of gravitational fields can be written in the Weyl-Lewis-Papapetrou form as [4, 5, 6]

$$ds^2 = f(dt - \omega d\varphi)^2 - f^{-1} \left[e^{2\gamma}(d\rho^2 + dz^2) + \rho^2 d\varphi^2 \right], \quad (4.1.1)$$

where f , ω and γ are functions of ρ and z , only. After some rearrangements which include the introduction of a new function $\Omega = \Omega(\rho, z)$ by means of

$$\rho \partial_\rho \Omega = f^2 \partial_z \omega, \quad \rho \partial_z \Omega = -f^2 \partial_\rho \omega, \quad (4.1.2)$$

the vacuum field equations $R_{\mu\nu} = 0$ can be shown to be equivalent to the following set of partial differential equations

$$\frac{1}{\rho} \partial_\rho(\rho \partial_\rho f) + \partial_z^2 f + \frac{1}{f} [(\partial_\rho \Omega)^2 + (\partial_z \Omega)^2 - (\partial_\rho f)^2 - (\partial_z f)^2] = 0, \quad (4.1.3)$$

$$\frac{1}{\rho} \partial_\rho(\rho \partial_\rho \Omega) + \partial_z^2 \Omega - \frac{2}{f} (\partial_\rho f \partial_\rho \Omega + \partial_z f \partial_z \Omega) = 0, \quad (4.1.4)$$

$$\partial_\rho \gamma = \frac{\rho}{4f^2} [(\partial_\rho f)^2 + (\partial_\rho \Omega)^2 - (\partial_z f)^2 - (\partial_z \Omega)^2], \quad (4.1.5)$$

$$\partial_z \gamma = \frac{\rho}{2f^2} (\partial_\rho f \partial_z f + \partial_\rho \Omega \partial_z \Omega). \quad (4.1.6)$$

It is clear that the field equations for γ can be integrated by quadratures, once f and Ω are known. For this reason, the equations (4.1.3) and (4.1.4) for f and Ω are usually considered as the main field equations for stationary axisymmetric vacuum gravitational fields. In the following subsections we will focus on the analysis of the main field equations, only. It is interesting to mention that this set of equations can be geometrically interpreted in the context of nonlinear sigma models [7].

Let us consider the special case of static axisymmetric fields. This corresponds to metrics which, apart from being axially symmetric and independent of the time coordinate, are invariant with respect to the transformation $\varphi \rightarrow -\varphi$ (i.e. rotations with respect to the axis of symmetry are not allowed). Consequently, the corresponding line element is given by (4.1.1) with $\omega = 0$,

and the field equations can be written as

$$\partial_\rho^2 \psi + \frac{1}{\rho} \partial_\rho \psi + \partial_z^2 \psi = 0, \quad f = \exp(2\psi), \quad (4.1.7)$$

$$\partial_\rho \gamma = \rho \left[(\partial_\rho \psi)^2 - (\partial_z \psi)^2 \right], \quad \partial_z \gamma = 2\rho \partial_\rho \psi \partial_z \psi. \quad (4.1.8)$$

We see that the main field equation (4.1.7) corresponds to the linear Laplace equation for the metric function ψ .

4.2 Static solution

The general solution of Laplace's equation is known and, if we demand additionally asymptotic flatness, we obtain the Weyl solution which can be written as [4, 1]

$$\psi = \sum_{n=0}^{\infty} \frac{a_n}{(\rho^2 + z^2)^{\frac{n+1}{2}}} P_n(\cos \theta), \quad \cos \theta = \frac{z}{\sqrt{\rho^2 + z^2}}, \quad (4.2.1)$$

where a_n ($n = 0, 1, \dots$) are arbitrary constants, and $P_n(\cos \theta)$ represents the Legendre polynomials of degree n . The expression for the metric function γ can be calculated by quadratures by using the set of first order differential equations (4.1.8). Then

$$\gamma = - \sum_{n,m=0}^{\infty} \frac{a_n a_m (n+1)(m+1)}{(n+m+2)(\rho^2 + z^2)^{\frac{n+m+2}{2}}} (P_n P_m - P_{n+1} P_{m+1}). \quad (4.2.2)$$

Since this is the most general static, axisymmetric, asymptotically flat vacuum solution, it must contain all known solution of this class. In particular, one of the most interesting special solutions which is Schwarzschild's spherically symmetric black hole spacetime must be contained in this class. To see this, we must choose the constants a_n in such a way that the infinite sum (4.2.1) converges to the Schwarzschild solution in cylindric coordinates. But, or course, this representation is not the most appropriate to analyze the interesting physical properties of Schwarzschild's metric.

In fact, it turns out that to investigate the properties of solutions with multipole moments it is more convenient to use prolate spheroidal coordinates (t, x, y, φ) in which the line element can be written as

$$ds^2 = f dt^2 - \frac{\sigma^2}{f} \left[e^{2\gamma} (x^2 - y^2) \left(\frac{dx^2}{x^2 - 1} + \frac{dy^2}{1 - y^2} \right) + (x^2 - 1)(1 - y^2) d\varphi^2 \right]$$

where

$$x = \frac{r_+ + r_-}{2\sigma}, \quad (x^2 \geq 1), \quad y = \frac{r_+ - r_-}{2\sigma}, \quad (y^2 \leq 1) \quad (4.2.3)$$

$$r_{\pm}^2 = \rho^2 + (z \pm \sigma)^2, \quad \sigma = \text{const}, \quad (4.2.4)$$

and the metric functions are f , ω , and γ depend on x and y , only. In this coordinate system, the general static solution which is also asymptotically flat can be expressed as

$$f = \exp(2\psi), \quad \psi = \sum_{n=0}^{\infty} (-1)^{n+1} q_n P_n(y) Q_n(x), \quad q_n = \text{const}$$

where $P_n(y)$ are the Legendre polynomials, and $Q_n(x)$ are the Legendre functions of second kind. In particular,

$$P_0 = 1, \quad P_1 = y, \quad P_2 = \frac{1}{2}(3y^2 - 1), \dots$$

$$Q_0 = \frac{1}{2} \ln \frac{x+1}{x-1}, \quad Q_1 = \frac{1}{2} x \ln \frac{x+1}{x-1} - 1,$$

$$Q_2 = \frac{1}{2}(3x^2 - 1) \ln \frac{x+1}{x-1} - \frac{3}{2}x, \dots$$

The corresponding function γ can be calculated by quadratures and its general expression has been explicitly derived in [8]. The most important special cases contained in this general solution are the Schwarzschild metric

$$\psi = -q_0 P_0(y) Q_0(x), \quad \gamma = \frac{1}{2} \ln \frac{x^2 - 1}{x^2 - y^2},$$

and the Erez-Rosen metric [9]

$$\psi = -q_0 P_0(y) Q_0(x) - q_2 P_2(y) Q_2(x), \quad \gamma = \frac{1}{2} \ln \frac{x^2 - 1}{x^2 - y^2} + \dots$$

In the last case, the constant parameter q_2 turns out to determine the quadrupole moment. In general, the constants q_n represent an infinite set of parameters that determines an infinite set of mass multipole moments.

5 Stationary generalization

The solution generating techniques [12] can be applied, in particular, to any static seed solution in order to obtain the corresponding stationary generalization. One of the most powerful techniques is the inverse method (ISM) developed by Belinski and Zakharov [13]. We used a particular case of the ISM, which is known as the Hoenselaers–Kinnersley–Xanthopoulos (HKX) transformation to derive the stationary generalization of the general static solution in prolate spheroidal coordinates.

5.1 Ernst representation

In the general stationary case ($\omega \neq 0$) with line element

$$ds^2 = f(dt - \omega d\varphi)^2 - \frac{\sigma^2}{f} \left[e^{2\gamma} (x^2 - y^2) \left(\frac{dx^2}{x^2 - 1} + \frac{dy^2}{1 - y^2} \right) + (x^2 - 1)(1 - y^2) d\varphi^2 \right]$$

it is useful to introduce the the Ernst potentials

$$E = f + i\Omega, \quad \xi = \frac{1 - E}{1 + E},$$

where the function Ω is now determined by the equations

$$\sigma(x^2 - 1)\Omega_x = f^2\omega_y, \quad \sigma(1 - y^2)\Omega_y = -f^2\omega_x.$$

Then, the main field equations can be represented in a compact and symmetric form:

$$(\xi\xi^* - 1) \left\{ [(x^2 - 1)\xi_x]_x + [(1 - y^2)\xi_y]_y \right\} = 2\xi^* [(x^2 - 1)\xi_x^2 + (1 - y^2)\xi_y^2].$$

This equation is invariant with respect to the transformation $x \leftrightarrow y$. Then, since the particular solution

$$\xi = \frac{1}{x} \rightarrow \Omega = 0 \rightarrow \omega = 0 \rightarrow \gamma = \frac{1}{2} \ln \frac{x^2 - 1}{x^2 - y^2}$$

represents the Schwarzschild spacetime, the choice $\zeta^{-1} = y$ is also an exact solution. Furthermore, if we take the linear combination $\zeta^{-1} = c_1x + c_2y$ and introduce it into the field equation, we obtain the new solution

$$\zeta^{-1} = \frac{\sigma}{M}x + i\frac{a}{M}y, \quad \sigma = \sqrt{M^2 - a^2},$$

which corresponds to the Kerr metric in prolate spheroidal coordinates.

In the case of the Einstein-Maxwell theory, the main field equations can be expressed as

$$(\zeta\zeta^* - \mathcal{F}\mathcal{F}^* - 1)\nabla^2\zeta = 2(\zeta^*\nabla\zeta - \mathcal{F}^*\nabla\mathcal{F})\nabla\zeta,$$

$$(\zeta\zeta^* - \mathcal{F}\mathcal{F}^* - 1)\nabla^2\mathcal{F} = 2(\zeta^*\nabla\zeta - \mathcal{F}^*\nabla\mathcal{F})\nabla\mathcal{F}$$

where ∇ represents the gradient operator in prolate spheroidal coordinates. Moreover, the gravitational potential ζ and the electromagnetic \mathcal{F} Ernst potential are defined as

$$\zeta = \frac{1 - f - i\Omega}{1 + f + i\Omega}, \quad \mathcal{F} = 2\frac{\Phi}{1 + f + i\Omega}.$$

The potential Φ can be shown to be determined uniquely by the electromagnetic potentials A_t and A_φ . One can show that if ζ_0 is a vacuum solution, then the new potential

$$\zeta = \zeta_0\sqrt{1 - e^2}$$

represents a solution of the Einstein-Maxwell equations with effective electric charge e . This transformation is known in the literature as the Harrison transformation [10]. Accordingly, the Kerr-Newman solution in this representation acquires the simple form

$$\zeta = \frac{\sqrt{1 - e^2}}{\frac{\sigma}{M}x + i\frac{a}{M}y}, \quad e = \frac{Q}{M}, \quad \sigma = \sqrt{M^2 - a^2 - Q^2}.$$

In this way, it is very easy to generalize any vacuum solution to include the case of electric charge. More general transformations of this type can be used in order to generate solutions with any desired set of gravitational and electromagnetic multipole moments [11].

5.2 Representation as a nonlinear sigma model

Consider two (pseudo)-Riemannian manifolds (M, γ) and (N, G) of dimension m and n , respectively. Let M be coordinatized by x^a , and N by X^μ , so that the metrics on M and N can be, in general, smooth functions of the corresponding coordinates, i.e., $\gamma = \gamma(x)$ and $G = G(X)$. A harmonic map is a

smooth map $X : M \rightarrow N$, or in coordinates $X : x \mapsto X$ so that X becomes a function of x , and the X 's satisfy the motion equations following from the action [14]

$$S = \int d^m x \sqrt{|\gamma|} \gamma^{ab}(x) \partial_a X^\mu \partial_b X^\nu G_{\mu\nu}(X), \quad (5.2.1)$$

which sometimes is called the “energy” of the harmonic map X . The straightforward variation of S with respect to X^μ leads to the motion equations

$$\frac{1}{\sqrt{|\gamma|}} \partial_b \left(\sqrt{|\gamma|} \gamma^{ab} \partial_a X^\mu \right) + \Gamma_{\nu\lambda}^\mu \gamma^{ab} \partial_a X^\nu \partial_b X^\lambda = 0, \quad (5.2.2)$$

where $\Gamma_{\nu\lambda}^\mu$ are the Christoffel symbols associated to the metric $G_{\mu\nu}$ of the target space N . If $G_{\mu\nu}$ is a flat metric, one can choose Cartesian-like coordinates such that $G_{\mu\nu} = \eta_{\mu\nu} = \text{diag}(\pm 1, \dots, \pm 1)$, the motion equations become linear, and the corresponding sigma model is linear. This is exactly the case of a bosonic string on a flat background in which the base space is the 2-dimensional string world-sheet. In this case the action (5.2.1) is usually referred to as the Polyakov action [16].

Consider now the case in which the base space M is a stationary axisymmetric spacetime. Then, γ^{ab} , $a, b = 0, \dots, 3$, can be chosen as the Weyl-Lewis-Papapetrou metric (4.1.1), i.e.

$$\gamma_{ab} = \begin{pmatrix} f & 0 & 0 & -f\omega \\ 0 & -f^{-1}e^{2k} & 0 & 0 \\ 0 & 0 & -f^{-1}e^{2k} & 0 \\ -f\omega & 0 & 0 & f\omega^2 - \rho^2 f^{-1} \end{pmatrix}. \quad (5.2.3)$$

Let the target space N be 2-dimensional with metric $G_{\mu\nu} = (1/2)f^{-2}\delta_{\mu\nu}$, $\mu, \nu = 1, 2$, and let the coordinates on N be $X^\mu = (f, \Omega)$. Then, it is straightforward to show that the action (5.2.1) becomes

$$S = \int \mathcal{L} dt d\phi d\rho dz, \quad \mathcal{L} = \frac{\rho}{2f^2} \left[(\partial_\rho f)^2 + (\partial_z f)^2 + (\partial_\rho \Omega)^2 + (\partial_z \Omega)^2 \right], \quad (5.2.4)$$

and the corresponding motion equations (5.2.2) are identical to the main field equations (4.1.3) and (4.1.4).

Notice that the field equations can also be obtained from (5.2.4) by a direct variation with respect to f and Ω . This interesting result was obtained originally by Ernst [2], and is the starting point of what today is known as the Ernst representation of the field equations.

The above result shows that stationary axisymmetric gravitational fields can be described as a $(4 \rightarrow 2)$ -nonlinear harmonic map, where the base space is the spacetime of the gravitational field and the target space corresponds to a 2-dimensional conformally Euclidean space. A further analy-

sis of the target space shows that it can be interpreted as the quotient space $SL(2, R)/SO(2)$ [15], and the Lagrangian (5.2.4) can be written explicitly [17] in terms of the generators of the Lie group $SL(2, R)$. Harmonic maps in which the target space is a quotient space are usually known as nonlinear sigma models [14].

The form of the Lagrangian (5.2.4) with two gravitational field variables, f and Ω , depending on two coordinates, ρ and z , suggests a representation as a harmonic map with a 2-dimensional base space. In string theory, this is an important fact that allows one to use the conformal invariance of the base space metric to find an adequate representation for the set of classical solutions. This, in turn, facilitates the application of the canonical quantization procedure. Unfortunately, this is not possible for the Lagrangian (5.2.4). Indeed, if we consider γ^{ab} as a 2-dimensional metric that depends on the parameters ρ and z , the diagonal form of the Lagrangian (5.2.4) implies that $\sqrt{|\gamma|}\gamma^{ab} = \delta^{ab}$. Clearly, this choice is not compatible with the factor ρ in front of the Lagrangian. Therefore, the reduced gravitational Lagrangian (5.2.4) cannot be interpreted as corresponding to a $(2 \rightarrow n)$ -harmonic map. Nevertheless, we will show in the next section that a modification of the definition of harmonic maps allows us to “absorb” the unpleasant factor ρ in the metric of the target space, and to use all the advantages of a 2-dimensional base space.

Notice that the representation of stationary fields as a nonlinear sigma model becomes degenerate in the limiting case of static fields. Indeed, the underlying geometric structure of the $SL(2, R)/SO(2)$ nonlinear sigma models requires that the target space be 2-dimensional, a condition which is not satisfied by static fields. We will see below that by using a dimensional extension of generalized sigma models, it will be possible to treat the special static case, without affecting the underlying geometric structure.

The analysis performed in this section for stationary axisymmetric fields can be generalized to include any gravitational field containing two commuting Killing vector fields [1]. This is due to the fact that for this class of gravitational fields it is always possible to find the corresponding Ernst representation in which the Lagrangian contains only two gravitational variables which depend on only two spacetime coordinates.

5.3 Representation as a generalized harmonic map

Consider two (pseudo-)Riemannian manifolds (M, γ) and (N, G) of dimension m and n , respectively. Let x^a and X^μ be coordinates on M and N , respectively. This coordinatization implies that in general the metrics γ and G become functions of the corresponding coordinates. Let us assume that not only γ but also G can explicitly depend on the coordinates x^a , i.e. let $\gamma = \gamma(x)$ and $G = G(X, x)$. This simple assumption is the main aspect of our

generalization which, as we will see, lead to new and nontrivial results.

A smooth map $X : M \rightarrow N$ will be called an $(m \rightarrow n)$ -generalized harmonic map if it satisfies the Euler-Lagrange equations

$$\frac{1}{\sqrt{|\gamma|}} \partial_b \left(\sqrt{|\gamma|} \gamma^{ab} \partial_a X^\mu \right) + \Gamma^\mu_{\nu\lambda} \gamma^{ab} \partial_a X^\nu \partial_b X^\lambda + G^{\mu\lambda} \gamma^{ab} \partial_a X^\nu \partial_b G_{\lambda\nu} = 0, \quad (5.3.1)$$

which follow from the variation of the generalized action

$$S = \int d^m x \sqrt{|\gamma|} \gamma^{ab}(x) \partial_a X^\mu \partial_b X^\nu G_{\mu\nu}(X, x), \quad (5.3.2)$$

with respect to the fields X^μ . Here the Christoffel symbols, determined by the metric $G_{\mu\nu}$, are calculated in the standard manner, without considering the explicit dependence on x . Notice that the new ingredient in this generalized definition of harmonic maps, i.e., the term $G_{\mu\nu}(X, x)$ in the Lagrangian density implies that we are taking into account the “interaction” between the base space M and the target space N . This interaction leads to an extra term in the motion equations, as can be seen in (5.3.1). It turns out that this interaction is the result of the effective presence of the gravitational field.

Notice that the limiting case of generalized linear harmonic maps is much more complicated than in the standard case. Indeed, for the motion equations (5.3.1) to become linear it is necessary that the conditions

$$\gamma^{ab} (\Gamma^\mu_{\nu\lambda} \partial_b X^\lambda + G^{\mu\lambda} \partial_b G_{\lambda\nu}) \partial_a X^\nu = 0, \quad (5.3.3)$$

be satisfied. One could search for a solution in which each term vanishes separately. The choice of a (pseudo-)Euclidean target metric $G_{\mu\nu} = \eta_{\mu\nu}$, which would imply $\Gamma^\mu_{\nu\lambda} = 0$, is not allowed, because it would contradict the assumption $\partial_b G_{\mu\nu} \neq 0$. Nevertheless, a flat background metric in curvilinear coordinates could be chosen such that the assumption $G^{\mu\lambda} \partial_b G_{\mu\nu} = 0$ is fulfilled, but in this case $\Gamma^\mu_{\nu\lambda} \neq 0$ and (5.3.3) cannot be satisfied. In the general case of a curved target metric, conditions (5.3.3) represent a system of m first order nonlinear partial differential equations for $G_{\mu\nu}$. Solutions to this system would represent linear generalized harmonic maps. The complexity of this system suggests that this special type of maps is not common.

As we mentioned before, the generalized action (5.3.2) includes an interaction between the base space N and the target space M , reflected on the fact that $G_{\mu\nu}$ depends explicitly on the coordinates of the base space. Clearly, this interaction must affect the conservation laws of the physical systems we attempt to describe by means of generalized harmonic maps. To see this explicitly we calculate the covariant derivative of the generalized Lagrangian density

$$\mathcal{L} = \sqrt{|\gamma|} \gamma^{ab}(x) \partial_a X^\mu \partial_b X^\nu G_{\mu\nu}(X, x), \quad (5.3.4)$$

and replace in the result the corresponding motion equations (5.3.1). Then, the final result can be written as

$$\nabla_b \tilde{T}_a^b = -\frac{\partial \mathcal{L}}{\partial x^a} \quad (5.3.5)$$

where \tilde{T}_a^b represents the canonical energy-momentum tensor

$$\tilde{T}_a^b = \frac{\partial \mathcal{L}}{\partial(\partial_b X^\mu)} (\partial_a X^\mu) - \delta_a^b \mathcal{L} = 2\sqrt{\gamma} G_{\mu\nu} \left(\gamma^{bc} \partial_a X^\mu \partial_c X^\nu - \frac{1}{2} \delta_a^b \gamma^{cd} \partial_c X^\mu \partial_d X^\nu \right). \quad (5.3.6)$$

The standard conservation law is recovered only when the Lagrangian does not depend explicitly on the coordinates of the base space. Even if we choose a flat base space $\gamma_{ab} = \eta_{ab}$, the explicit dependence of the metric of the target space $G_{\mu\nu}(X, x)$ on x generates a term that violates the standard conservation law. This term is due to the interaction between the base space and the target space which, consequently, is one of the main characteristics of the generalized harmonic maps introduced in this work.

An alternative and more general definition of the energy-momentum tensor is by means of the variation of the Lagrangian density with respect to the metric of the base space, i.e.

$$T_{ab} = \frac{\delta \mathcal{L}}{\delta \gamma^{ab}}. \quad (5.3.7)$$

A straightforward computation shows that for the action under consideration here we have that $\tilde{T}_{ab} = 2T_{ab}$ so that the generalized conservation law (5.3.5) can be written as

$$\nabla_b T_a^b + \frac{1}{2} \frac{\partial \mathcal{L}}{\partial x^a} = 0. \quad (5.3.8)$$

For a given metric on the base space, this represents in general a system of m differential equations for the “fields” X^μ which must be satisfied “on-shell”.

If the base space is 2-dimensional, we can use a reparametrization of x to choose a conformally flat metric, and the invariance of the Lagrangian density under arbitrary Weyl transformations to show that the energy-momentum tensor is traceless, $T_a^a = 0$.

In Section 5.1 we described stationary, axially symmetric, gravitational fields as a $(4 \rightarrow 2)$ -nonlinear sigma model. There it was pointed out the convenience of having a 2-dimensional base space in analogy with string theory. Now we will show that this can be done by using the generalized harmonic maps defined above.

Consider a $(2 \rightarrow 2)$ -generalized harmonic map. Let $x^a = (\rho, z)$ be the coordinates on the base space M , and $X^\mu = (f, \Omega)$ the coordinates on the target space N . In the base space we choose a flat metric and in the target

space a conformally flat metric, i.e.

$$\gamma_{ab} = \delta_{ab} \quad \text{and} \quad G_{\mu\nu} = \frac{\rho}{2f^2} \delta_{\mu\nu} \quad (a, b = 1, 2; \mu, \nu = 1, 2). \quad (5.3.9)$$

A straightforward computation shows that the generalized Lagrangian (5.3.4) coincides with the Lagrangian (5.2.4) for stationary axisymmetric fields, and that the equations of motion (5.3.1) generate the main field equations (4.1.3) and (4.1.4).

For the sake of completeness we calculate the components of the energy-momentum tensor $T_{ab} = \delta\mathcal{L}/\delta\gamma^{ab}$. Then

$$T_{\rho\rho} = -T_{zz} = \frac{\rho}{4f^2} \left[(\partial_\rho f)^2 + (\partial_\rho \Omega)^2 - (\partial_z f)^2 - (\partial_z \Omega)^2 \right], \quad (5.3.10)$$

$$T_{\rho z} = \frac{\rho}{2f^2} (\partial_\rho f \partial_z f + \partial_\rho \Omega \partial_z \Omega). \quad (5.3.11)$$

This tensor is traceless due to the fact that the base space is 2-dimensional. It satisfies the generalized conservation law (5.3.8) on-shell:

$$\frac{dT_{\rho\rho}}{d\rho} + \frac{dT_{\rho z}}{dz} + \frac{1}{2} \frac{\partial\mathcal{L}}{\partial\rho} = 0, \quad (5.3.12)$$

$$\frac{dT_{\rho z}}{d\rho} - \frac{dT_{\rho\rho}}{dz} = 0. \quad (5.3.13)$$

Incidentally, the last equation coincides with the integrability condition for the metric function k , which is identically satisfied by virtue of the main field equations. In fact, as can be seen from Eqs.(4.1.5,4.1.6) and (5.3.10,5.3.11), the components of the energy-momentum tensor satisfy the relationships $T_{\rho\rho} = \partial_\rho k$ and $T_{\rho z} = \partial_z k$, so that the conservation law (5.3.13) becomes an identity. Although we have eliminated from the starting Lagrangian (5.2.4) the variable k by applying a Legendre transformation on the Einstein-Hilbert Lagrangian (see [17] for details) for this type of gravitational fields, the formalism of generalized harmonic maps seems to retain the information about k at the level of the generalized conservation law.

The above results show that stationary axisymmetric spacetimes can be represented as a $(2 \rightarrow 2)$ -generalized harmonic map with metrics given as in (5.3.9). It is also possible to interpret the generalized harmonic map given above as a generalized string model. Although the metric of the base space M is Euclidean, we can apply a Wick rotation $\tau = i\rho$ to obtain a Minkowski-like structure on M . Then, M represents the world-sheet of a bosonic string in which τ measures the time and z is the parameter along the string. The string is "embedded" in the target space N whose metric is conformally flat and explicitly depends on the time parameter τ . We will see in the next sec-

tion that this embedding becomes more plausible when the target space is subject to a dimensional extension. In the present example, it is necessary to apply a Wick rotation in order to interpret the base space as a string world-sheet. This is due to the fact that both coordinates ρ and z are spatial coordinates. However, this can be avoided by considering other classes of gravitational fields with timelike Killing vector fields; examples will be given below.

The most studied solutions belonging to the class of stationary axisymmetric fields are the asymptotically flat solutions. Asymptotic flatness imposes conditions on the metric functions which in the cylindrical coordinates used here can be formulated in the form

$$\lim_{x^a \rightarrow \infty} f = 1 + O\left(\frac{1}{x^a}\right), \quad \lim_{x^a \rightarrow \infty} \omega = c_1 + O\left(\frac{1}{x^a}\right), \quad \lim_{x^a \rightarrow \infty} \Omega = O\left(\frac{1}{x^a}\right) \quad (5.3.14)$$

where c_1 is an arbitrary real constant which can be set to zero by appropriately choosing the angular coordinate φ . If we choose the domain of the spatial coordinates as $\rho \in [0, \infty)$ and $z \in (-\infty, +\infty)$, from the asymptotic flatness conditions it follows that the coordinates of the target space N satisfy the boundary conditions

$$\dot{X}^\mu(\rho, -\infty) = 0 = \dot{X}^\mu(\rho, \infty), \quad X'^\mu(\rho, -\infty) = 0 = X'^\mu(\rho, \infty) \quad (5.3.15)$$

where the dot stands for a derivative with respect to ρ and the prime represents derivation with respect to z . These relationships are known in string theory [16] as the Dirichlet and Neumann boundary conditions for open strings, respectively, with the extreme points situated at infinity. We thus conclude that if we assume ρ as a “time” parameter for stationary axisymmetric gravitational fields, an asymptotically flat solution corresponds to an open string with endpoints attached to D -branes situated at plus and minus infinity in the z -direction.

5.4 Dimensional extension

In order to further analyze the analogy between gravitational fields and bosonic string models, we perform an arbitrary dimensional extension of the target space N , and study the conditions under which this dimensional extension does not affect the field equations of the gravitational field. Consider an $(m \rightarrow D)$ -generalized harmonic map. As before we denote by $\{x^a\}$ the coordinates on M . Let $\{X^\mu, X^\alpha\}$ with $\mu = 1, 2$ and $\alpha = 3, 4, \dots, D$ be the coordinates on N . The metric structure on M is again $\gamma = \gamma(x)$, whereas the metric on N can in general depend on all coordinates of M and N , i.e. $G = G(X^\mu, X^\alpha, x^a)$. The general structure of the corresponding field equations is as given in (5.3.1). They can be divided into one set of equations for X^μ and one set of equations for X^α . According to the results of the last sec-

tion, the class of gravitational fields under consideration can be represented as a $(2 \rightarrow 2)$ -generalized harmonic map so that we can assume that the main gravitational variables are contained in the coordinates X^μ of the target space. Then, the gravitational sector of the target space will be contained in the components $G_{\mu\nu}$ ($\mu, \nu = 1, 2$) of the metric, whereas the components $G_{\alpha\beta}$ ($\alpha, \beta = 3, 4, \dots, D$) represent the sector of the dimensional extension.

Clearly, the set of differential equations for X^μ also contains the variables X^α and its derivatives $\partial_a X^\alpha$. For the gravitational field equations to remain unaffected by this dimensional extension we demand the vanishing of all the terms containing X^α and its derivatives in the equations for X^μ . It is easy to show that this can be achieved by imposing the conditions

$$G_{\mu\alpha} = 0, \quad \frac{\partial G_{\mu\nu}}{\partial X^\alpha} = 0, \quad \frac{\partial G_{\alpha\beta}}{\partial X^\mu} = 0. \quad (5.4.1)$$

That is to say that the gravitational sector must remain completely invariant under a dimensional extension, and the additional sector cannot depend on the gravitational variables, i.e., $G_{\alpha\beta} = G_{\alpha\beta}(X^\gamma, x^a)$, $\gamma = 3, 4, \dots, D$. Furthermore, the variables X^α must satisfy the differential equations

$$\frac{1}{\sqrt{|\gamma|}} \partial_b \left(\sqrt{|\gamma|} \gamma^{ab} \partial_a X^\alpha \right) + \Gamma^\alpha_{\beta\gamma} \gamma^{ab} \partial_a X^\beta \partial_b X^\gamma + G^{\alpha\beta} \gamma^{ab} \partial_a X^\gamma \partial_b G_{\beta\gamma} = 0. \quad (5.4.2)$$

This shows that any given $(2 \rightarrow 2)$ -generalized map can be extended, without affecting the field equations, to a $(2 \rightarrow D)$ -generalized harmonic map.

It is worth mentioning that the fact that the target space N becomes split in two separate parts implies that the energy-momentum tensor $T_{ab} = \delta\mathcal{L}/\delta\gamma^{ab}$ separates into one part belonging to the gravitational sector and a second one following from the dimensional extension, i.e. $T_{ab} = T_{ab}(X^\mu, x) + T_{ab}(X^\alpha, x)$. The generalized conservation law as given in (5.3.8) is satisfied by the sum of both parts.

Consider the example of stationary axisymmetric fields given the metrics (5.3.9). Taking into account the conditions (5.4.1), after a dimensional extension the metric of the target space becomes

$$G = \begin{pmatrix} \frac{\rho}{2f^2} & 0 & 0 & \cdots & 0 \\ 0 & \frac{\rho}{2f^2} & 0 & \cdots & 0 \\ 0 & 0 & G_{33}(X^\alpha, x) & \cdots & G_{3D}(X^\alpha, x) \\ \cdot & \cdot & \cdots & \cdots & \cdots \\ 0 & 0 & G_{D3}(X^\alpha, x) & \cdots & G_{DD}(X^\alpha, x) \end{pmatrix}. \quad (5.4.3)$$

Clearly, to avoid that this metric becomes degenerate we must demand that $\det(G_{\alpha\beta}) \neq 0$, a condition that can be satisfied in view of the arbitrariness of the components of the metric. With the extended metric, the Lagrangian

density gets an additional term

$$\mathcal{L} = \frac{\rho}{2f^2} \left[(\partial_\rho f)^2 + (\partial_z f)^2 + (\partial_\rho \Omega)^2 + (\partial_z \Omega)^2 \right] + \left(\partial_\rho X^\alpha \partial_\rho X^\beta + \partial_z X^\alpha \partial_z X^\beta \right) G_{\alpha\beta}, \quad (5.4.4)$$

which nevertheless does not affect the field equations for the gravitational variables f and Ω . On the other hand, the new fields must be solutions of the extra field equations

$$\left(\partial_\rho^2 + \partial_z^2 \right) X^\alpha + \Gamma^\alpha_{\beta\gamma} \left(\partial_\rho X^\beta \partial_\rho X^\gamma + \partial_z X^\beta \partial_z X^\gamma \right) + G^{\alpha\gamma} \left(\partial_\rho X^\beta \partial_\rho G_{\beta\gamma} + \partial_z X^\beta \partial_z G_{\beta\gamma} \right) = 0. \quad (5.4.5)$$

An interesting special case of the dimensional extension is the one in which the extended sector is Minkowskian, i.e. for the choice $G_{\alpha\beta} = \eta_{\alpha\beta}$ with additional fields X^α given as arbitrary harmonic functions. This choice opens the possibility of introducing a “time” coordinate as one of the additional dimensions, an issue that could be helpful when dealing with the interpretation of gravitational fields in this new representation.

The dimensional extension finds an interesting application in the case of static axisymmetric gravitational fields. As mentioned in Section 4.1, these fields are obtained from the general stationary fields in the limiting case $\Omega = 0$ (or equivalently, $\omega = 0$). If we consider the representation as an $SL(2, R)/SO(2)$ nonlinear sigma model or as a $(2 \rightarrow 2)$ -generalized harmonic map, we see immediately that the limit $\Omega = 0$ is not allowed because the target space becomes 1-dimensional and the underlying metric is undefined. To avoid this degeneracy, we first apply a dimensional extension and only then calculate the limiting case $\Omega = 0$. In the most simple case of an extension with $G_{\alpha\beta} = \delta_{\alpha\beta}$, the resulting $(2 \rightarrow 2)$ -generalized map is described by the metrics $\gamma_{ab} = \delta_{ab}$ and

$$G = \begin{pmatrix} \frac{\rho}{2f^2} & 0 \\ 0 & 1 \end{pmatrix} \quad (5.4.6)$$

where the additional dimension is coordinatized by an arbitrary harmonic function which does not affect the field equations of the only remaining gravitational variable f . This scheme represents an alternative method for exploring static fields on nondegenerate target spaces. Clearly, this scheme can be applied to the case of gravitational fields possessing two hypersurface orthogonal Killing vector fields.

Our results show that a stationary axisymmetric field can be represented as a string “living” in a D -dimensional target space N . The string world-sheet is parametrized by the coordinates ρ and z . The gravitational sector of the target space depends explicitly on the metric functions f and Ω and on the parameter ρ of the string world-sheet. The sector corresponding to the dimensional extension can be chosen as a $(D - 2)$ -dimensional Minkowski space-time with time parameter τ . Then, the string world-sheet is a 2-dimensional

flat hypersurface which is “frozen” along the time τ .

5.5 The general solution

If we take as seed metric the general static solution, the application of two HXK transformations generates a stationary solution with an infinite number of gravitoelectric and gravitomagnetic multipole moments. The HKX method is applied at the level of the Ernst potential from which the metric functions can be calculated by using the definition of the Ernst potential E and the field equations for γ . The resulting expressions in the general case are quite cumbersome. We quote here only the special case in which only an arbitrary quadrupole parameter is present. In this case, the result can be written as

$$\begin{aligned} f &= \frac{R}{L} e^{-2qP_2Q_2}, \\ \omega &= -2a - 2\sigma \frac{\mathcal{M}}{R} e^{2qP_2Q_2}, \\ e^{2\gamma} &= \frac{1}{4} \left(1 + \frac{M}{\sigma}\right)^2 \frac{R}{x^2 - y^2} e^{2\hat{\gamma}}, \end{aligned} \quad (5.5.1)$$

where

$$\begin{aligned} R &= a_+ a_- + b_+ b_-, & L &= a_+^2 + b_+^2, \\ \mathcal{M} &= \alpha x(1 - y^2)(e^{2q\delta_+} + e^{2q\delta_-}) a_+ + y(x^2 - 1)(1 - \alpha^2 e^{2q(\delta_+ + \delta_-)}) b_+, \\ \hat{\gamma} &= \frac{1}{2}(1 + q)^2 \ln \frac{x^2 - 1}{x^2 - y^2} + 2q(1 - P_2)Q_1 + q^2(1 - P_2) \left[(1 + P_2)(Q_1^2 - Q_2^2) \right. \\ &\quad \left. + \frac{1}{2}(x^2 - 1)(2Q_2^2 - 3xQ_1Q_2 + 3Q_0Q_2 - Q_2') \right]. \end{aligned} \quad (5.5.2)$$

Here $P_l(y)$ and $Q_l(x)$ are Legendre polynomials of the first and second kind respectively. Furthermore

$$\begin{aligned} a_{\pm} &= x(1 - \alpha^2 e^{2q(\delta_+ + \delta_-)}) \pm (1 + \alpha^2 e^{2q(\delta_+ + \delta_-)}), \\ b_{\pm} &= \alpha y(e^{2q\delta_+} + e^{2q\delta_-}) \mp \alpha(e^{2q\delta_+} - e^{2q\delta_-}), \\ \delta_{\pm} &= \frac{1}{2} \ln \frac{(x \pm y)^2}{x^2 - 1} + \frac{3}{2}(1 - y^2 \mp xy) + \frac{3}{4}[x(1 - y^2) \mp y(x^2 - 1)] \ln \frac{x - 1}{x + 1}, \end{aligned}$$

the quantity α being a constant

$$\alpha = \frac{\sigma - M}{a}, \quad \sigma = \sqrt{M^2 - a^2}. \quad (5.5.3)$$

The physical significance of the parameters entering this metric can be clar-

ified by calculating the Geroch-Hansen [18, 19] multipole moments

$$M_{2k+1} = J_{2k} = 0, \quad k = 0, 1, 2, \dots \quad (5.5.4)$$

$$M_0 = M, \quad M_2 = -Ma^2 + \frac{2}{15}qM^3 \left(1 - \frac{a^2}{M^2}\right)^{3/2}, \dots \quad (5.5.5)$$

$$J_1 = Ma, \quad J_3 = -Ma^3 + \frac{4}{15}qM^3a \left(1 - \frac{a^2}{M^2}\right)^{3/2}, \dots \quad (5.5.6)$$

The vanishing of the odd gravitoelectric (M_n) and even gravitomagnetic (J_n) multipole moments is a consequence of the symmetry with respect to the equatorial plane. From the above expressions we see that M is the total mass of the body, a represents the specific angular momentum, and q is related to the deviation from spherical symmetry. All higher multipole moments can be shown to depend only on the parameters M , a , and q .

We analyzed the geometric and physical properties of the above solution. The special cases contained in the general solution suggest that it can be used to describe the exterior asymptotically flat gravitational field of rotating body with arbitrary quadrupole moment. This is confirmed by the analysis of the motion of particles on the equatorial plane. The quadrupole moment turns out to drastically change the geometric structure of spacetime as well as the motion of particles, especially near the gravitational source.

We investigated in detail the properties of the Quevedo-Mashhoon (QM) spacetime which is a generalization of Kerr spacetime, including an arbitrary quadrupole. Our results show [20] that a deviation from spherical symmetry, corresponding to a non-zero electric quadrupole, completely changes the structure of spacetime. A similar behavior has been found in the case of the Erez-Rosen spacetime. In fact, a naked singularity appears that affects the ergosphere and introduces regions where closed timelike curves are allowed. Whereas in the Kerr spacetime the ergosphere corresponds to the boundary of a simply-connected region of spacetime, in the present case the ergosphere is distorted by the presence of the quadrupole and can even become transformed into non simply-connected regions. All these changes occur near the naked singularity which is situated at $x = 1$, a value that corresponds to the radial distance $r = M + \sqrt{M^2 - a^2}$ in Boyer-Lindquist coordinates. In the limiting case $a/M > 1$, the multipole moments and the metric become complex, indicating that the physical description breaks down. Consequently, the extreme Kerr black hole represents the limit of applicability of the QM spacetime.

Since standard astrophysical objects satisfy the condition $a/M < 1$, we can conclude that the QM metric can be used to describe their exterior gravitational field. Two alternative situations are possible. If the characteristic radius of the body is greater than the critical distance $M + \sqrt{M^2 - a^2}$, i.e.

$x > 1$, the exterior solution must be matched with an interior solution in order to describe the entire spacetime. If, however, the characteristic radius of the body is smaller than the critical distance $M + \sqrt{M^2 - a^2}$, the QM metric describes the field of a naked singularity.

The presence of a naked singularity leads to interesting consequences in the motion of test particles. For instance, repulsive effects can take place in a region very closed to the naked singularity. In that region stable circular orbits can exist. The limiting case of static particle is also allowed. Due to the complexity of the above solution, the investigation of naked singularities can be performed only numerically. To illustrate the effects of repulsive gravity analytically, we used the simplest possible case which corresponds to the Reissner-Nordström spacetime.

6 Motion of charged test particles in Reissner–Nordström spacetime

6.1 Introduction

Let us consider the background of a static gravitational source of mass M and charge Q , described by the Reissner–Nordström (RN) line element in standard spherical coordinates

$$ds^2 = -\frac{\Delta}{r^2}dt^2 + \frac{r^2}{\Delta}dr^2 + r^2(d\theta^2 + \sin^2\theta d\phi^2), \quad (6.1.1)$$

where $\Delta = (r - r_+)(r - r_-)$ and $r_{\pm} = M \pm \sqrt{M^2 - Q^2}$ are the radii of the outer and inner horizon, respectively. Furthermore, the associated electromagnetic potential and field are

$$A = \frac{Q}{r}dt, \quad F = dA = -\frac{Q}{r^2}dt \wedge dr, \quad (6.1.2)$$

respectively.

The motion of a test particle of charge q and mass μ moving in a RN background (6.1.1) is described by the following Lagrangian density:

$$\mathcal{L} = \frac{1}{2}g_{\alpha\beta}\dot{x}^\alpha\dot{x}^\beta + \epsilon A_\alpha\dot{x}^\alpha, \quad (6.1.3)$$

where A_α are the components of the electromagnetic 4-potential, the dot represents differentiation with respect to the proper time, and the parameter $\epsilon = q/\mu$ is the specific charge of the test particle. The equations of motion of the test particle can be derived from Eq. (6.1.3) by using the Euler–Lagrange equation. Then,

$$\dot{x}^\alpha\nabla_\alpha\dot{x}^\beta = \epsilon F_\gamma^\beta\dot{x}^\gamma, \quad (6.1.4)$$

where $F_{\alpha\beta} \equiv A_{\alpha,\beta} - A_{\beta,\alpha}$.

Since the Lagrangian density (6.1.3) does not depend explicitly on the vari-

ables t and ϕ , the following two conserved quantities exist

$$p_t \equiv \frac{\partial \mathcal{L}}{\partial \dot{t}} = - \left(\frac{\Delta}{r^2} \dot{t} + \frac{\epsilon Q}{r} \right) = - \frac{E}{\mu}, \quad (6.1.5)$$

$$p_\phi = \frac{\partial \mathcal{L}}{\partial \dot{\phi}} = r^2 \sin^2 \theta \dot{\phi} = \frac{L}{\mu}, \quad (6.1.6)$$

where L and E are respectively the angular momentum and energy of the particle as measured by an observer at rest at infinity. Moreover, to study the motion of charged test particles in the RN spacetime it is convenient to use the fact if the initial position and the tangent vector of the trajectory of the particle lie on a plane that contains the center of the body, then the entire trajectory must lie on this plane. Without loss of generality we may therefore restrict ourselves to the study of equatorial trajectories with $\theta = \pi/2$.

On the equatorial plane $\theta = \pi/2$, the motion equations can be reduced to the form $\dot{r}^2 + V^2 = E^2/\mu^2$ which describes the motion inside an effective potential V . Then, we define the potential

$$V_\pm = \frac{E^\pm}{\mu} = \frac{\epsilon Q}{r} \pm \sqrt{\left(1 + \frac{L^2}{\mu^2 r^2}\right) \left(1 - \frac{2M}{r} + \frac{Q^2}{r^2}\right)} \quad (6.1.7)$$

as the value of E/μ that makes r into a “turning point” ($V = E/\mu$); in other words, the value of E/μ at which the (radial) kinetic energy of the particle vanishes [80, 21, 22, 23]. The effective potential with positive (negative) sign corresponds to the solution with

$$\lim_{r \rightarrow \infty} E^+ = +\mu; \quad \left(\lim_{r \rightarrow \infty} E^- = -\mu \right),$$

where

$$E^+(L, \epsilon, r) \geq E^-(L, \epsilon, r), \quad (6.1.8)$$

and the following relation holds:

$$E^+(L, \epsilon, r) = -E^-(L, -\epsilon, r). \quad (6.1.9)$$

The behavior of the effective potential strongly depends on the sign of ϵQ ; in particular in the case of $\epsilon Q < 0$, negative energy states for the solution E^+ can exist (see also [24, 25, 26, 27, 28, 29, 30]).

The problem of finding exact solutions of the motion equations of test particles moving in a RN spacetime has been widely studied in literature in many contexts and ways. For a recent discussion we mention the works [24, 25, 26, 27, 28, 29, 30]. In particular, in a recent paper [24] the full set of analytical solutions of the motion equations for electrically and magnetically charged test particles is discussed in terms of the Weierstrass (γ , σ and

ζ) functions. The general structure of the geodesics was discussed and a classification of their types was proposed. Remarkably, analytical solutions are found in the case of a central RN source not only with constant electric charge, but also with constant magnetic charge. It is interesting to notice that if either the test particle or the central body possesses both types of charge, it turns out that the motion is no longer confined to a plane. In the present work, we consider only equatorial circular orbits around a central RN source with constant electric charge. Instead of solving directly the equations of motion, we explore the properties of the effective potential function associated to the motion. Thus, we discuss and propose a classification of the equatorial orbits in terms of the two constants of motion: the energy E/μ and the orbital angular momentum $L/(\mu M)$. In fact, we focus our attention on some peculiar features of the circular motion and the physics around black holes and naked singularities. In particular, we are interested in exploring the possibility of distinguishing between black holes and naked singularities by studying the motion of circular test particles. In this sense, the present work complements and is different from previous studies [24, 25, 26, 27, 28, 29, 30].

In a previous work [31, 32], we analyzed the dynamics of the RN spacetime by studying the motion of neutral test particles for which the effective potential turns out to coincide with V_+ as given in Eq.(6.1.7) with $\epsilon = 0$. We will see that in the case of charged test particles the term $\epsilon Q/r$ drastically changes the behavior of the effective potential, and leads to several possibilities which must be analyzed in the case of black holes and naked singularities. In particular, we will show that for particles moving along circular orbits there exist stability regions whose geometric structure clearly distinguishes naked singularities from black holes (see also [33, 34] and [35, 36]). The plan of this paper is the following: In Sec. 6.2 we investigate the behavior of the effective potential and the conditions for the motion of positive and negative charged test particles moving on circular orbits around the central charged mass. This section also contains a brief analysis of the Coulomb approximation of the effective potential. In Sec. 6.3, we will consider the black hole case while in Sec. 6.4 we shall focus on the motion around naked singularities. The conclusions are in Sec. 6.6.

6.2 Circular motion

The circular motion of charged test particles is governed by the behavior of the effective potential (6.1.7). In this work, we will mainly consider the special case of a positive solution V_+ for the potential in order to be able to compare our results with those obtained in the case of neutral test particles analyzed in [31, 32]. Thus, the radius of circular orbits and the corresponding values of the energy E and the angular momentum L are given by the extrema of the function V_+ . Therefore, the conditions for the occurrence of circular orbits

are:

$$\frac{dV_+}{dr} = 0, \quad V_+ = \frac{E^+}{\mu}. \quad (6.2.1)$$

When possible, to simplify the notation we will drop the subindex (+) so that, for example, $V = E/\mu$ will denote the positive effective potential solution. Solving Eq. (6.2.1) with respect to L , we find the specific angular momentum

$$\frac{(L^\pm)^2}{\mu^2} = \frac{r^2}{2\Sigma^2} \left[2(Mr - Q^2)\Sigma + \epsilon^2 Q^2 \Delta \pm Q\Delta \sqrt{\epsilon^2 (4\Sigma + \epsilon^2 Q^2)} \right], \quad (6.2.2)$$

where $\Sigma \equiv r^2 - 3Mr + 2Q^2$, of the test particle on a circular orbit of radius r . The corresponding energy can be obtained by introducing the expression for the angular momentum into Eq. (6.1.7). Then, we obtain

$$\frac{E^\pm}{\mu} = \frac{\epsilon Q}{r} + \frac{\Delta \sqrt{2\Sigma + \epsilon^2 Q^2 \pm Q \sqrt{\epsilon^2 (4\Sigma + \epsilon^2 Q^2)}}}{\sqrt{2}r|\Sigma|}. \quad (6.2.3)$$

The sign in front of the square root should be chosen in accordance with the physical situation. This point will be clarified below by using the formalism of orthonormal frames.

An interesting particular orbit is the one in which the particle is located at rest as seen by an observer at infinity, i.e., $L = 0$. These “orbits” are therefore characterized by the following conditions

$$L = 0, \quad \frac{dV}{dr} = 0. \quad (6.2.4)$$

[83]. Solving Eq. (6.2.4) for $Q \neq 0$ and $\epsilon \neq 0$, we find the following radius

$$r_s^\pm \equiv \frac{(\epsilon^2 - 1) Q^2 M}{\epsilon^2 Q^2 - M^2} \pm \sqrt{\frac{\epsilon^2 Q^4 (\epsilon^2 - 1) (M^2 - Q^2)}{(\epsilon^2 Q^2 - M^2)^2}}. \quad (6.2.5)$$

Table 6.1 shows the explicit values of all possible radii for different values of the ratio Q/M . A particle located at $r = r_s$ with angular momentum $L = 0$ will have the energy (see also [37, 38, 83, 39, 40, 41, 42])

$$\frac{E_s^\pm}{\mu} \equiv \frac{1}{Q} \left(\sqrt{\frac{M^2 - Q^2}{\epsilon^2 - 1}} + \frac{\epsilon}{\frac{\epsilon^2 - 1}{\epsilon^2 Q^2 - M^2} \pm \sqrt{\frac{\epsilon^2 (M^2 - Q^2) (\epsilon^2 - 1)}{(\epsilon^2 Q^2 - M^2)^2}}} \right). \quad (6.2.6)$$

The minimum radius for a stable circular orbit occurs at the inflection points

$0 < Q < M$		$Q = M$		$Q > M$	
ϵ	Radius	ϵ	Radius	ϵ	Radius
$\epsilon > M/Q$	$r = r_s^+$	$\epsilon = 1$	$r > M$	$-M/Q < \epsilon < 0$	$r = r_s^-$
				$\epsilon = -M/Q$	$r = Q^2/(2M)$
				$-1 < \epsilon \leq -M/Q$	$r = r_s^+$
				$\epsilon = 0$	$r = Q^2/M$
				$0 < \epsilon < M/Q$	$r = r_s^+$

Table 6.1: Radii of the “orbits” characterized by the conditions $L = 0$ and $dV/dr = 0$.

of the effective potential function; thus, we must solve the equation

$$\frac{d^2V}{dr^2} = 0, \quad (6.2.7)$$

for the orbit radius r , using the expression (6.2.2) for the angular momentum L . From Eq. (6.2.1) and Eq. (6.2.7) we find that the radius of the last stable circular orbit and the angular momentum of this orbit are related by the following equations

$$\begin{aligned} (L^2 + Q^2 - 1) r^6 - 6L^2 r^5 + 6L^2 (1 + Q^2) r^4 - 2L^2 (2L^2 + 5Q^2) r^3 \\ + L^2 (3L^2 + 3L^2 Q^2 + 3Q^4) r^2 - 6L^4 Q^2 r + 2L^4 Q^4 = 0, \end{aligned}$$

and

$$Q^2 r^2 - r^3 + L^2 (2Q^2 - 3r + r^2) + Qr^3 \sqrt{\frac{(L^2 + r^2)(Q^2 - 2r + r^2)}{r^4}} \epsilon = 0, \quad (6.2.8)$$

where in order to simplify the notation we introduced the normalized quantities $L \rightarrow L/(M/\mu)$, $r \rightarrow r/M$, and $Q \rightarrow Q/M$. Equation (6.2.8) depends on the test particle specific charge ϵ via the function L as given in Eq. (6.2.2). It is possible to solve Eq. (6.2.8) for the last stable circular orbit radius as a function of the free parameter L . We find the expression

$$\begin{aligned} \frac{(L_{\text{lsc}}^\pm)^2}{\mu^2} = & \frac{r^2}{2[2Q^4 + 3Q^2 r(r - 2M) - (2r - 3M)r^2]} \\ & \left[2Q^2(5M - 3r)r - 3Q^4 - r^2[6M^2 + (r - 6M)r] \right. \\ & \left. \pm \sqrt{9Q^2 + (r - 6M)r} (Q^2 + (r - 2M)r)^{3/2} \right] \end{aligned} \quad (6.2.9)$$

for the angular momentum of last stable circular orbit. Eq. (6.2.9) can be

substituted in Eq. (6.2.8) to find the radius of the last stable circular orbit.

6.2.1 Coulomb potential approximation

Consider the case of a charged particle moving in the Coulomb potential

$$U(r) = \frac{Q}{r}.$$

This means that we are considering the motion described by the following effective potential

$$V_+ = \frac{E^+}{\mu} = \frac{\epsilon Q}{r} + \sqrt{1 + \frac{L^2}{\mu^2 r^2}}, \quad (6.2.10)$$

where $\epsilon Q < 0$. The Coulomb approximation is interesting for our further analysis because it corresponds to the limiting case for large values of the radial coordinate r [cf. Eq.(6.1.7)].

Circular orbits are therefore situated at $r = r_c$ with

$$r_c = \sqrt{\frac{L^2}{\mu^2} \left(\frac{L^2}{\epsilon^2 Q^2} - 1 \right)} \quad \text{and} \quad \frac{L^2}{\mu^2} \geq \epsilon^2 Q^2, \quad (6.2.11)$$

and in the case $\epsilon = 0$ with $Q > 0$, circular orbits exist in all $r > 0$ for $L = 0$. We conclude that in this approximation circular orbits always exist with orbital radius r_c and angular momentum satisfying the condition $|L|/\mu \geq |\epsilon Q|$. For the last stable circular orbit situated at $r = r_{\text{lsc}}$ we find

$$r_{\text{lsc}} = 0 \quad \text{with} \quad \frac{E^+(r_{\text{lsc}})}{\mu} = 0 \quad \text{and} \quad \frac{|L|}{\mu} = |\epsilon Q|. \quad (6.2.12)$$

This means that, in the approximation of the Coulomb potential, all the circular orbits are stable, including the limiting case of a particle at rest on the origin of coordinates.

Furthermore, Eqs. (6.2.11–6.2.12) show that, in contrast with the general RN case, for a charged particle moving in a Coulomb potential only positive or null energy solutions can exist. See Fig. 6.1 where the potential (6.2.10) is plotted as a function of the orbital radius for different values of the angular momentum.

6.3 Black holes

In the case of a black hole ($M^2 > Q^2$) the two roots V_{\pm} of the effective potential are plotted as a function of the ratio r/M in Fig. 6.2 for a fixed value of

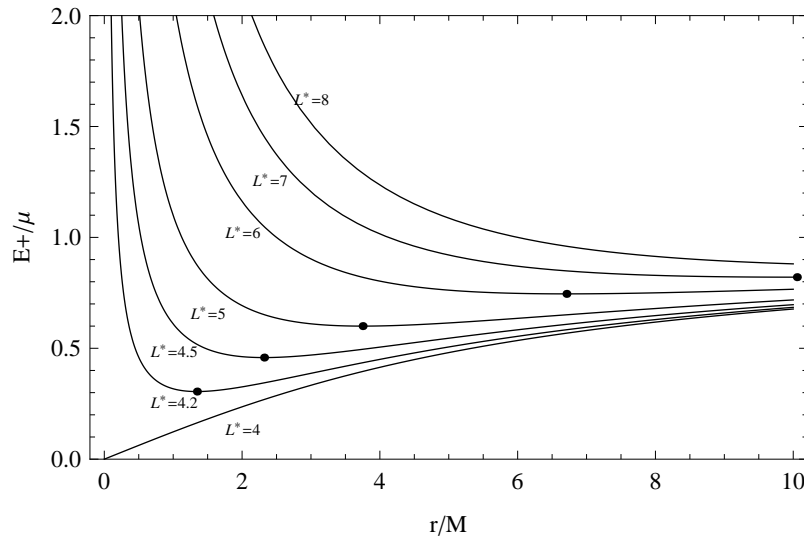


Figure 6.1: Effective potential for a charged test particle with $\epsilon = -2$ moving in a Coulomb potential with $Q/M = 2$ for different values of the momentum $L^* \equiv L/(\mu M)$. The points indicate the minima of the potential. In particular, for $L^* = |\epsilon Q|/M$ the potential vanishes on the origin $r = 0$ (see text).

the charge-to-mass ratio of the test particle and different values of the angular momentum $L/(M\mu)$ (see also [43, 44, 45, 46, 47, 48]). Notice the presence of negative energy states for the positive solution $V_+ = E^+/\mu$ of the effective potential function. Negative energy states for V_+ are possible only in the case $\epsilon Q < 0$. In particular, the largest region in which the V_+ solution has negative energy states is

$$M + \sqrt{M^2 - Q^2} < r \leq M + \sqrt{M^2 - Q^2(1 - \epsilon^2)} \quad (6.3.1)$$

and corresponds to the limiting case of vanishing angular momentum ($L = 0$). For $L \neq 0$ this region becomes smaller and decreases as L increases. For a given value of the orbit radius, say r_0 , such that $r_0 < M + \sqrt{M^2 - Q^2(1 - \epsilon^2)}$, the angular momentum of the test particle must be chosen within the interval

$$0 < \frac{L^2}{\mu^2} < r_0^2 \left(\frac{\epsilon^2 Q^2}{r_0^2 - 2Mr_0 + Q^2} - 1 \right) \quad (6.3.2)$$

for a region with negative energy states to exist. This behavior is illustrated in Fig. 6.2.

Fig. 6.3 shows the positive solution V_+ of the effective potential for different values of the momentum and for positive and negative charged particles. In particular, we note that, at fixed Q/M for a particle with $|\epsilon| < 1$, in the case $\epsilon Q > 0$ the stable orbit radius is larger than in the case of attractive

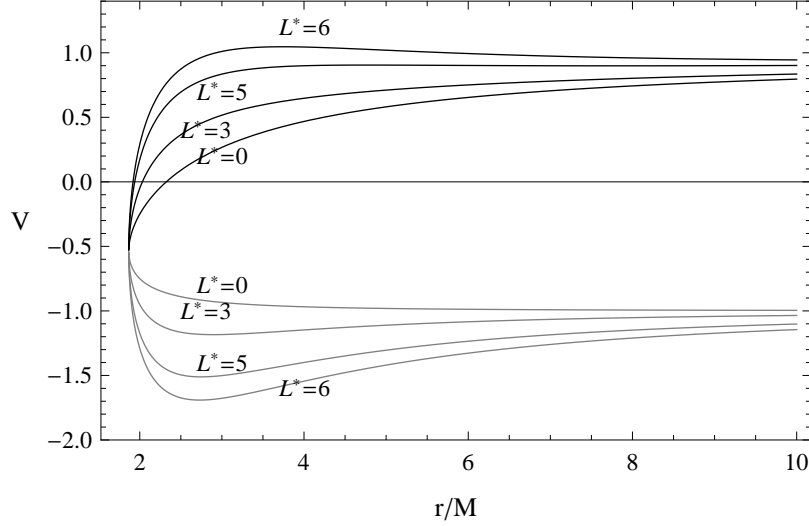


Figure 6.2: The effective potential as a function of r/M for a charged particle of charge-to-mass ratio $\epsilon \equiv q/\mu$ moving in a Reissner–Nordström black hole of charge Q and mass M . The graphic shows the positive E^+/μ (black curves) and negative roots E^-/μ (gray curves) of the effective potential for $Q/M = 0.5$, $\epsilon = -2$, and different values of the momentum $L^* \equiv L/(M\mu)$. The outer horizon is located at $r_+ \equiv M + \sqrt{M^2 - Q^2} \approx 1.87M$. Note the presence of negative energy states for the positive roots.

electromagnetic interaction, i. e., $\epsilon Q < 0$. In Fig. 6.4, the potential V_+ of an extreme black hole is plotted for different, positive and negative values of the test particle with charge-to-mass ratio ϵ . In this case, it is clear that the magnitude of the energy increases as the magnitude of the specific charge of the particle ϵ increases.

As mentioned in Sec. 6.2, in the case of the positive solution for the effective potential the conditions for the existence of circular orbits

$$\dot{r} = 0, \quad V = \frac{E}{\mu}, \quad \frac{dV}{dr} = 0. \quad (6.3.3)$$

lead to Eqs.(6.2.2) and (6.2.3) in which the selection of the (\pm) sign inside the square root should be done properly. To clarify this point we consider explicitly the equation of motion for a charged particle in the gravitational field of a RN black hole.

$$a(U)^\alpha = \epsilon F_\beta^\alpha U^\beta, \quad (6.3.4)$$

where $a(U) = \nabla_U U$ is the particle's 4-acceleration. Introducing the orthonormal frame

$$e_{\hat{t}} = \frac{r}{\Delta^{1/2}} \partial_t, \quad e_{\hat{r}} = \frac{\Delta^{1/2}}{r} \partial_r, \quad e_{\hat{\theta}} = \frac{1}{r} \partial_\theta, \quad e_{\hat{\phi}} = \frac{1}{r \sin \theta} \partial_\phi, \quad (6.3.5)$$

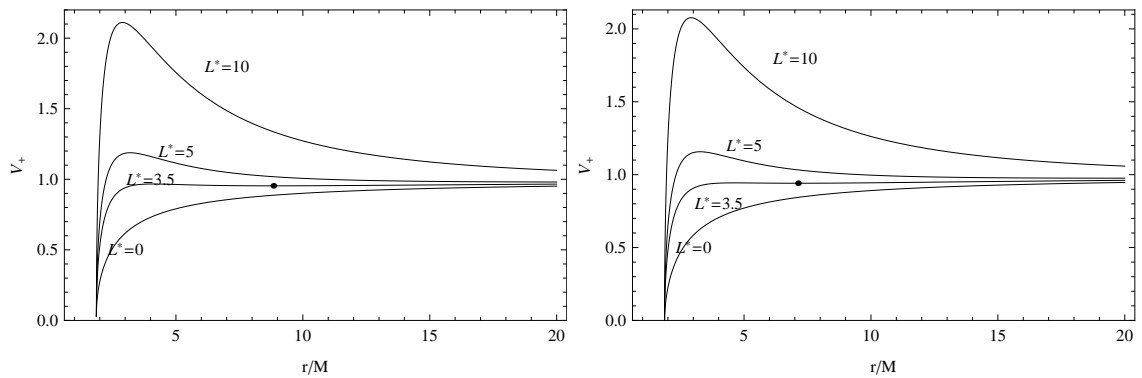


Figure 6.3: The effective potential V_+ for a charged particle of charge-to-mass ratio, $\epsilon = q/\mu$, moving in a Reissner-Nordström spacetime of charge Q and mass M with charge-to-mass ratio $Q/M = 0.5$ is plotted as a function of the radial coordinate r/M for different values of the angular momentum $L^* \equiv L/(M\mu)$. The outer horizon is located at $r_+ \approx 1.87M$. In the graphic on the left with $\epsilon = 0.1$, the effective potential for $L^* \approx 3.5$ has a minimum $V_{min} \approx 0.954$ at $r_{min} \approx 8.84M$. In the graphic on the right with $\epsilon = -0.1$, the minimum $V_{min} \approx 0.94$ is located at $r_{min} \approx 7.13M$ for $L^* \approx 3.5$.

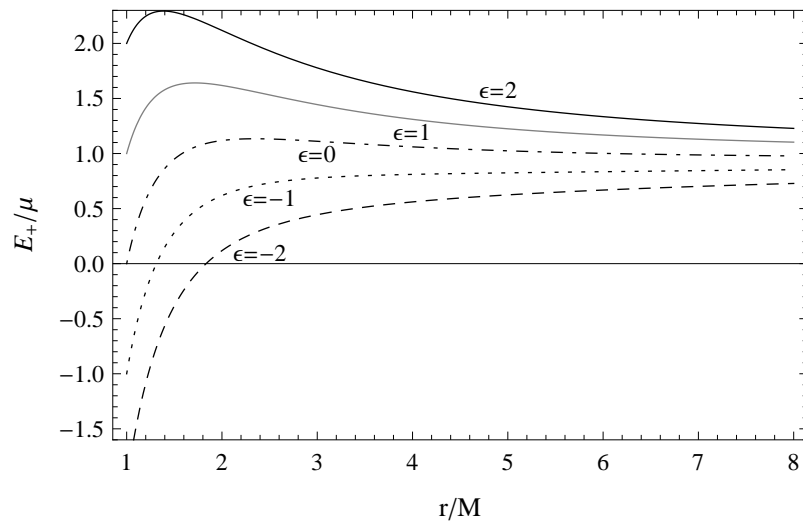


Figure 6.4: The effective potential V_+ is plotted as a function of r/M for a charged test particle with specific charge $\epsilon = q/\mu$ moving in the field of a Reissner-Nordström extreme black hole ($Q = M$). Here $L/(M\mu) = 4$, and the effective potential is plotted for different values of ϵ . The outer horizon is located at $r_+ \equiv M + \sqrt{M^2 - Q^2} = M$. Note the presence of negative energy states for particles with negative ϵ .

with dual

$$\omega^{\hat{t}} = \frac{\Delta^{1/2}}{r} dt, \quad \omega^{\hat{r}} = \frac{r}{\Delta^{1/2}} dr, \quad \omega^{\hat{\theta}} = r d\theta, \quad \omega^{\hat{\phi}} = r \sin \theta d\phi, \quad (6.3.6)$$

the tangent to a (timelike) spatially circular orbit u^α can be expressed as

$$u = \Gamma(\partial_t + \zeta \partial_\phi) = \gamma \left(e_{\hat{t}} + \nu e_{\hat{\phi}} \right),$$

where Γ and γ are normalization factors

$$\Gamma^2 = (-g_{tt} - \zeta^2 g_{\phi\phi})^{-1} \quad \text{and} \quad \gamma^2 = (1 - \nu^2)^{-1},$$

which guarantees that $u_\alpha u^\alpha = -1$. Here ζ is the angular velocity with respect to infinity and ν is the “local proper linear velocity” as measured by an observer associated with the orthonormal frame. The angular velocity ζ is related to the local proper linear velocity by

$$\zeta = \sqrt{\frac{-g_{tt}}{g_{\phi\phi}}} \nu.$$

Since only the radial component of the 4-velocity is non-vanishing, Eq. (6.3.4) can be written explicitly as

$$0 = \gamma(\nu^2 - \nu_g^2) + \frac{\nu_g \epsilon Q}{\zeta_g r^2}, \quad (6.3.7)$$

where

$$\zeta_g = \pm \frac{\sqrt{Mr - Q^2}}{r^2}, \quad \nu_g = \sqrt{\frac{Mr - Q^2}{\Delta}}. \quad (6.3.8)$$

This equation gives the values of the particle linear velocity $\nu = \pm \nu_\epsilon^\pm$ which are compatible with a given value of ϵQ on a circular orbit of radius r , i. e.,

$$\nu_\epsilon^\pm = \nu_g \sqrt{1 - \frac{Q^2 \epsilon^2}{2r^4 \zeta_g^2} \pm \frac{Q}{r^2 \zeta_g \nu_g} \sqrt{\frac{\epsilon^2}{\gamma_g^2} + \frac{Q^2 \epsilon^4 \nu_g^2}{4r^4 \zeta_g^2}}}, \quad (6.3.9)$$

where

$$\gamma_g = \left(\frac{\Delta}{r^2 - 3Mr + 2Q^2} \right)^{1/2},$$

and

$$\gamma_\epsilon^\pm = (1 - \nu_\epsilon^{\pm 2})^{-1/2}. \quad (6.3.10)$$

In the limiting case of a neutral particle ($\epsilon = 0$), Eq.(6.3.7) implies that the linear velocity of the particle is ν_g .

We introduce the limiting value of the parameter ϵ corresponding to a particle at rest, $v = 0$, in Eq. (6.3.7), i. e.,

$$\epsilon_0 = v_g \zeta_g \frac{r^2}{Q} = \frac{Mr - Q^2}{Q\sqrt{\Lambda}}. \quad (6.3.11)$$

By introducing this quantity into Eq. (6.3.7), one gets the following equivalent relation

$$\frac{\epsilon}{\epsilon_0} = \gamma \left(1 - \frac{v^2}{v_g^2} \right), \quad (6.3.12)$$

whose solution (6.3.9) can be conveniently rewritten as

$$v_\epsilon^\pm = v_g \left[\Lambda \pm \sqrt{\Lambda^2 - 1 + (\epsilon/\epsilon_0)^2} \right]^{1/2}, \quad (6.3.13)$$

where

$$\Lambda = 1 - \frac{v_g^2}{2} \left(\frac{\epsilon}{\epsilon_0} \right)^2. \quad (6.3.14)$$

Moreover, from Eq. (6.3.12) it follows that $\epsilon < 0$ implies that $v^2 > v_g^2$ (because ϵ_0 is always positive for $r > r_+$), so that the allowed solutions for v can exist only for $r \geq r_\gamma^+$, where

$$r_\gamma^+ \equiv \frac{1}{2} \left(3M + \sqrt{9M^2 - 8Q^2} \right), \quad (6.3.15)$$

the equality corresponding to $v_g = 1$. In this case, the solutions of Eq. (6.3.7) are given by $v = \pm v_\epsilon^+$.

For $\epsilon > 0$, instead, solutions can exist also for $r_+ < r < r_\gamma^+$. The situation strongly depends on the considered range of values of ϵ and is summarized below.

Equation (6.3.13) gives the following conditions for the existence of velocities

$$\Lambda^2 - 1 + (\epsilon/\epsilon_0)^2 \geq 0, \quad (6.3.16)$$

$$\Lambda \pm \sqrt{\Lambda^2 - 1 + (\epsilon/\epsilon_0)^2} \geq 0. \quad (6.3.17)$$

The second condition, Eq. (6.3.17), is satisfied by

$$r \geq r_l \equiv \frac{3M}{2} + \frac{1}{2} \sqrt{9M^2 - 8Q^2 - \epsilon^2 Q^2}. \quad (6.3.18)$$

Moreover for $Q = M$ and $\epsilon = 1$ it is $\Lambda + \sqrt{\Lambda^2 - 1 + (\epsilon/\epsilon_0)^2} \geq 0$ when $M < r < (3/2)M$. However it is also possible to show that condition Eq. (6.2.1) is

satisfied for $0 < Q < M$ and $\epsilon > 0$ only in the range $r \geq r_l$.

Requiring that the argument of the square root be nonnegative implies

$$\epsilon \leq \epsilon_l \equiv \frac{\sqrt{9M^2 - 8Q^2}}{Q}. \quad (6.3.19)$$

The condition (6.3.17) will be discussed later.

From the equation of motion (6.3.12) it follows that the velocity vanishes for $\epsilon/\epsilon_0 = 1$, i. e., for [cf. Eq.(6.2.5)]

$$r = r_s \equiv \frac{Q^2}{\epsilon^2 Q^2 - M^2} \left[M(\epsilon^2 - 1) + \sqrt{\epsilon^2(\epsilon^2 - 1)(M^2 - Q^2)} \right], \quad (6.3.20)$$

which exists only for $\epsilon > M/Q$. We thus have that

$$\frac{\epsilon}{\epsilon_0} > 1 \quad \text{for} \quad r > r_s, \quad (6.3.21)$$

whereas

$$\frac{\epsilon}{\epsilon_0} < 1 \quad \text{for} \quad r_+ < r < r_s. \quad (6.3.22)$$

On the other hand, the condition $\nu = 0$ in Eq. (6.3.13) implies that

$$\left[\Lambda \pm \sqrt{\Lambda^2 - 1 + (\epsilon/\epsilon_0)^2} \right]_{\epsilon/\epsilon_0=1} = 0, \quad (6.3.23)$$

$$\text{i. e.} \quad \left[\Lambda \pm \sqrt{\Lambda^2 - 1} \right]_{r=r_s} = 0, \quad (6.3.24)$$

thus ν_{ϵ}^- is identically zero whereas $\nu_{\epsilon}^+ = 2\Lambda(r_s) = 0$ only for

$$\epsilon = \tilde{\epsilon} \equiv \frac{1}{\sqrt{2}Q} \sqrt{5M^2 - 4Q^2 + \sqrt{25M^2 - 24Q^2}}. \quad (6.3.25)$$

Finally, the lightlike condition $\nu = 1$ is reached only at $r = r_{\gamma}^+$, where $\nu_g = 1 = \nu$.

The behavior of charged test particles depends very strongly on their location with respect to the special radii r_+ , r_l , r_{γ}^+ , and r_s . In Sec. 6.3.1 the behavior of these radii will be analyzed in connection with the problem of stability of circular orbits.

On the other hand, the particle's 4-momentum is given by $P = mU - qA$. Then, the conserved quantities associated with the temporal and azimuthal

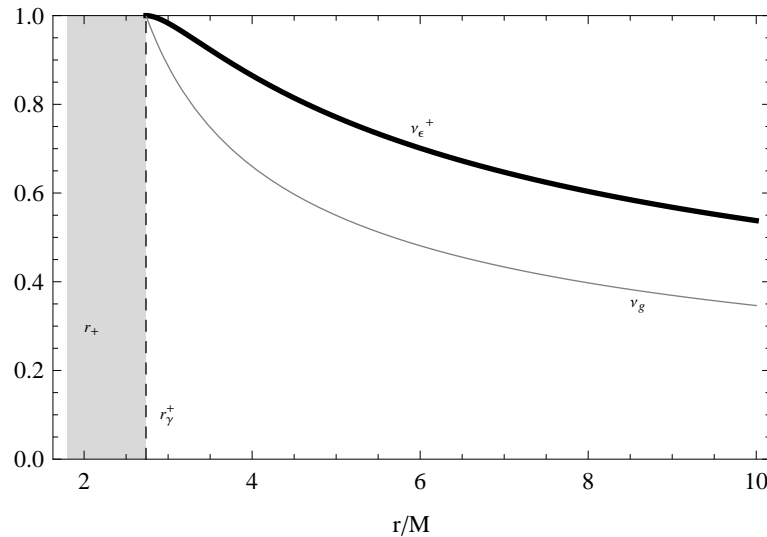


Figure 6.5: The positive solution of the linear velocity v_ϵ^+ is plotted as a function of the radial distance r/M for the parameter choice $Q/M = 0.6$ and $\epsilon = -3$ so that $r_\gamma^+/M \approx 2.74$ and the outer horizon is located at $r_+/M = 1.8$. The geodesic velocity v_g is also shown (gray curve). The shaded region ($r < r_\gamma^+$) is forbidden.

Killing vectors $\zeta = \partial_t$ and $\eta = \partial_\phi$ are respectively

$$P \cdot \zeta = -\frac{\epsilon Q}{r} - \gamma \frac{\sqrt{\Delta}}{r} = -\frac{E}{\mu}, \quad (6.3.26)$$

$$P \cdot \eta = \frac{r}{M} \gamma v = \frac{L}{M\mu}, \quad (6.3.27)$$

where E/μ and L/μ are the particle's energy and angular momentum per unit mass, respectively (see also Eqs.(6.2.2) and (6.2.3)).

Let us summarize the results.

Case $\epsilon < 0$

The solutions are the geodesic velocities $v = \pm v_\epsilon^+$ in the range $r \geq r_\gamma^+$ as illustrated in Fig. 6.5. Orbits with radius $r = r_\gamma^+$ are lightlike. We can also compare the velocity of charged test particles with the geodesic velocity v_g for neutral particles. For $r > r_\gamma^+$ we see that $v_\epsilon^+ > v_g$ always. This means that, at fixed orbital radius, charged test particles acquire a larger orbital velocity compared to that of neutral test particles in the same orbit. As it is possible to see from Eq. (6.3.9) and also in Fig. 6.6, an increase in the particle charge $\epsilon < 0$ corresponds to an increase in the velocity v_ϵ^+ . As the orbital radius decreases, the velocity increases until it reaches the limiting value $v_\epsilon^+ = 1$ which corresponds to the velocity of a photon. This fact can be seen also in Fig. 6.7, where the energy and angular momentum for circular orbits are

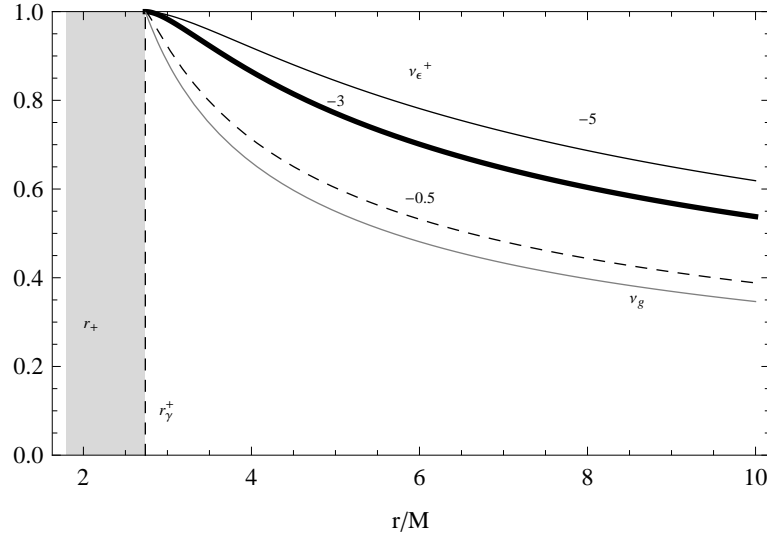


Figure 6.6: The positive solution of the linear velocity v_ϵ^+ is plotted as a function of the radial distance r/M for the parameter choice $Q/M = 0.6$ and different values of $\epsilon = -5$ (black curve), $\epsilon = -3$ (thick black curve), and $\epsilon = -0.5$ (dashed curve). The geodesic velocity v_g for $\epsilon = 0$ is also shown (gray curve). The choice of parameters implies that $r_\gamma^+/M \approx 2.74$ and the outer horizon is located at $r_+/M = 1.8$. The shaded region is forbidden. For $r > r_\gamma^+$ it holds that $v_\epsilon^+ > v_g$.

plotted in terms of the distance r . Clearly, this graphic shows that to reach the photon orbit at $r = r_\gamma^+$, the particles must acquire an infinity amount of energy and angular momentum. In Fig. 6.8 we analyze the behavior of the particle's energy and angular momentum in terms of the specific charge ϵ . It follows that both quantities decrease as the value of $|\epsilon|$ decreases.

Case $\epsilon = 0$

The solutions are the geodesic velocities $v = \pm v_g$ in the range $r \geq r_\gamma^+$. This case has been studied in detail in [31].

Case $\epsilon > 0$

Depending on the explicit values of the parameters Q and ϵ and the radial coordinate r , it is necessary to analyze several subcases.

a) $\epsilon < M/Q$ and $r \geq r_l$.

There are two different branches for both signs of the linear velocity: $v = \pm v_\epsilon^+$ in the range $r_l \leq r \leq r_\gamma^+$, and $v = \pm v_\epsilon^-$ in the whole range $r \geq r_l$. The two branches join at $r = r_l$, where $v_\epsilon^+ = v_\epsilon^- = v_g \sqrt{\Lambda}$, as shown in Fig. 6.9. First we note that in this case for $r > r_\gamma^+$ it always holds that $v_\epsilon^- < v_g$. This means that, at fixed orbital radius, charged

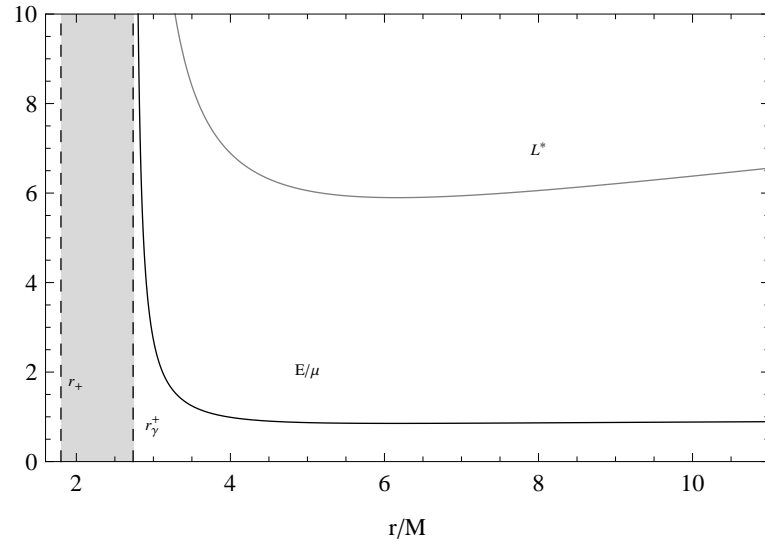


Figure 6.7: The energy E/μ and angular momentum $L^* \equiv L/(\mu M)$ of a charged particle of charge-to-mass ratio ϵ moving in the field of a RN black hole with charge Q and mass M are plotted as functions of the radial distance r/M for the parameter choice $Q/M = 0.6$ and $\epsilon = -3$, with $r_\gamma^+/M \approx 2.74$ and the outer horizon located at $r_+/M = 1.8$. The shaded region is forbidden.

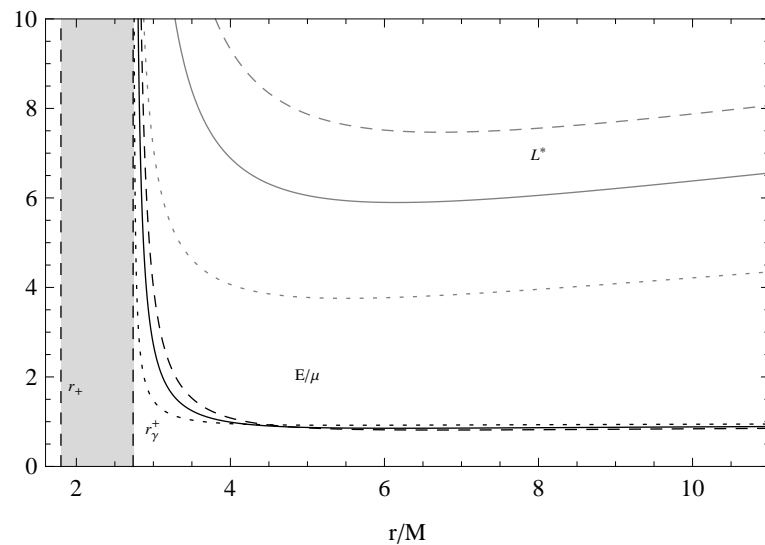


Figure 6.8: The energy E/μ and angular momentum $L^* \equiv L/(\mu M)$ of a charged particle of charge-to-mass ratio ϵ moving in the field of a RN black hole with charge Q and mass M are plotted as functions of the radial distance r/M for the parameter choice $Q/M = 0.6$ and $\epsilon = -3$ (solid curves), $\epsilon = -5$ (dashed curves), $\epsilon = -0.5$ (dotted curves). Here $r_\gamma^+/M \approx 2.74$ and the outer horizon is located at $r_+/M = 1.8$. The shaded region is forbidden. The energy and angular momentum decrease as $|\epsilon|$ decreases.

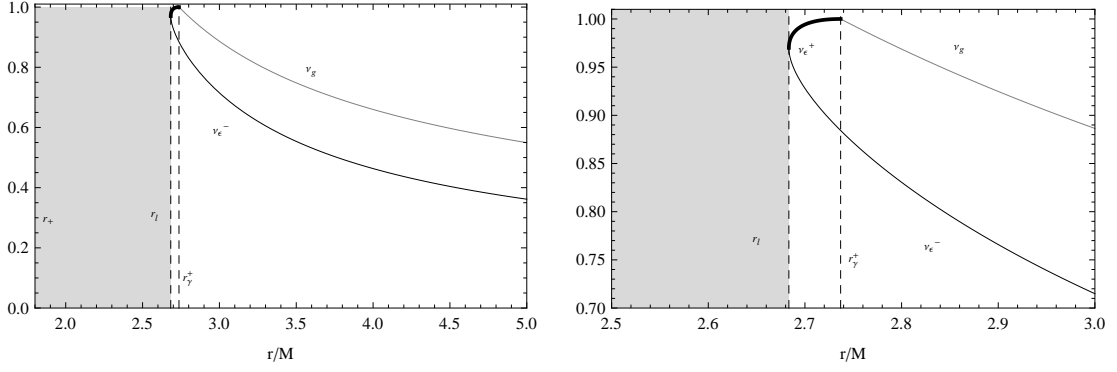


Figure 6.9: The positive solution of the linear velocity v_ϵ^\pm is plotted as a function of the radial distance r/M in the region $[1.8, 5]$ (left graphic) and $[2.5, 3]$ (right graphic). Here $Q/M = 0.6$ and $\epsilon = 1.2$, so that $r_l/M = 2.68$ and $r_\gamma^+ = 2.737M$. For the chosen parameters we have that $\tilde{\epsilon} = 3.25$ and $\epsilon_l = 4.12$. The region within the interval $[r_l, r_\gamma^+]$ is forbidden for neutral particles.

test particles possess a smaller orbital velocity than that of neutral test particles in the same orbit. This is in accordance to the fact that in this case, a black hole with $\epsilon Q > 0$, the attractive gravitational force is balanced by the repulsive electromagnetic force. In the region $r > r_\gamma^+$, the orbital velocity increases as the radius approaches the value r_γ^+ (see Fig. 6.9). The interval $r_l \leq r \leq r_\gamma^+$ presents a much more complex dynamical structure. First we note that, due to the Coulomb repulsive force, charged particle orbits are allowed in a region which is forbidden for neutral test particles. This is an interesting result leading to the possibility of accretion disks in which the innermost part forms a ring of charged particles only. Indeed, suppose that an accretion disk around a RN black hole is made of neutral and charged test particles. Then, the accretion disk can exist only in the region $r \geq r_l$ with a ring of charged particles in the interval $[r_l, r_\gamma^+]$. Outside the exterior radius of the ring ($r > r_\gamma^+$), the disk can be composed of neutral and charged particles. This situation can also be read from Fig. 6.10 where the energy and the angular momentum are plotted as functions of the radial distance r/M .

b) $M/Q < \epsilon < \tilde{\epsilon}$ and $r_l \leq r \leq r_s$.

Since $r < r_s$, one has that $\epsilon/\epsilon_0 < 1$, implying that both solutions v_ϵ^+ and v_ϵ^- can exist. There are two different branches for both signs: $v = \pm v_\epsilon^+$ in the range $r_l \leq r \leq r_\gamma^+$, and v_ϵ^- in the entire range $r_l \leq r \leq r_s$. The two branches join at $r = r_l$. Note that for increasing values of ϵ , the radius r_s decreases and approaches r_l , reaching it at $\epsilon = \tilde{\epsilon}$, and as ϵ tends to infinity r_s tends to the outer horizon r_+ (see Fig. 6.11). In particular, the interaction between the attractive gravitational force and the

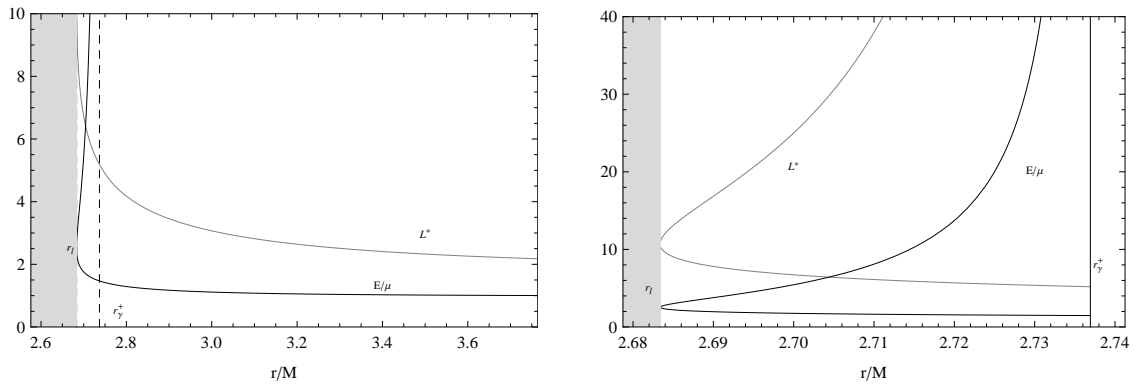


Figure 6.10: The energy E/μ and angular momentum $L^* \equiv L/(\mu M)$ of a charged particle of charge-to-mass ratio ϵ moving along circular orbits in a Reissner–Nordström black hole of charge Q and mass M are plotted in terms of the radial distance r/M in the range $[2.6, 3.8]$ (left graphic) $[2.68, 2.74]$ (right graphic). Here $Q/M = 0.6$ and $\epsilon = 1.2$, so that $r_l/M = 2.68$ and $r_\gamma^+/M = 2.737$. For the chosen parameters we have that $\tilde{\epsilon} = 3.25 \epsilon_l = 4.12$. The shaded region is forbidden for any particles.

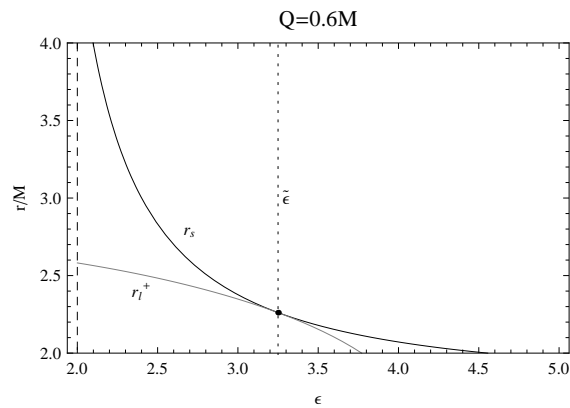


Figure 6.11: Radius $r_s = r_s^+$ (black curve) and $r_l = r_l^+$ (gray curve), are plotted as function of ϵ for $Q = 0.6M$. $r_s^+ = r_l^+$ for $\epsilon = \tilde{\epsilon} \approx 3.25$.

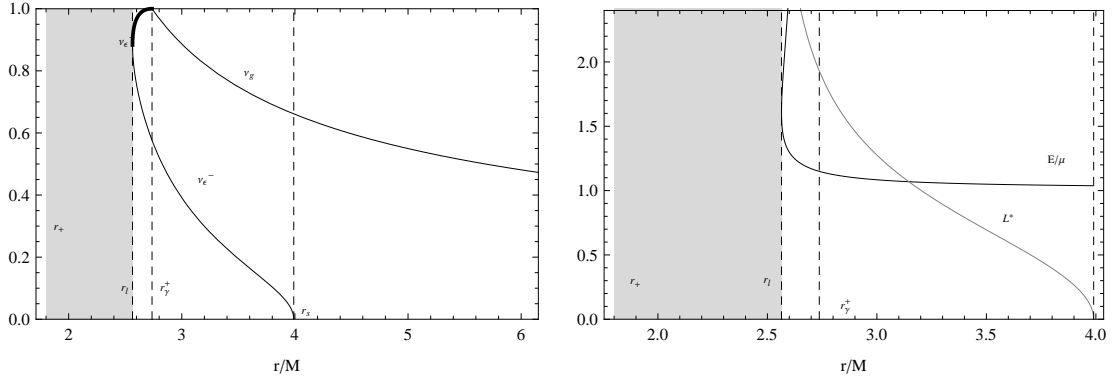


Figure 6.12: Left graphic: The positive solution of the linear velocity v is plotted as a function of the radial distance r/M . Right graphic: The energy E/μ and angular momentum $L^* \equiv L/(\mu M)$ of a charged particle of charge-to-mass ratio ϵ are plotted in terms of r/M . The parameter choice is $Q/M = 0.6$ and $\epsilon = 2.1$. Then, $r_l/M = 2.56$, $r_{\gamma}^+/M = 2.737$, and $r_s/M = 3.99$. Moreover, for this choice $\tilde{\epsilon} = 3.25$ and $\epsilon_l = 4.12$. The shaded region is forbidden.

Coulomb force generates a zone $r_l \leq r \leq r_{\gamma}^+$ in which only charged test particles can move along circular trajectories while neutral particles are allowed in the region $r > r_{\gamma}^+$ (see Fig. 6.12). This result again could be used to construct around black holes accretion disks with rings made of charged particles.

c) $\tilde{\epsilon} < \epsilon < \epsilon_l$ and $r_s < r < r_{\gamma}^+$.

The solution v_{ϵ}^- for the linear velocity is not allowed whereas the solution v_{ϵ}^+ is valid in the entire range. In fact, the condition $r > r_s$ implies that $\epsilon/\epsilon_0 > 1$, and therefore $\Lambda^2 - 1 + (\epsilon/\epsilon_0)^2 > \Lambda^2$, so that the condition (6.3.17) for the existence of velocities is satisfied for the plus sign only. Therefore, the solutions are given by $v = \pm v_{\epsilon}^+$ in the entire range as shown in Fig. 6.13. At the radius orbit $r = r_s$, the angular momentum and the velocity of the test particle vanish, indicating that the particle remains at rest with respect to static observers located at infinity. In the region $r_s < r < r_{\gamma}^+$ only charged particles can move along circular trajectories.

d) $\epsilon > \epsilon_l$ and $r_s < r < r_{\gamma}^+$.

In this case the radius r_l does not exist. The solutions are the velocities $v = \pm v_{\epsilon}^+$ in the entire range. Note that for $\epsilon \rightarrow \infty$ one has that $r_s \rightarrow r_+$. Also in this case we note that neutral particles can stay in circular orbits with a velocity v_g only in the region $r > r_{\gamma}^+$ whereas charged test particles are allowed within the interval $r_s < r < r_{\gamma}^+$, as shown in Fig.

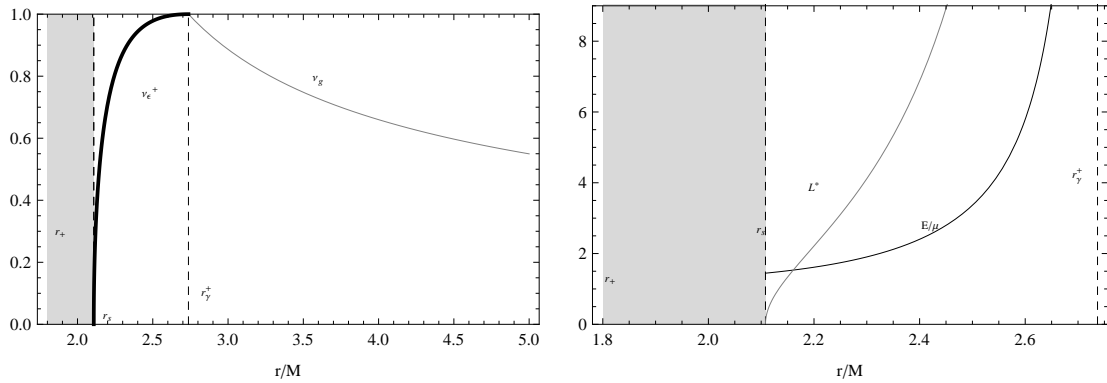


Figure 6.13: Left graphic: The positive solution of the linear velocity v is plotted as a function of the radial distance r/M . Right graphic: The energy E/μ and angular momentum $L^* \equiv L/(\mu M)$ of a charged particle of charge-to-mass ratio $\epsilon = 3.8$ moving in a RN space-time with $Q/M = 0.6$ are plotted in terms of the radial distance r/M . For this choice of parameters the radii are $r_l/M = 1.98$, $r_s/M = 2.11$, and $r_\gamma^+/M = 2.737$ whereas the charge parameters are $\tilde{\epsilon} = 3.25$ and $\epsilon_l = 4.12$.

6.14. Clearly, for charged and neutral test particles the circular orbit at $r = r_\gamma^+$ corresponds to a limiting orbit.

6.3.1 Stability

To analyze the stability of circular orbits for charged test particles in a RN black hole we must consider the condition (6.2.7) which leads to the Eqs.(6.2.8), (6.2.8), and (6.2.9). So the stability of circular orbits strongly depends on the sign of (ϵQ) . The case $\epsilon Q \leq 0$ is illustrated in Fig. 6.15 where the radius of the last stable circular orbit r_{lsc0} is plotted for two different values of ϵ as a function of Q/M . It can be seen that the energy and angular momentum of the particles decrease as the value of Q/M increases. These graphics also include the radius of the outer horizon r_+ and the radius r_γ^+ which determines the last (unstable) circular orbit of neutral particles. In Sec. 6.3, we found that circular orbits for charged particles are allowed also inside the radius r_γ^+ for certain values of the parameters; however, since $r_\gamma^+ < r_{\text{lsc0}}$, we conclude that all those orbits must be unstable. From Fig. 6.16 we see that for $Q = 0$ and $\epsilon = 0$, the well-known result for the Schwarzschild case, $r_{\text{lsc0}} = 6M$, is recovered. Also in the limiting case $Q = M$ and $\epsilon = 0$, we recover the value of $r_{\text{lsc0}} = 4M$ for neutral particles moving along circular orbits in an extreme BN black hole. In general, as the value of $|\epsilon|$ increases we see that the value of r_{lsc0} increases as well. This behavior resembles the case of the radius of the last stable orbit for neutral test particles [31, 32]. Indeed, in the case $\epsilon Q < 0$ the attractive Coulomb force reinforces the attractive gravitational force so that the general structure remains unchanged. We also can expect that an increase in the charge of the particle $|\epsilon|$ produces an increase in the velocity of the sta-

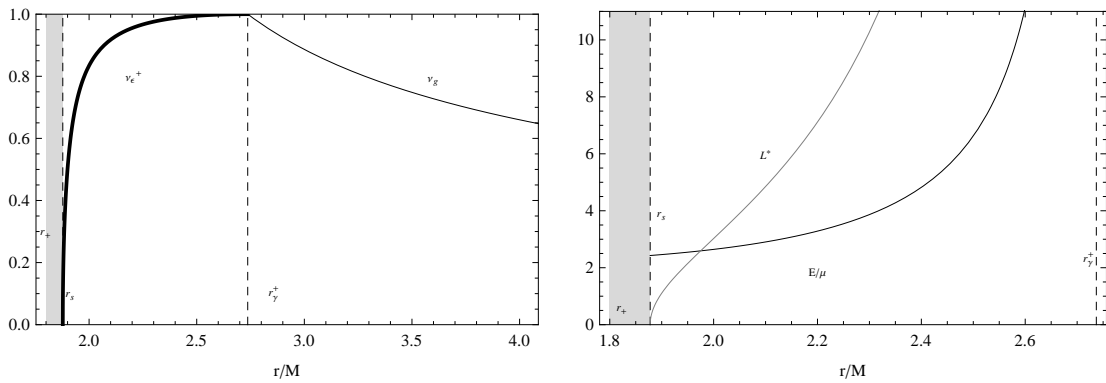


Figure 6.14: Left graphic: The positive solution of the linear velocity v is plotted as a function of the radial distance r/M . Right graphic: The energy E/μ and angular momentum $L^* \equiv L/(\mu M)$ of a charged particle of charge-to-mass ratio $\epsilon = 7$, moving in the field of a RN black hole with $Q/M = 0.6$, are plotted in terms of the radial distance r/M . For this parameter choice $r_s/M = 1.88$, $\tilde{\epsilon} = 3.25$, and $\epsilon_l = 4.12$.

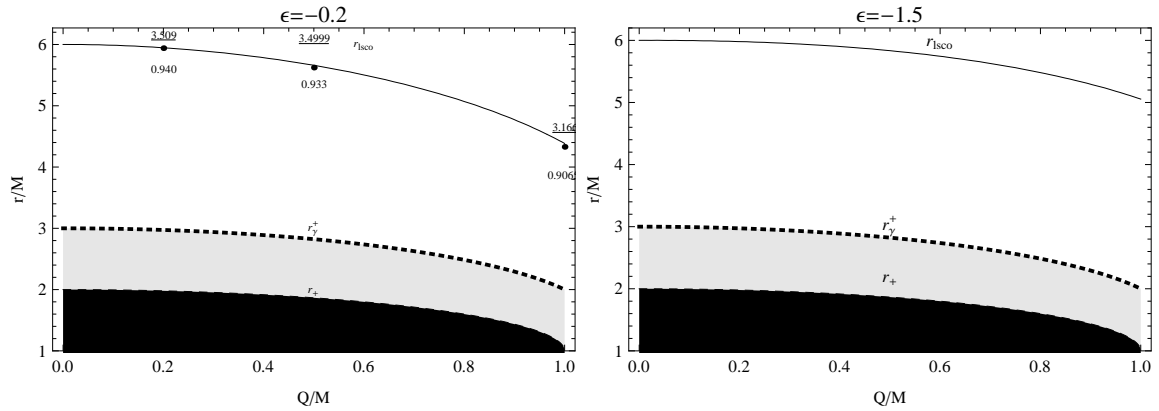


Figure 6.15: The radius of the last stable circular orbit r_{lSCO} in a RN black hole of mass M and charge Q for a particle with ratio $\epsilon = -0.2$ (left plot) and $\epsilon = -1.5$ (right plot). Numbers close to the point represent the energy E/μ of the last stable circular orbits at that point. Underlined numbers represent the corresponding angular momentum $L/(M\mu)$. Stable orbits are possible only for $r > r_{\text{lSCO}}$. For comparison we also include the curves for the radii r_+ and r_γ^+ .

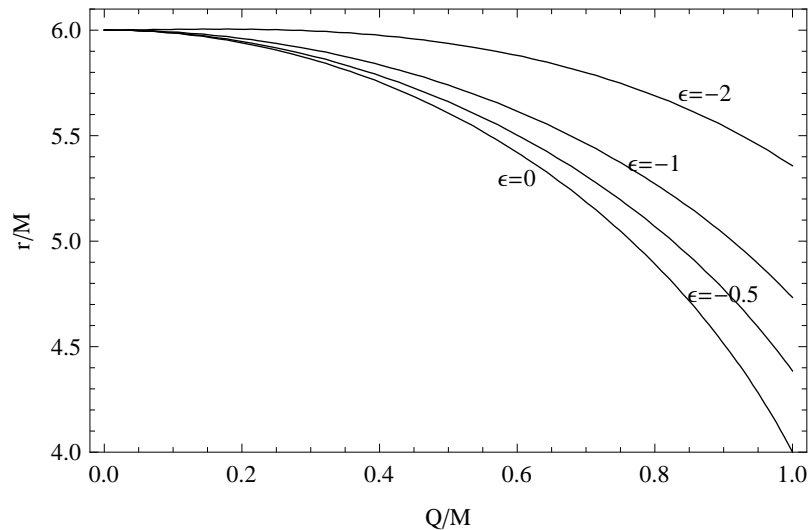


Figure 6.16: The radius r_{lsc0} of the last stable circular orbit in a RN black with charge-to-mass ratio Q/M for selected values of the charge-to-mass ratio ϵ of the test particle. Only the case $\epsilon Q \leq 0$ is illustrated. Stable orbits are possible only for $r > r_{\text{lsc0}}$

ble circular orbits. In fact, this can be seen explicitly from Eq. (6.3.9) and Fig. 6.6. It then follows that the energy and angular momentum of the charged test particle increases as the value of $|\epsilon|$ increases.

The case of $\epsilon Q > 0$ is illustrated in Figs. 6.17 and 6.18. The situation is very different from the case of neutral particles or charged particles with $\epsilon Q < 0$. Indeed, in this case the Coulomb force is repulsive and leads to a non trivial interaction with the attractive gravitational force, see also [50, 51, 52, 53, 54, 55, 56, 57, 58, 59]. It is necessary to analyze two different subcases. The first subcase for $\epsilon > 1$ is illustrated in Fig. 6.17 while the second one for $0 < \epsilon < 1$ is depicted in Fig. 6.18. We can see that in the case $0 < \epsilon < 1$ the stability regions are similar to those found in the case $\epsilon < 0$ (cf. Figs. 6.15 and 6.18). This means that for weakly-charged test particles, $0 < \epsilon < 1$, it always exists a stable circular orbit and $r_{\text{lsc0}} \geq 4M$, where the equality holds for an extreme black hole. On the contrary, in the case $\epsilon > 1$ there are regions of Q and ϵ in which stable circular orbits cannot exist at all. As can be seen from Fig. 6.17, charged particles moving along circular orbits with radii located within the region $r < r_{\gamma}^+$ or $r < r_s$ must be unstable.

We conclude that the ring structure of the hypothetical accretion disks around a RN black hole mentioned in Sec. 6.3 must be unstable.

6.4 Naked singularities

The effective potential V_{\pm} given in Eq. (9) in the case of naked singularities ($M^2 < Q^2$) is plotted in Figs. (6.19–6.22) in terms of the radial coordinate

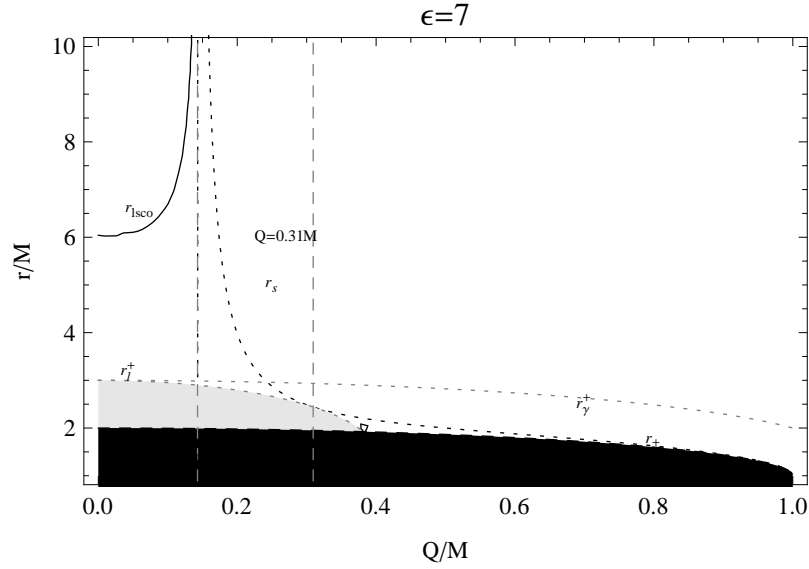


Figure 6.17: The radius of the last stable circular orbit r_{lSCO} (solid curve) for a charged test particle with $\epsilon = 7$, in a RN black hole with charge Q and mass M , is plotted as a function of the ratio Q/M . Other curves are the outer horizon radius $r_+ = M + \sqrt{M^2 - Q^2}$ and the radii $r_\gamma^+ \equiv [3M + \sqrt{(9M^2 - 8Q^2)}]/2$, $r_s \equiv \frac{Q^2}{\epsilon^2 Q^2 - M^2} [\epsilon \sqrt{M^2 - Q^2} \sqrt{\epsilon^2 - 1} + M(\epsilon^2 - 1)]$, $r_l \equiv \frac{3M}{2} + \frac{1}{2} \sqrt{9M^2 - 8Q^2 - Q^2 \epsilon^2}$. Shaded and dark regions are forbidden for timelike particles. Stable orbits are possible only for $r > r_{\text{lSCO}}$.

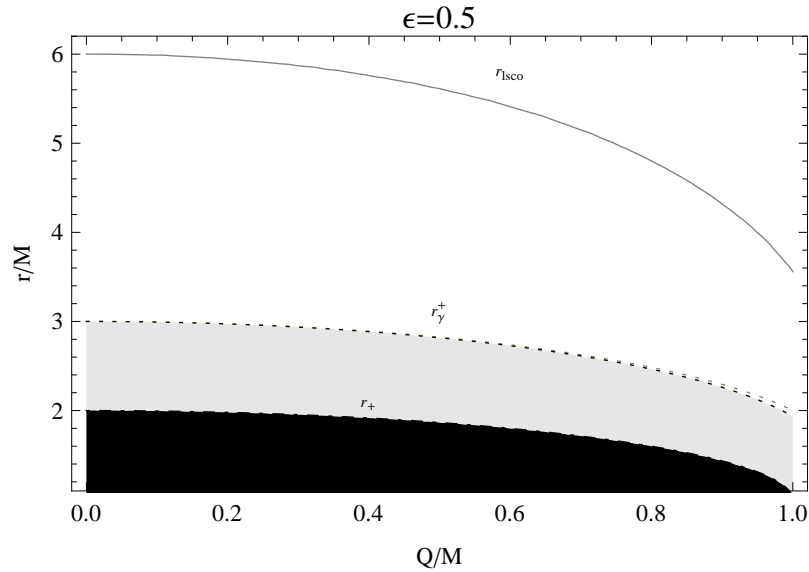


Figure 6.18: The radius of the last stable circular orbit r_{lSCO} (solid curve) for a charged test particle with $\epsilon = 0.5$, in a RN black hole with charge Q and mass M , is plotted as a function of the ratio Q/M . Other curves are the outer horizon radius r_+ and the radius r_γ^+ . Shaded and dark regions are forbidden for timelike particles. Stable orbits are possible only for $r > r_{\text{lSCO}}$.

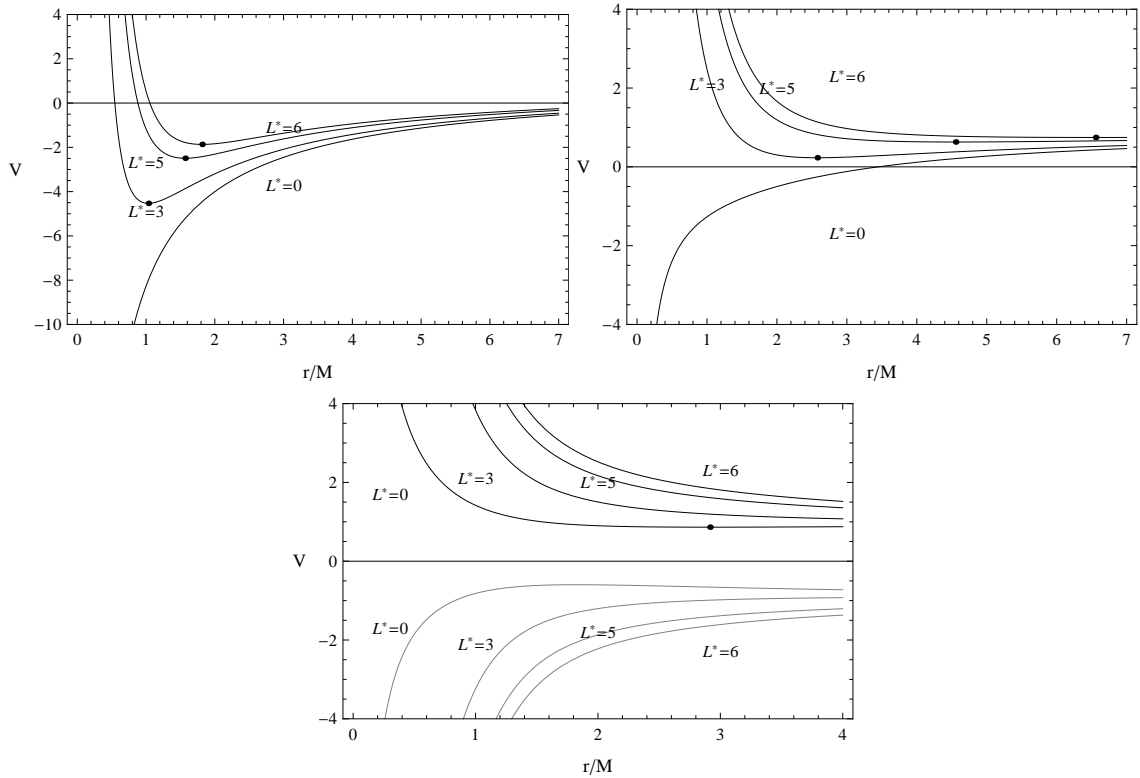


Figure 6.19: The effective potential for a charged particle with charge-to-mass ratio ϵ in a RN naked singularity of charge Q and mass M is plotted as a function of the radius r/M for fixed values of the angular momentum $L^* \equiv L/(\mu M)$. Black curves represent the positive solution V_+ while gray curves correspond to V_- . The boldfaced points denote the minima of the potentials. In upper left plot, the parameter choice is $Q/M = 2$ and $\epsilon = -1.5$; the upper right plot is for $Q/M = 2$ and $\epsilon = -5$ while the bottom plot corresponds to the choice $Q/M = 1.5$ and $\epsilon = -0.2$.

r/M for selected values of the ratio ϵ and the angular momentum $L/(M\mu)$ of the test particle, see also [60, 61, 62, 63, 64, 65, 43, 49]. The effective potential profile strongly depends on the sign of ϵQ . Moreover, the cases with $|\epsilon| \leq 1$ and with $|\epsilon| > 1$ must be explored separately.

Fig. 6.20 shows the effective potential for a particle of charge-to-mass ϵ in the range $[-10, -1]$. The presence of minima (stable circular orbits) in the effective potential with negative energy states is evident. Moreover, we note that the minimum of each potential decreases as $|\epsilon|$ increases. This fact is due to the attractive and repulsive effects of the gravitational and electric forces [50, 51, 52, 53, 54, 55, 56, 57, 58, 59]. In Fig. 6.21 the effective potential is plotted for negative and positive values of the charge-to-mass ratio ϵ . We see that for a fixed value of the radial coordinate and the angular momentum of the particle, the value of the potential V increases as the value of ϵ increases. In the Fig. 6.22 we plot the effective potential for a fixed Q/M as function of the radial coordinate and the angular momentum for two different cases,

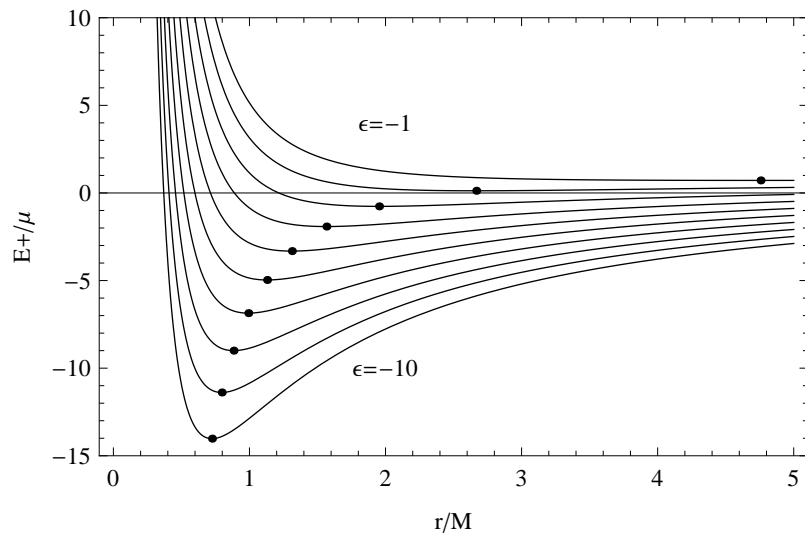


Figure 6.20: The effective potential of a RN naked singularity with $Q/M = 2$ for a particle with charge-to-mass ratio ϵ in the range $[-10, -1]$ and angular momentum $L/(M\mu) = 4$.

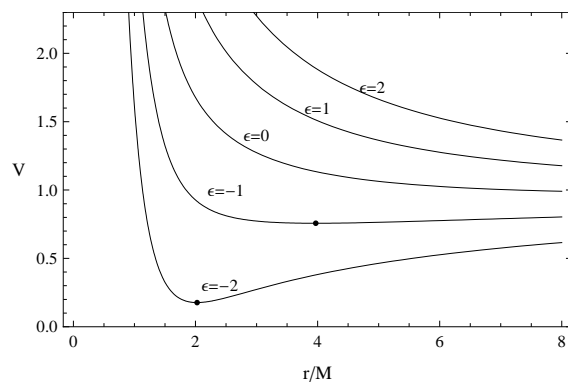


Figure 6.21: The effective potential of a RN naked singularity with $Q/M = 3/2$ for a particle with charge-to-mass ratio ϵ in the range $[-2, +2]$ and angular momentum $L/(M\mu) = 4$.

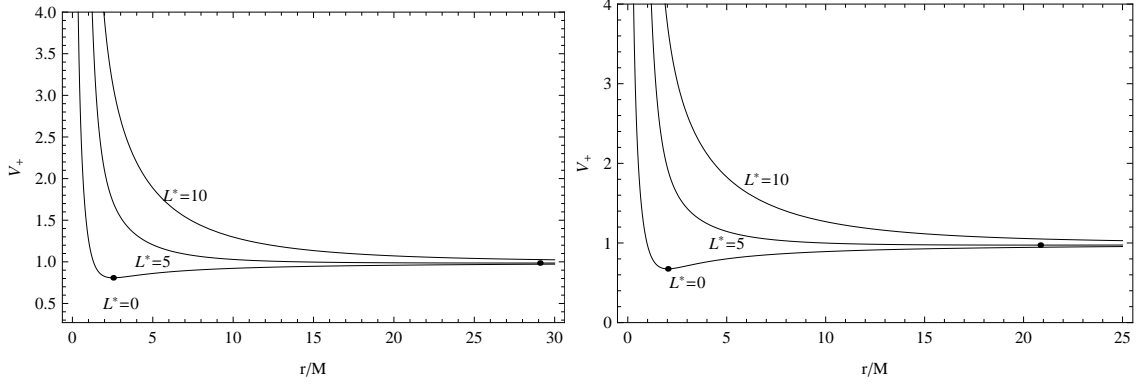


Figure 6.22: The effective potential V_+ of a RN naked singularity with $Q/M = 3/2$ for a charged particle is plotted for different values of the angular momentum $L^* \equiv L/(M\mu)$. The left plot corresponds to the ratio $\epsilon = 0.1$ while the right one is for $\epsilon = -0.1$. For $\epsilon = 0.1$ there is a minimum, $V_{min} \approx 0.81$, at $r_{min} \approx 2.52M$ for $L^* = 0$, and a minimum, $V_{min} \approx 0.96$, at $r_{min} \approx 29M$ for $L^* = 5$. For $\epsilon = -0.1$ the minimum, $V_{min} \approx 0.67$, is located at $r_{min} \approx 2.02M$ for $L^* = 0$, and at $r_{min} \approx 20.8M$ with $V_{min} \approx 0.97$ for $L^* = 5$.

$\epsilon = 0.1$ and $\epsilon = -0.1$. We can see that in the first case the presence of a repulsive Coulomb force reduces the value of the radius of the last stable circular orbit for a fixed angular momentum. We note the existence of stable “circular” orbits with $L = 0$ at which the particle is at rest with respect to static observers located at infinity.

Negative energy states are possible only in the case $\epsilon Q < 0$. The region in which the solution V_+ has negative energy states is

$$0 < r < M + \sqrt{M^2 - Q^2(1 - \epsilon^2)} \quad \text{for } \epsilon \leq -1, \quad (6.4.1)$$

and

$$0 < r < r_l^+ \quad \text{for } 0 \leq L < L_q, \quad \epsilon \leq -1, \quad (6.4.2)$$

$$r_l^- < r < r_l^+ \quad \text{for } 0 \leq L < L_q, \quad -1 < \epsilon \leq -\sqrt{1 - \frac{M^2}{Q^2}}, \quad (6.4.3)$$

where

$$\frac{L_q}{\mu} \equiv r \sqrt{\frac{\epsilon^2 Q^2}{r^2 - 2Mr + Q^2} - 1}. \quad (6.4.4)$$

In general, for a particle in circular motion with radius r_0 and charge-to-mass ratio ϵ , around a RN naked singularity with charge Q and mass M , the corresponding angular momentum must be chosen as

$$\frac{L^2}{\mu^2} < r_0^2 \left(\frac{\epsilon^2 Q^2}{r_0^2 - 2Mr_0 + Q^2} - 1 \right), \quad (6.4.5)$$

in order for negative energy states to exist.

The conditions for circular motion around a RN naked singularity are determined by Eq. (6.2.1) which can be used to find the energy and angular momentum of the test particle. Indeed, Eqs. (6.2.2) and (6.2.3) define the angular momentum L^\pm and the energy E^\pm , respectively, in terms of r/M , Q/M , and ϵ . The explicit dependence of these parameters makes it necessary to investigate several intervals of values. To this end, it is useful to introduce the following notation

$$r_l^\pm \equiv \frac{3M}{2} \pm \frac{1}{2} \sqrt{9M^2 - 8Q^2 - Q^2\epsilon^2}, \quad (6.4.6)$$

$$\tilde{\epsilon}_\pm \equiv \frac{1}{\sqrt{2}Q} \sqrt{5M^2 \pm 4Q^2 + \sqrt{25M^2 - 24Q^2}}, \quad (6.4.7)$$

and

$$\tilde{\tilde{\epsilon}}_\pm \equiv \frac{1}{\sqrt{2}Q} \sqrt{3M^2 - 2Q^2 \pm M\sqrt{9M^2 - 8Q^2}}. \quad (6.4.8)$$

We note that

$$\lim_{\epsilon \rightarrow 0} r_s^\pm = r_* = \frac{Q^2}{M}, \quad (6.4.9)$$

which corresponds to the classical radius of a mass M with charge Q , see for example [66, 67], and

$$\lim_{\epsilon \rightarrow 0} r_l^\pm = r_\gamma^\pm = \frac{3M}{2} \pm \frac{1}{2} \sqrt{9M^2 - 8Q^2}, \quad (6.4.10)$$

which represents the limiting radius at which neutral particles can be in circular motion around a RN naked singularity [31].

The behavior of the charge parameters defined above is depicted in Fig. 6.23 in terms of the ratio $Q/M > 1$. It follows from Fig. 6.23 that it is necessary to consider the following intervals:

$$Q/M \in (1, 5/(2\sqrt{6})], \quad (6.4.11)$$

$$Q/M \in (5/(2\sqrt{6}), (3\sqrt{6})/7], \quad (6.4.12)$$

$$Q/M \in ((3\sqrt{6})/7, \sqrt{9/8}], \quad (6.4.13)$$

$$Q/M \in [\sqrt{9/8}, \infty). \quad (6.4.14)$$

Our approach consists in analyzing the conditions for the existence of circular orbits by using the expressions for the angular momentum, Eq. (6.2.2), and the energy, Eq. (6.2.3), of the particle together with the expressions for the velocity obtained in Sec. 6.3. We consider separately the case $\epsilon > 0$ in Secs. 6.4.1 and 6.4.2, and $\epsilon < 0$ in Secs. 6.4.3 and 6.4.4.

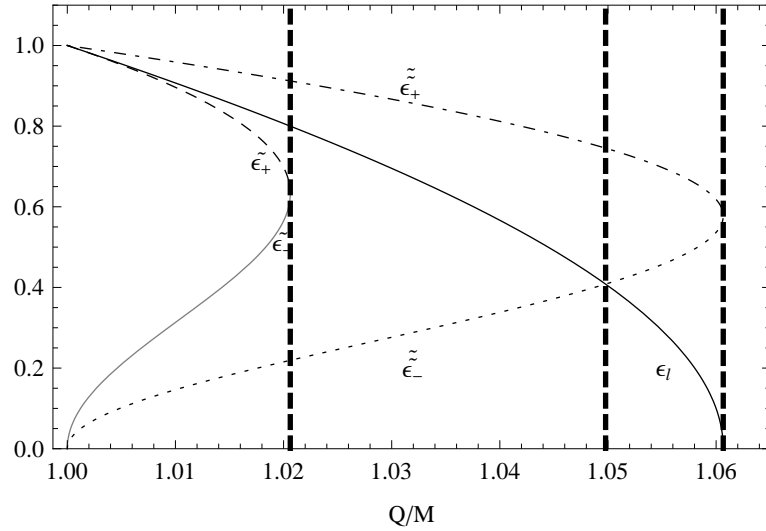


Figure 6.23: The charge parameters ϵ_l (black solid curve), $\tilde{\epsilon}_-$ (gray solid curve), $\tilde{\epsilon}_+$ (dashed curve), $\tilde{\tilde{\epsilon}}_-$ (dotted curve), and $\tilde{\tilde{\epsilon}}_+$ (dotdashed curve) as functions of the charge-to-mass ratio of the RN naked singularity. The special lines $Q/M = 5/(2\sqrt{6}) \approx 1.02$, $Q/M = 3\sqrt{6}/7 \approx 1.05$, and $Q/M = \sqrt{9/8} \approx 1.06$ are also plotted.

6.4.1 Case $\epsilon > 1$

For $\epsilon > 0$ the condition (6.3.12) implies in general that $r > r_* \equiv Q^2/M$. Imposing this constraint on Eqs.(6.2.2) and (6.2.3), we obtain the following results for timelike orbits. For $\epsilon > 1$ and $M < Q < \sqrt{9/8}M$ circular orbits exist with angular momentum $L = L^+$ in the interval $r_\gamma^- < r < r_\gamma^+$, while for $Q \geq \sqrt{9/8}M$ no circular orbits exist (see Fig. 6.24). Clearly, the energy and angular momentum of circular orbits diverge as r approaches the limiting orbits at r_γ^\pm . This means that charged test particles located in the region $r_\gamma^- < r < r_\gamma^+$ need to acquire an infinite amount of energy to reach the orbits at r_γ^\pm . The energy of the states is always positive. A hypothetical accretion disk would consist in this case of a charged ring of inner radius r_γ^- and outer radius r_γ^+ , surrounded by a disk of neutral particles. The boundary $r = r_\gamma^+$ in this case would be a lightlike hypersurface.

Since for $\epsilon Q > 0$ the Coulomb interaction is repulsive, the situation characterized by the values for $Q \geq \sqrt{9/8}M$ and $\epsilon > 1$ corresponds to a repulsive electromagnetic effect that cannot be balanced by the attractive gravitational interaction. We note that the case $Q \geq \sqrt{9/8}M$ and $\epsilon > 1$ could be associated to the realistic configuration of a positive ion or a positron in the background of a RN naked singularity.

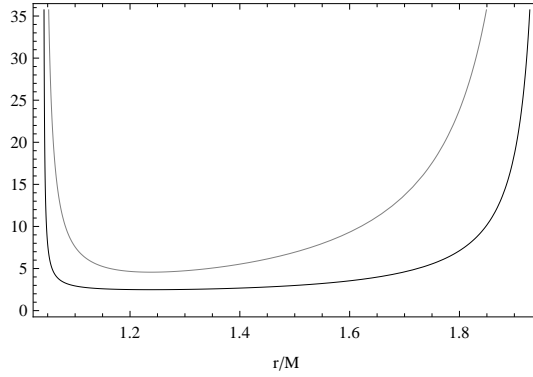


Figure 6.24: The case $\epsilon > 1$. The energy (black curve) and angular momentum (gray curve) for a test particle with charge-to-mass ratio $\epsilon = 2$ in a RN naked singularity with $Q = 1.06M$. Circular orbits exist in the interval $r_\gamma^- < r < r_\gamma^+$, where $r_\gamma^- = 1.04196M$ and $r_\gamma^+ = 1.95804M$.

6.4.2 Case $0 < \epsilon < 1$

It turns out that in this case it is necessary to consider separately each of the four different regions for the ratio Q/M that follow from Fig. 6.23. Moreover, in each region of Q/M it is also necessary to consider the value of ϵ for each of the zones determined by the charge parameters ϵ_l , $\tilde{\epsilon}_\pm$, and $\tilde{\tilde{\epsilon}}_\pm$, as shown in Fig. 6.23. We analyzed all the resulting cases in detail and found the values of the energy and angular momentum of charged test particles in all the intervals where circular motion is allowed. We summarize the results as follows.

There is always a minimum radius r_{min} at which circular motion is allowed. We found that either $r_{min} = r_s^+$ or $r_{min} = r_\gamma^-$. Usually, at the radius r_s^+ the test particle acquires a zero angular momentum so that a static observer at infinity would consider the particle as being at rest. Furthermore, at the radius r_γ^- the energy of the test particle diverges, indicating that the hypersurface $r = r_\gamma^-$ is lightlike. In the simplest case, circular orbits are allowed in the infinite interval $[r_{min}, \infty)$ so that, at any given radius greater than r_{min} , it is always possible to have a charged test particle moving on a circular trajectory. Sometimes, inside the infinite interval $[r_{min}, \infty)$, there exists a lightlike hypersurface situated at $r_\gamma^+ > r_{min}$.

Another possible structure is that of a finite region filled with charged particles within the spatial interval $(r_{min} = r_\gamma^-, r_{max} = r_\gamma^+)$. This region is usually surrounded by an empty finite region in which no motion is allowed. Outside the empty region, we find a zone of allowed circular motion in which either only neutral particles or neutral and charged particles can exist in circular motion. Clearly, this spatial configuration formed by two separated regions in which circular motion is allowed, could be used to build with test particles an accretion disk of disconnected rings. A particular example of this case is

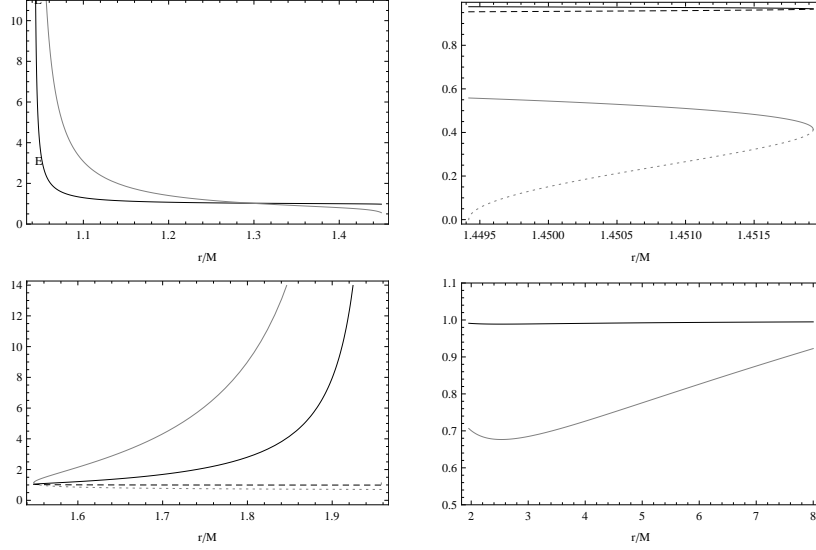


Figure 6.25: Case: $M < Q \leq 5/(2\sqrt{6})M$ and $\tilde{\epsilon}_+ < \epsilon \leq \epsilon_l$. Parameter choice: $Q = 1.01M$ and $\epsilon = 0.902$. Then $\epsilon_l = 0.907$, $\tilde{\epsilon}_+ = 0.8963$, $r_s^+ = 1.44942M$, $r_\gamma^- = 1.04196M$, $r_\gamma^+ = 1.95804M$, $r_l^- = 1.45192M$, and $r_l^+ = 1.548077M$. Circular orbits exist with angular momentum $L = L^+$ (gray curves) and energy $E = E^+$ (black curves) in $r_\gamma^- < r < r_s^+$ (upper left plot); $L = L^\pm$ in $r_s^+ \leq r < r_l^-$ (upper right plot) and $r_l^+ \leq r < r_\gamma^+$ (bottom left plot); $L = L^-$ in $r \geq r_\gamma^+$ (bottom right plot).

illustrated in Fig. 6.25

6.4.3 Case $\epsilon < -1$

The contribution of the electromagnetic interaction in this case is always attractive. Hence, the only repulsive force to balance the attractive effects of the gravitational and Coulomb interactions can be generated only by the RN naked singularity. This case therefore can be compared with the neutral test particle motion as studied in [31, 32]. Then, it is convenient, as in the case of a neutral test particle, to consider the two regions $Q > \sqrt{9/8}M$ and $M < Q \leq \sqrt{9/8}M$ separately.

For $\epsilon < -1$ and for $Q > \sqrt{9/8}M$ circular orbits with $L = L^+$ always exist for $r > 0$ (in fact, however, one has to consider also the limit $r > r_*$ for the existence of timelike trajectories). This case is illustrated in Fig. 6.26 where the presence of orbits with negative energy states is evident.

For $M < Q \leq \sqrt{9/8}M$ circular orbits exist with $L = L^+$ in $0 < r < r_\gamma^-$ and $r > r_\gamma^+$ (see Fig. 6.27). We note that for neutral test particles in the region $M < Q \leq \sqrt{9/8}M$, (stable) circular orbits are possible for $r > r_* = Q^2/M$. At $r = r_*$, the angular momentum of the particle vanishes [31]. On the contrary, charged test particles with $\epsilon < -1$ can move along circular orbits also in the region $(0, r_*]$. The value of the energy on circular orbits increases as r

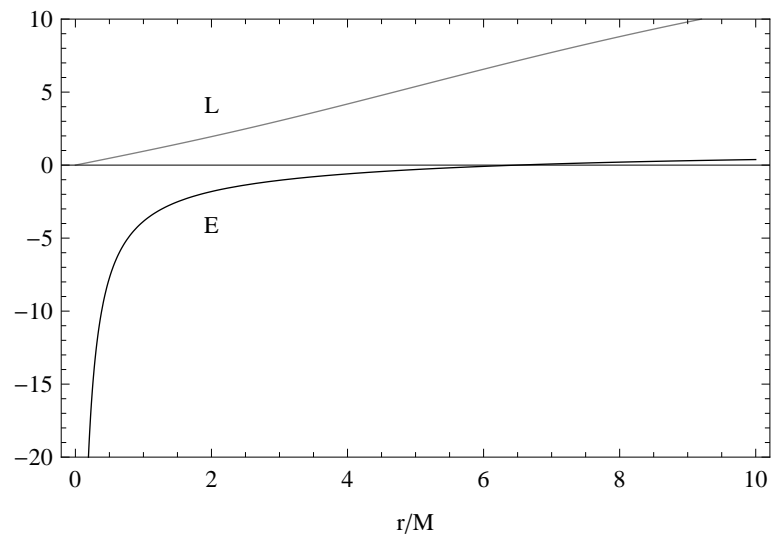


Figure 6.26: Case: $\epsilon < -1$ and $Q > \sqrt{9/8}M$. Parameter choice: $Q = 2M$ and $\epsilon = -2$. Circular orbits exist with angular momentum $L = L^+$ (gray curve) and energy $E = E^+$ (black curve).

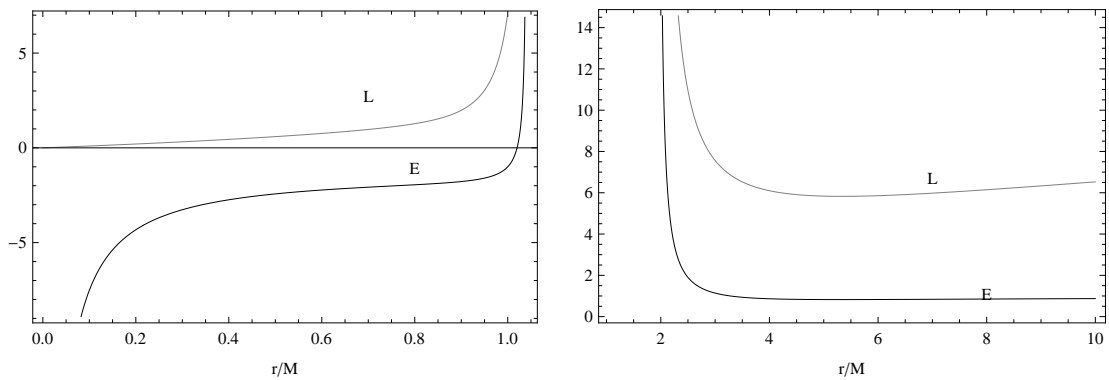


Figure 6.27: Case: $\epsilon < -1$ and $M < Q \leq \sqrt{9/8}M$. Parameter choice: $Q = 1.01M$ and $\epsilon = -2$. Then, $r_\gamma^- = 1.04196M$ and $r_\gamma^+ = 1.95804M$. Circular orbits exist with angular momentum $L = L^+$ (gray curve) and energy $E = E^+$ (black curve) in $0 < r < r_\gamma^-$ and $r > r_\gamma^+$.

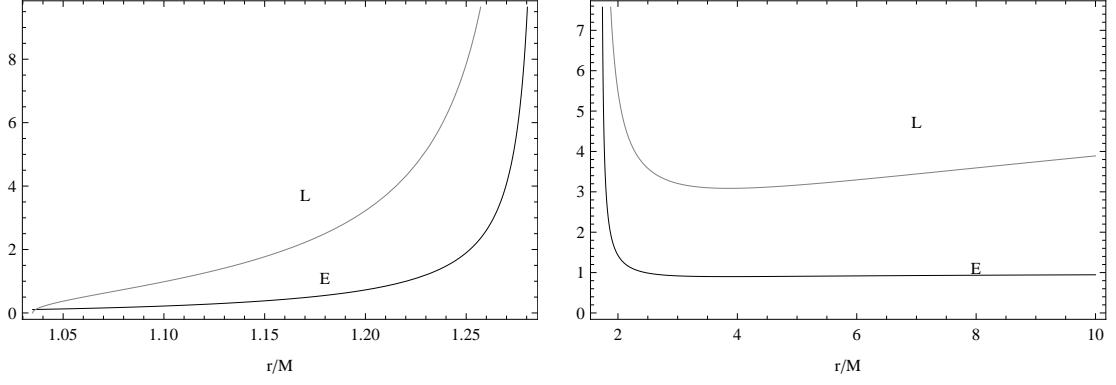


Figure 6.28: Case: $M < Q \leq \sqrt{9/8}M$ and $-M/Q < \epsilon < 0$. Parameter choice: $Q = 1.05M$ and $\epsilon = -0.2$. Then $r_\gamma^- = 1.28787M$, $r_\gamma^+ = 1.71213M$, and $r_s^- = 1.03487M$. Circular orbits exist with angular momentum $L = L^+$ (gray curve) and energy $E = E^+$ (black curve) in $r_s^- < r < r_\gamma^-$ (left plot) and in $r > r_\gamma^+$ (right plot). For $r = r_s^-$, $L = 0$.

approaches $r = 0$. However, the angular momentum, as seen by an observer located at infinity, decreases as the radius of the orbit decreases. In the region $M < Q \leq \sqrt{9/8}M$, two limiting orbits appear at r_γ^\pm , as in the neutral particle case [31].

6.4.4 Case $-1 < \epsilon < 0$

For this range of the ratio ϵ , it is also convenient to analyze separately the two cases $Q > \sqrt{9/8}M$ and $M < Q \leq \sqrt{9/8}M$. In each case it is necessary to analyze the explicit value of ϵ with respect to the ratio M/Q . Several cases arise in which we must find the regions where circular motion is allowed and the value of the angular momentum and energy of the rotating charged test particles.

We summarize the results in the following manner. There are two different configurations for the regions in which circular motion of charged test particles is allowed. The first one arises in the case $Q > \sqrt{9/8}M$, and consists in a continuous region that extends from a minimum radius r_{min} to infinity, in principle. The explicit value of the minimum radius depends on the value of ϵ and can be either r_s^- , r_s^+ , or $r_{min} = Q^2/(2M)$. In general, we find that particles standing on the minimum radius are characterized by $L = 0$, i. e., they are static with respect to a non-rotating observer located at infinity.

The second configuration appears for $M < Q \leq \sqrt{9/8}M$. It also extends from r_{min} to infinity, but inside it there is a forbidden region delimited by the radii r_γ^- and r_γ^+ . The configuration is therefore composed of two disconnected regions. At the minimum radius, test particles are characterized by $L = 0$. On the boundaries (r_γ^\pm) of the interior forbidden region only photons can stand on circular orbits. A particular example of this case is presented in Fig. 6.28.

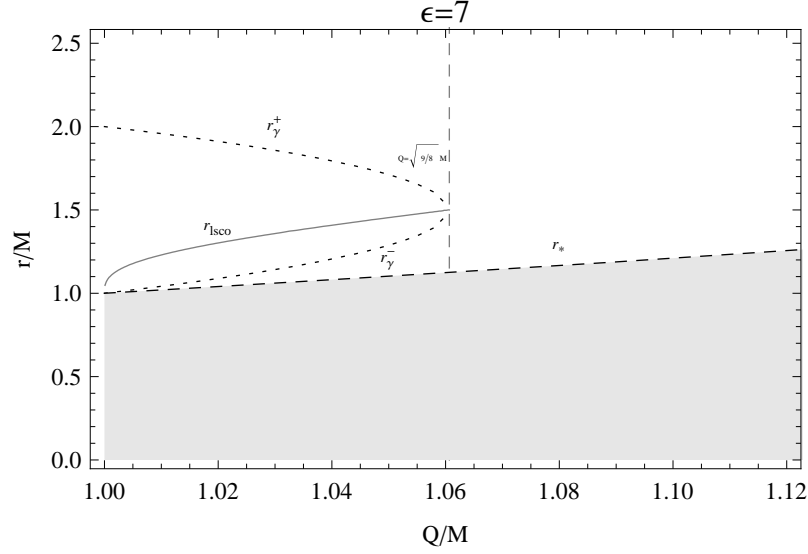


Figure 6.29: The radius of the last stable circular orbit r_{lSCO} (gray curve) of a charged particle with ratio $\epsilon = +7$ in a RN naked singularity with ratio $Q/M \in [1, 1.2]$. The radii $r_* = Q^2/M$ and $r = r_{\gamma}^{\pm} \equiv [3M \pm \sqrt{9M^2 - 8Q^2}]/2$ are also plotted. Circular orbits exist only in the interval $1 < Q/M < \sqrt{9/8}$. The shaded region is forbidden for timelike particles. Stable orbits are located in the region $r > r_{\text{lSCO}}$.

6.4.5 Stability

To explore the stability properties of the circular motion of charged test particles in a RN naked singularity, it is necessary to investigate the equation (6.2.7) or, equivalently, Eqs.(6.2.8), (6.2.8), and (6.2.9), considering the different values for ϵ and $Q/M > 1$. We can distinguish two different cases, $|\epsilon| > 1$ and $0 < |\epsilon| < 1$. Let us consider the case $|\epsilon| > 1$. In particular, as it was shown in Sec. 6.4.1, for $\epsilon > 1$ and $M < Q < \sqrt{9/8}M$ circular orbits exist with $L = L^+$ in the interval $r_{\gamma}^- < r < r_{\gamma}^+$ whereas no circular orbits exist for $\epsilon > 1$ and $Q > \sqrt{9/8}M$. For this particular case, a numerical analysis of condition (6.2.7) leads to the conclusion that a circular orbit is stable only if its radius r_0 satisfies the condition $r_0 > r_{\text{lSCO}}$, where r_{lSCO} is depicted in Fig. 6.29. We see that in general the radius of the last stable circular orbit is located inside the interval $(r_{\gamma}^-, r_{\gamma}^+)$. It then follows that the only stable region is determined by the interval $r_{\text{lSCO}} < r < r_{\gamma}^+$.

Consider now the case $\epsilon < -1$. The numerical investigation of the condition (6.2.7) for the last stable circular orbit shows that in this case there are two solutions r_{lSCO}^{\pm} such that $r_{\text{lSCO}}^- \leq r_{\text{lSCO}}^+$, where the equality is valid for $Q/M \approx 1.72$. Moreover, for $Q/M = \sqrt{9/8}$ we obtain that $r_{\text{lSCO}}^- = r_{\gamma}^- = r_{\gamma}^+$. This situation is illustrated in Fig. 6.30. Stable orbits corresponds to points located outside the region delimited by the curves $r = r_{\text{lSCO}}^+$, $r = r_{\text{lSCO}}^-$, and the axis $Q/M = 1$. On the other hand, we found in Sec. 6.4.3 that for $\epsilon < -1$ and $1 < Q/M \leq \sqrt{9/8}$

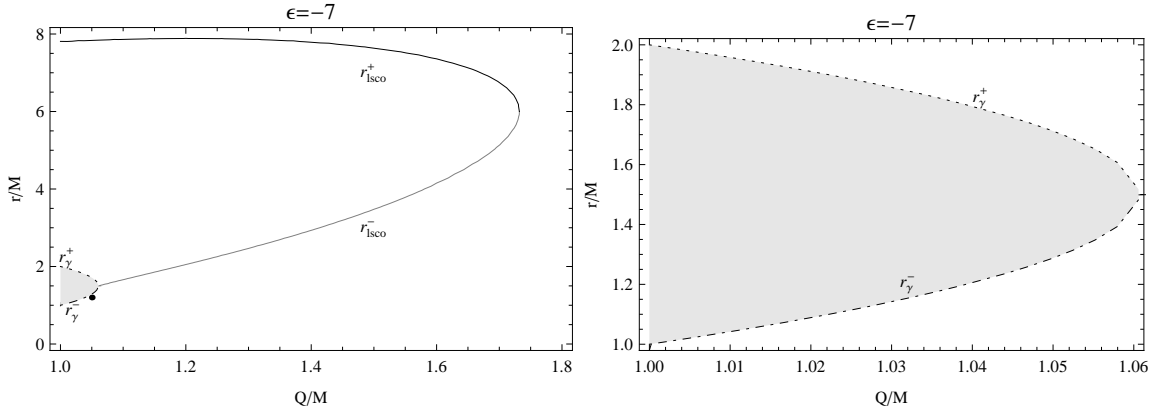


Figure 6.30: The radius of the last stable circular orbit r_{lSCO}^{\pm} (black curves) of a charged particle with ratio $\epsilon = -7$ in a RN naked singularity with ratio $Q/M \in [1, 1.8]$. The radii r_* , and r_{γ}^{\pm} are also plotted for comparison. In the shaded region no circular orbits can exist. Stable circular orbits are situated outside the region with boundaries r_{lSCO}^+ , r_{lSCO}^- , and the vertical axis $Q/M = 1$.

circular orbits exist in the interval $0 < r < r_{\gamma}^-$ and $r > r_{\gamma}^+$. It then follows that the region of stability corresponds in this case to two disconnected zones determined by $0 < r < r_{\gamma}^-$ and $r > r_{\text{lSCO}}^+$. Moreover, we established in Sec. 6.4.3 that for $\epsilon < -1$ and $\sqrt{9/8} < Q/M$ circular orbits always exist for $r > 0$. Consequently, in the interval $\sqrt{9/8} < Q/M \lesssim 1.72$, the stable circular orbits are located in the two disconnected regions defined by $0 < r < r_{\text{lSCO}}^-$ and $r > r_{\text{lSCO}}^+$. Finally, for $Q/M \gtrsim 1.72$ all the circular orbits are stable (see Fig. 6.30).

The case $0 < |\epsilon| < 1$ is much more complex, and needs to be described for different subcases following the classification of orbital regions traced in Sec. 6.4.2 for the case $0 < \epsilon < 1$, and in Sec. 6.4.4 for the case $-1 < \epsilon < 0$. The results for the specific ratio $\epsilon = 0.5$ are given in Fig. 6.31 and for $\epsilon = -0.5$ in Fig. 6.32. In general, we find that the results are similar to those obtained for the case $\epsilon < -1$. Indeed, the zone of stability consists of either one connected region or two disconnected regions. The explicit value of the radii that determine the boundaries of the stability regions depend on the particular values of the ratio Q/M .

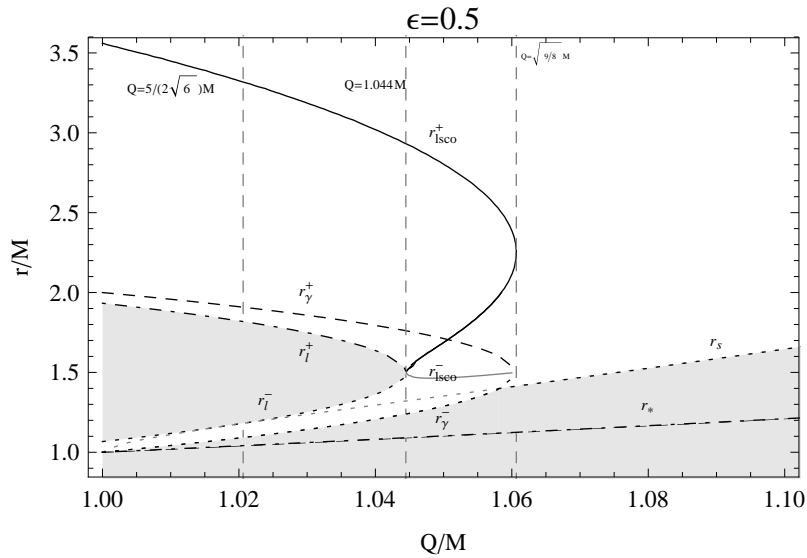


Figure 6.31: The radius of the last stable circular orbit r_{lsc}^{\pm} (black and grey curves) of a charged particle with ratio $\epsilon = 0.5$ in a RN naked singularity with ratio $Q/M \in [1, 1.1]$. Also plotted: $r_{\gamma}^{\pm} \equiv [3M \pm \sqrt{(9M^2 - 8Q^2)}]/2$, $r_s^+ \equiv \frac{Q^2}{e^2 Q^2 - M^2} [\sqrt{\epsilon^2(\epsilon^2 - 1)(M^2 - Q^2)}M(\epsilon^2 - 1)]$, $r_l^{\pm} \equiv \frac{3M}{2} \pm \frac{1}{2}\sqrt{9M^2 - 8Q^2 - Q^2\epsilon^2}$, and $r_* = Q^2/M$. Regions of stability are: for $Q > \sqrt{9/8}M$ in $r > r_s$, for $(3\sqrt{6}/7)M < Q < \sqrt{9/8}M$ exist stable orbits in $r_{\gamma}^- < r$, for $(5/(2\sqrt{6}))M < Q < (3\sqrt{6}/7)M$ exist stable orbits in $r_{\gamma}^- < r$. For $M < Q < (5/(2\sqrt{6}))M$ stable orbits are located in $r > r_{lsc}^+$.

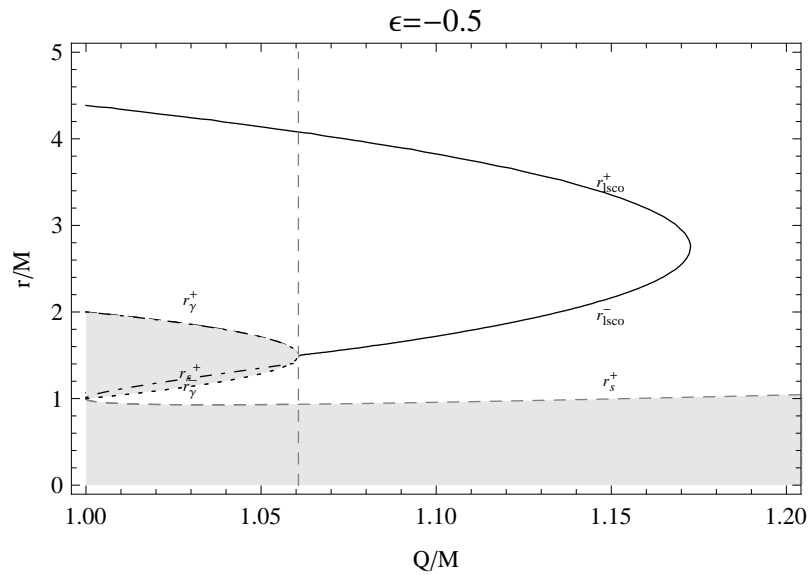


Figure 6.32: The radius of the last stable circular orbit r_{lSCO}^{\pm} (black and grey curves) of a charged particle with ratio $\epsilon = -0.5$ in a RN naked singularity with ratio $Q/M \in [1, 1.2]$. Also plotted: $r_{\gamma}^{\pm} \equiv [3M \pm \sqrt{(9M^2 - 8Q^2)}]/2$, $r_s^+ \equiv \frac{Q^2}{\epsilon^2 Q^2 - M^2} \left[\sqrt{\epsilon^2(\epsilon^2 - 1)(M^2 - Q^2)} M(\epsilon^2 - 1) \right]$, $r_l^{\pm} \equiv \frac{3M}{2} \pm \frac{1}{2} \sqrt{9M^2 - 8Q^2 - Q^2 \epsilon^2}$, and $r_* = Q^2/M$. Shaded regions are forbidden. Regions of stability are: for $Q > (\sqrt{9/8})M$ stable circular orbits exist in $r_s^+ < r < r_{lSCO}^-$, and $r > r_{lSCO}^+$. For $M < Q < (\sqrt{9/8})M$ stable circular orbits exist in $r_s^+ < r < r_{\gamma}^-$, and $r > r_{\gamma}^+$.

6.5 Velocity of test particles in a RN naked singularity

In this section explore charged test particles in circular motion in a RN naked singularity by using the tetrad formalism, as developed in Sec. 6.3 for the black hole analysis. In Sec. 6.4, we studied the timelike circular motion in the naked singularity case by analyzing directly the existence conditions for the energy, Eq. (6.2.3), and the angular momentum, Eq. (6.2.2). Here we use the formalism of “local proper linear velocity” as measured by an observer attached to an orthonormal frame. The results are equivalent to those obtained by using the expressions for the energy and angular momentum.

In Sec. 6.3, we showed that the linear velocity of a test particle in a RN spacetime can be written as

$$v_{\epsilon}^{\pm} = v_g \left[\Lambda \pm \sqrt{\Lambda^2 - 1 + (\epsilon/\epsilon_0)^2} \right]^{1/2}, \quad (6.5.1)$$

where

$$\Lambda = 1 - \frac{v_g^2}{2} \left(\frac{\epsilon}{\epsilon_0} \right)^2, \quad v_g = \sqrt{\frac{Mr - Q^2}{\Delta}}, \quad \epsilon_0 = \frac{Mr - Q^2}{Q\sqrt{\Delta}}. \quad (6.5.2)$$

Then, the conditions for the existence of timelike velocities are

$$\Lambda^2 - 1 + (\epsilon/\epsilon_0)^2 \geq 0, \quad (6.5.3)$$

$$\Lambda \pm \sqrt{\Lambda^2 - 1 + (\epsilon/\epsilon_0)^2} \geq 0, \quad (6.5.4)$$

$$(v_{\epsilon}^{\pm})^2 < 1. \quad (6.5.5)$$

We first note that, in the case of a naked singularity, these conditions can be satisfied only for $r \geq Q^2/M$.

For $\epsilon > 1$ and $\epsilon < -1$ the solutions are the geodesic velocities $v = \pm v_{\epsilon}^{\pm}$. In fact, in this case, condition (6.5.4) with the minus sign is no more satisfied. On the other hand, conditions (6.5.3), (6.5.4), and (6.5.5) imply that circular timelike orbits exist for $Q/M > \sqrt{9/8}$ in the entire range $r > Q^2/M$. For $1 < Q/M < \sqrt{9/8}$ circular orbits are possible in $r > Q^2/M$ and $r \neq r_{\gamma}^{\pm} \equiv [3M \pm \sqrt{9M^2 - 8Q^2}]/2$. Finally, for $Q/M = \sqrt{9/8}$ timelike circular orbits exist for all $r > Q^2/M$, except at $r = (3/2)M$. Moreover, the radii $r = r_{\gamma}^{\pm}$ correspond to photon orbits in the RN spacetime (see Fig. 6.33).

Consider now the case $|\epsilon| < 1$. It is useful to introduce here the following

notations:

$$r_l^\pm \equiv \frac{3M}{2} \pm \frac{1}{2} \sqrt{9M^2 - 8Q^2 - Q^2\epsilon^2}, \quad (6.5.6)$$

$$\tilde{\epsilon}_\pm \equiv \frac{1}{\sqrt{2}Q} \sqrt{5M^2 \pm 4Q^2 + \sqrt{25M^2 - 24Q^2}}, \quad (6.5.7)$$

and

$$r_s^\pm \equiv \frac{Q^2}{\epsilon^2 Q^2 - M^2} \left[M(\epsilon^2 - 1) \pm \sqrt{\epsilon^2(\epsilon^2 - 1)(M^2 - Q^2)} \right]. \quad (6.5.8)$$

First, consider the case $0 < \epsilon < 1$. For $\epsilon > 0$ condition (6.3.12) implies that $r > Q^2/M$. Applying this constraint on conditions (6.5.3) and (6.5.4), we obtain the following results for timelike geodesics.

1. For $1 < Q/M \leq 5/(2\sqrt{6})$ the following subcases occur:

a) $0 < \epsilon < \tilde{\epsilon}_-$: Fig. 6.34a

The velocity $v = \pm v_\epsilon^+$ exists in the range $Q^2/M < r \leq r_l^-$ and $r \geq r_l^+$ with $r \neq r_\gamma^\pm$, $v = \pm v_\epsilon^-$ exists in the range $r_s^+ < r \leq r_l^-$ and $r \geq r_l^+$.

b) $\tilde{\epsilon}_- \leq \epsilon \leq \tilde{\epsilon}_+$: Fig. 6.34b

The velocity $v = \pm v_\epsilon^+$ exists in the range $Q^2/M < r < r_l^-$ and $r \geq r_l^+$ with $r \neq r_\gamma^\pm$, $v = \pm v_\epsilon^-$ exists in the range $r \geq r_l^+$.

c) $\tilde{\epsilon}_+ < \epsilon < \epsilon_l$: Fig. 6.34.c

The velocity $v = \pm v_\epsilon^+$ exists in the range $Q^2/M < r \leq r_l^-$ and $r \geq r_l^+$ with $r \neq r_\gamma^\pm$, $v = \pm v_\epsilon^-$ exists in the range $r_s^+ < r \leq r_l^-$ and $r \geq r_l^+$.

d) $\epsilon_l \leq \epsilon < 1$: Fig. 6.34d

The solutions are the geodesic velocities $v = \pm v_\epsilon^+$ in the range $r > Q^2/M$ with $r \neq r_\gamma^\pm$. The solution $v = \pm v_\epsilon^-$ exists for $\epsilon_l \leq \epsilon < M/Q$ in the range $r > r_s^+$.

2. For $5/(2\sqrt{6}) < Q/M < \sqrt{9/8}$ the following subcases occur:

a) $0 < \epsilon < \epsilon_l$: Fig. 6.35b

The velocity $v = \pm v_\epsilon^+$ exists in the range $Q^2/M < r \leq r_l^-$ and $r > r_l^+$ with $r \neq r_\gamma^\pm$, $v = \pm v_\epsilon^-$ exists in the range $r_s^+ < r \leq r_l^-$ and

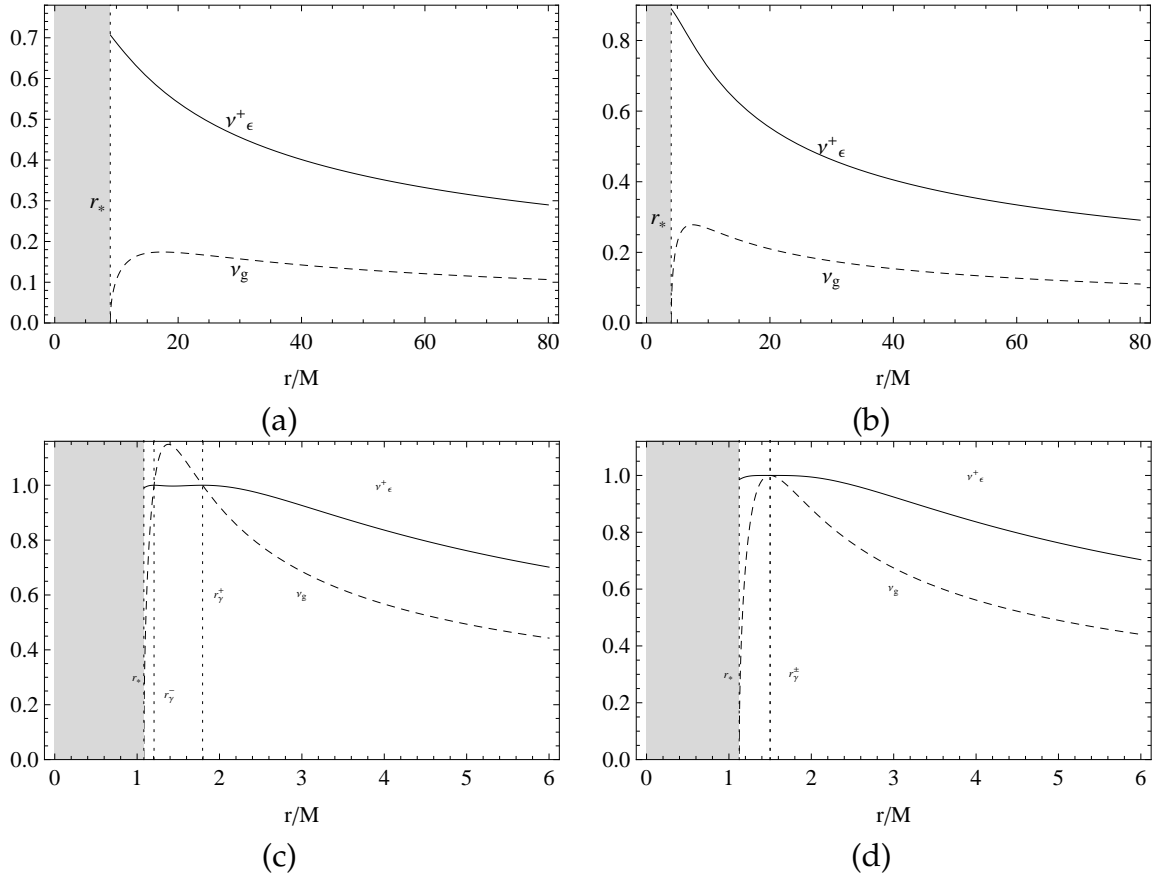


Figure 6.33: The positive solution of the linear velocity v_ϵ^+ is plotted as a function of the radial distance r/M for different values of the ratios Q/M and ϵ . The geodesic velocity v_g is also shown (dashed curve). Shaded region is forbidden. In (a) the parameter choice is $Q/M = 3$ and $\epsilon = 2$, with $r_* \equiv Q^2/M = 9M$. In (b) the parameter choice is $Q/M = 2$ and $\epsilon = 3$, with $r_* \equiv Q^2/M = 4M$. In (c) the parameter choice is $Q/M = 1.04$ and $\epsilon = 2$, with $r_* \equiv Q^2/M \approx 1.08M$, $r_\gamma^+ \equiv [3M + \sqrt{9M^2 - 8Q^2}]/2 \approx 1.79M$, and $r_\gamma^- \equiv [3M - \sqrt{9M^2 - 8Q^2}]/2 \approx 1.201M$. In (d) the parameter choice is $Q/M = \sqrt{9/8}$ and $\epsilon = 2$, with $r_* \equiv Q^2/M = (9/8)M$, $r_\gamma^\pm \equiv [3M \pm \sqrt{9M^2 - 8Q^2}]/2 = (3/2)M$.

$$r \geq r_l^+.$$

b) $\epsilon_l \leq \epsilon < 1$: Fig. 6.35a

The velocity $v = \pm v_\epsilon^+$ exists in the range $r > Q^2/M$, $v = \pm v_\epsilon^-$ exists in the range $r > r_s^+$.

3. $Q/M \geq \sqrt{9/8}$: Figs. 6.36 and 6.37

The velocity $v = \pm v_\epsilon^+$ exists in the range $r > Q^2/M$ for $Q/M > \sqrt{9/8}$ whereas for $Q/M = \sqrt{9/8}$ this is a solution in $r/M > 9/8$ with $r/M \neq 3/2$, $v = \pm v_\epsilon^-$ exists for $0 < \epsilon < M/Q$ in the range $r > r_s^+$.

The results for $-1 < \epsilon < 0$ are summarized below.

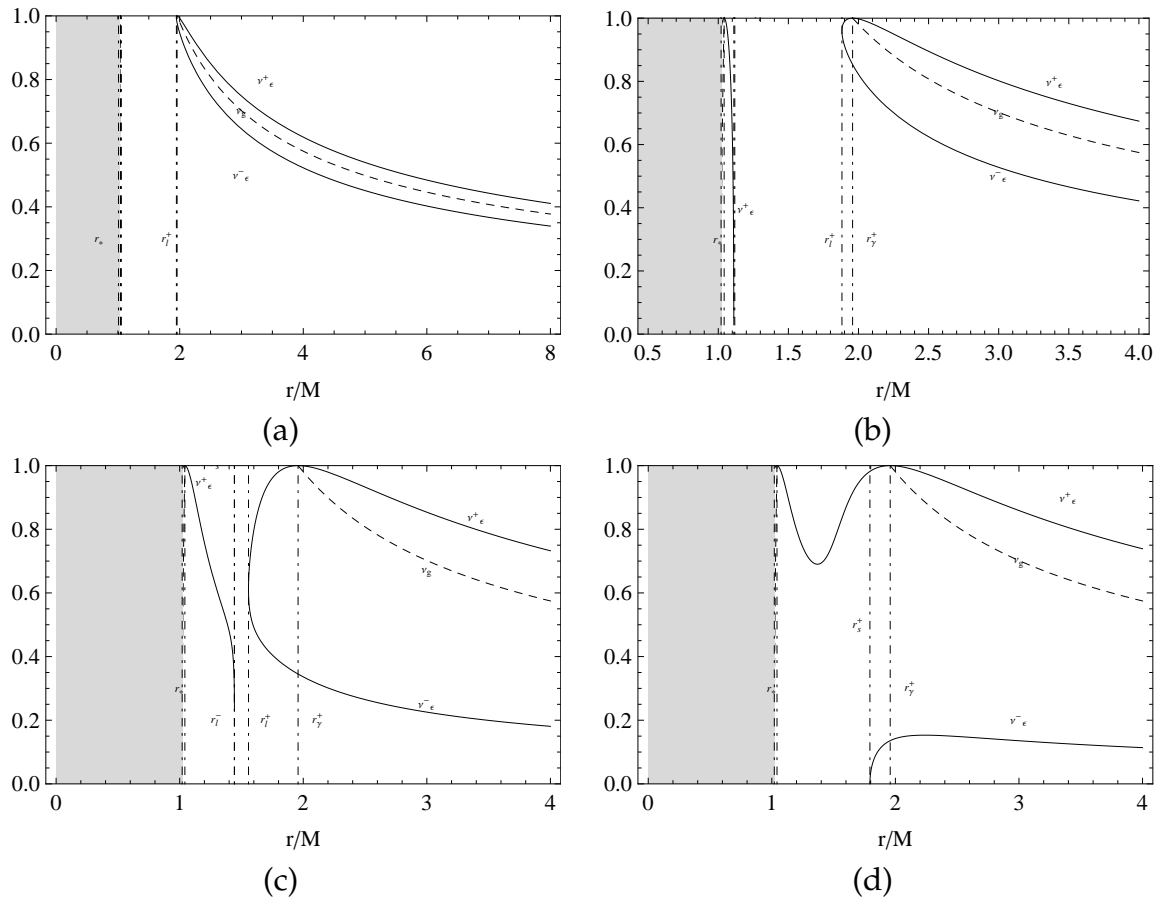


Figure 6.34: The positive solution of the linear velocity v_ϵ is plotted as a function of the radial distance r/M for $Q/M = 1.01$ and different values of the ratio ϵ . In this case $r_\gamma^+ = 1.96M$, $r_\gamma^- = 1.042M$ with $r_* \equiv Q^2/M = 1.02M$, $\tilde{e}_- = 0.31$, $\tilde{e}_+ = 0.9$, $e_l \approx 0.91$. The geodesic velocity v_g is also shown (dashed curve). Shaded region is forbidden. In (a) the parameter choice is $\epsilon = 0.2$ with $r_s^+ = 1.05M$, and $r_l^+ = 1.95M$, $r_l^- = 1.05M$. In (b) the parameter choice is $\epsilon = 0.5$. Here $r_s^+ = 1.11M$, and $r_l^+ = 1.88M$, $r_l^- = 1.12M$. In (c) the parameter choice is $\epsilon = 0.9$. Here $r_s^+ = 1.11M$, and $r_l^+ = 1.88M$, $r_l^- = 1.12M$. In (d) the parameter choice is $\epsilon = 0.95$. Here $r_s^+ = 1.79M$, and r_l^\pm do not exist.

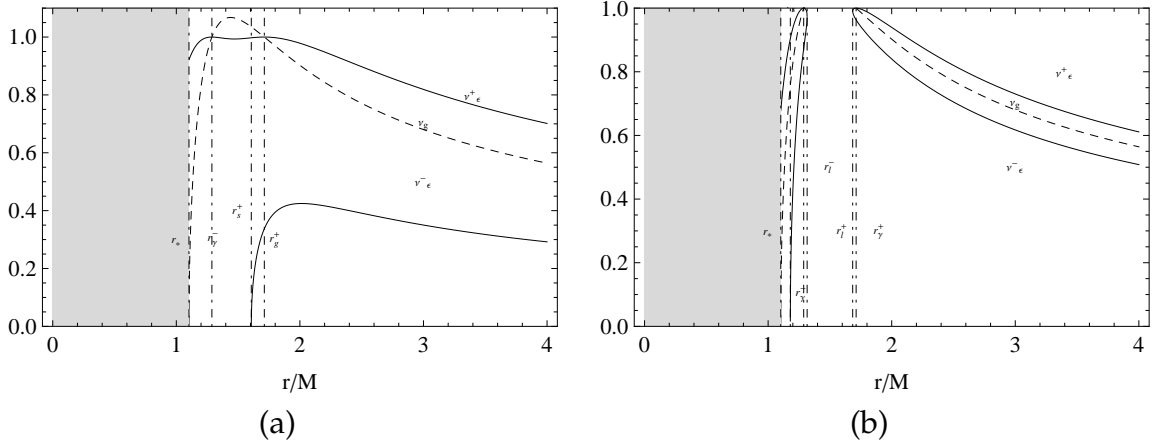


Figure 6.35: The positive solution of the linear velocity v_ϵ is plotted as a function of the radial distance r/M for $Q/M = 1.05$ and different values of the ratio ϵ . In this case $r_\gamma^+ = 1.71M$, $r_\gamma^- = 1.29M$ with $r_* \equiv Q^2/M \approx 1.102M$, $\epsilon_l \approx 0.40$. The geodesic velocity v_g is also shown (dashed curve). Shaded region is forbidden. In (a) the parameter choice is $\epsilon = 0.7$. Here $r_s^+ = 1.61M$, and r_l^\pm are not defined. In (b) the parameter choice is $\epsilon = 0.2$. Here $r_s^+ = 1.2M$, and $r_l^+ = 1.68M$, $r_l^- = 1.32M$.

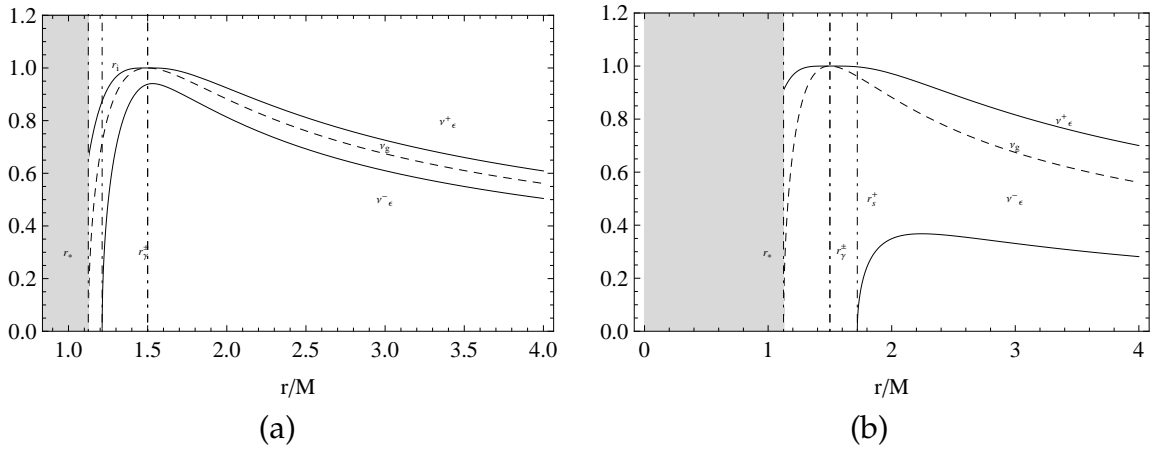


Figure 6.36: The positive solution of the linear velocity v_ϵ is plotted as a function of the radial distance r/M for $Q/M = \sqrt{9/8}$ and different values of the ratio ϵ . In this case $r_\gamma^+ = r_\gamma^- = 3/2M$ with $r_* \equiv 9/8M$, $\epsilon_l = 0$. The geodesic velocity v_g is also shown (dashed curve). Shaded region is forbidden. In (a) the parameter choice is $\epsilon = 0.2$ with $r_s^+ = 1.2M$. In (b) the parameter choice is $\epsilon = 0.7$ with $r_s^+ = 1.72M$.

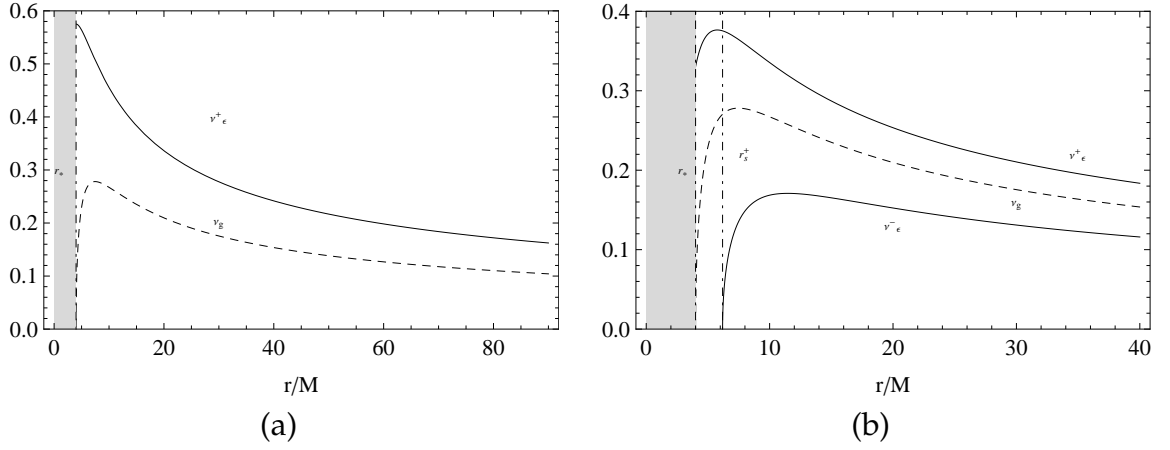


Figure 6.37: The positive solution of the linear velocity v_ϵ is plotted as a function of the radial distance r/M for $Q/M = 2$ and different values of the ratio ϵ . In this case $r_* \equiv Q^2/M \approx 4M$. The geodesic velocity v_g is also shown (dashed curve). Shaded region is forbidden. In (a) the parameter choice is $\epsilon = 0.7$ with $r_s^+ = 1.48M$. In (b) the parameter choice is $\epsilon = 0.2$ with $r_s^+ = 6.2M$.

1. For $1 < Q/M \leq 5/(2\sqrt{6})$ the following subcases occur:

- a) For $-1 < \epsilon \leq -\epsilon_l$, the velocity $v = \pm v_\epsilon^+$ exists in the range $r > Q^2/M$ with $r \neq r_\gamma^\pm$, $v = \pm v_\epsilon^-$ exists for $-(M/Q) < \epsilon \leq -\epsilon_l$ in the range $r > r_s^+$ (see Fig. 6.38a).
- b) For $-\epsilon_l < \epsilon < -\tilde{\epsilon}_+$, the solution is $v = \pm v_\epsilon^+$ in the range $Q^2/M < r \leq r_l^-$ and $r \geq r_l^+$ with $r \neq r_\gamma^\pm$, $v = \pm v_\epsilon^-$ exists in the range $r_s^+ < r \leq r_l^-$ and $r \geq r_l^+$ (see Fig. 6.38b).
- c) For $-\tilde{\epsilon}_+ \leq \epsilon \leq -\tilde{\epsilon}_-$, the velocity $v = \pm v_\epsilon^-$ exists in the range $r \geq r_l^+$. $v = \pm v_\epsilon^+$ exists for $-\tilde{\epsilon}_+ < \epsilon < -\tilde{\epsilon}_-$ in the range $(Q^2/M) < r < r_s^+$, and $r \geq r_l^+$ with $r \neq r_\gamma^\pm$, and for $\epsilon = -\tilde{\epsilon}^\pm$ the velocity v_ϵ^+ exists for $Q^2/M < r < r_l^-$ and $r \geq r_l^+$ with $r \neq r_\gamma^\pm$. Finally, for $Q = 5/(2\sqrt{6})M$ and $\epsilon = -\tilde{\epsilon}_+$, v_ϵ^+ exists for $(Q^2/M) < r < r_l^-$, and $r \geq r_l^+$ (see Fig. 6.38c).
- d) For $-\tilde{\epsilon}_- < \epsilon < 0$, the solutions are the geodesic velocities $v = \pm v_\epsilon^+$ in the range $(Q^2/M) < r \leq r_l^-$ and $r \geq r_l^+$ with $r \neq r_\gamma^\pm$. The solution $v = \pm v_\epsilon^-$ exists in $r_s^+ < r \leq r_l^-$ and $r \geq r_l^+$ (see Fig. 6.38d).

2. For $5/(2\sqrt{6}) < Q/M < \sqrt{9/8}$ the following subcases occur:

- a) For $-1 < \epsilon \leq -\epsilon_l$, the velocity $v = \pm v_\epsilon^+$ exists in the range $r > Q^2/M$ with $r \neq r_\gamma^\pm$, $v = \pm v_\epsilon^-$ exists for $-(M/Q) < \epsilon \leq -\epsilon_l$ in the range $r > r_s^+$ (see Fig. 6.39b).
- b) For $-\epsilon_l \leq \epsilon < 0$, the velocity $v = \pm v_\epsilon^+$ exists in the range $Q^2/M < r \leq r_l^-$ and $r \geq r_l^+$, $r \neq r_\gamma^\pm$, $v = \pm v_\epsilon^-$ exists in the range $r_s^+ < r \leq r_l^-$ and $r \geq r_l^+$ (see Fig. 6.39a).
3. For $Q/M \geq \sqrt{9/8}$ the velocity $v = \pm v_\epsilon^-$ exists for $-(M/Q) < \epsilon < 0$ in the range $r > r_s^+$. $v = \pm v_\epsilon^+$ is a solution for $Q/M > \sqrt{9/8}$ and $-1 < \epsilon < 0$ in $r > Q^2/M$ whereas for $Q/M = \sqrt{9/8}$ this is a solution in $r/M > 9/8$ with $r/M \neq 3/2$ (see Figs. 6.40 and 6.41).

6.6 Remarks

In this work, we explored the motion of charged test particles along circular orbits in the spacetime described by the Reissner–Nordström (RN) metric. We performed a very detailed discussion of all the regions of the spacetime where circular orbits are allowed, using as parameters the charge–to–mass ratio Q/M of the source of gravity and the charge–to–mass ratio $\epsilon = q/\mu$ of the test particle. Depending on the value of Q/M , two major cases must be considered: The black hole case, $|Q/M| \leq 1$, and the naked singularity case, $|Q/M| > 1$. Moreover, we found out that the two cases $|\epsilon| \leq 1$ and $|\epsilon| > 1$ must also be investigated separately. Whereas the investigation of the motion of charged test particles with $|\epsilon| > 1$ can be carried out in a relatively simple manner, the case with $|\epsilon| \leq 1$ is much more complex, because it is necessary to consider various subcases which depend on the explicit value of ϵ in this interval.

To perform the analysis of circular motion of charged test particles in this gravitational field we use two different methods. The first one consists in using constants of motion to reduce the equations of motion to a single first-order differential equation for a particle moving in an effective potential. The properties of this effective potential are then used to find the conditions under which circular motion is possible. The second approach uses a local orthonormal frame to introduce a “local proper linear velocity” for the test particle. The conditions for this velocity to be timelike are then used to determine the regions of space where circular orbits are allowed. The results of both methods are equivalent and, in fact, for the sake of simplicity it is sometimes convenient to use a combination of both approaches. In this work, we analyzed in detail the conditions for the existence of circular orbits and found all the solutions for all the regions of space in the case of black holes and naked singularities.

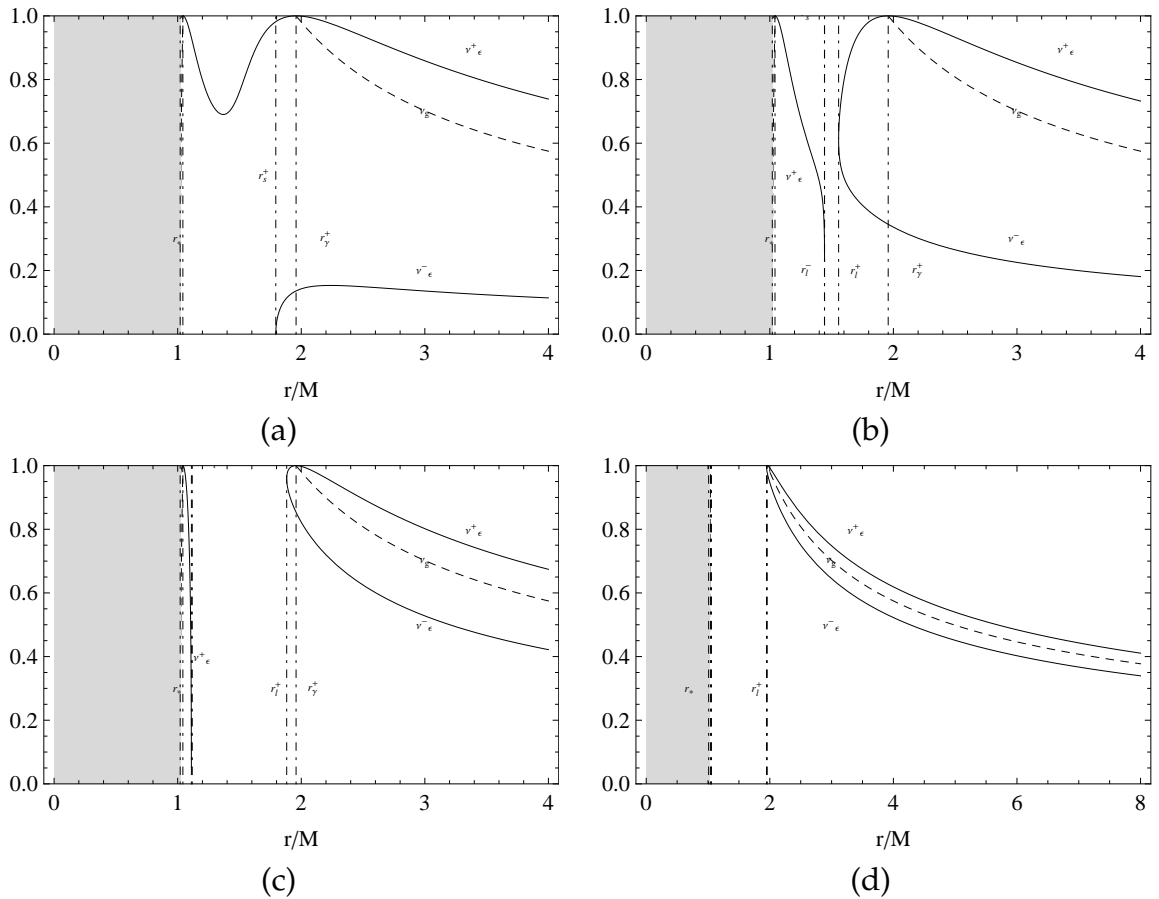


Figure 6.38: The positive solution of the linear velocity v_ϵ is plotted as a function of the radial distance r/M for $Q/M = 1.01$ and different values of the ratio ϵ . In this case $r_\gamma^+ = 1.96M$, $r_\gamma^- = 1.042M$, $r_* \equiv Q^2/M = 1.02M$, $\tilde{\epsilon}_- = 0.31$, $\tilde{\epsilon}_+ = 0.9$, and $\epsilon_l \approx 0.91$. The geodesic velocity v_g is also shown (dashed curve). Shaded region is forbidden. In (a) the parameter choice is $\epsilon = -0.95$. Here $r_s^+ = 1.79M$, and r_l^\pm do not exist. In (b) the parameter choice is $\epsilon = -0.9$. Here $r_s^+ = 1.11M$, $r_l^+ = 1.88M$, and $r_l^- = 1.12M$. In (c) the parameter choice is $\epsilon = -0.5$. Here $r_s^+ = 1.11M$, $r_l^+ = 1.88M$, and $r_l^- = 1.12M$. In (d) the parameter choice is $\epsilon = -0.2$. Here $r_s^+ = 1.05M$, $r_l^+ = 1.95M$, and $r_l^- = 1.05M$.

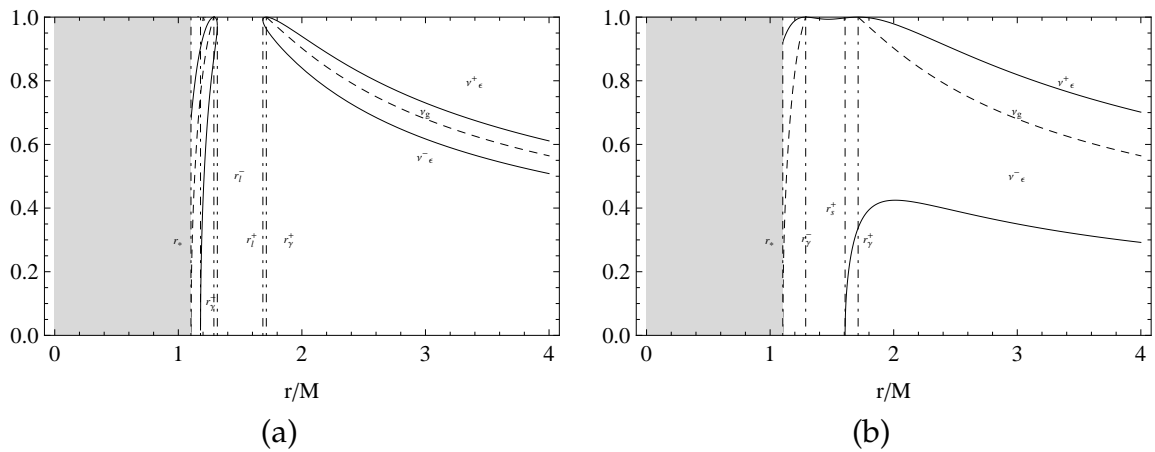


Figure 6.39: The positive solution of the linear velocity v_ϵ is plotted as a function of the radial distance r/M for $Q/M = 1.05$ and different values of the ratio ϵ . In this case $r_\gamma^+ = 1.71M$, $r_\gamma^- = 1.29M$, $r_* \equiv Q^2/M \approx 1.102M$, and $\epsilon_l \approx 0.40$. The geodesic velocity v_g is also shown (dashed curve). Shaded region is forbidden. In (a) the parameter choice is $\epsilon = -0.2$. Here $r_s^+ = 1.2M$, $r_l^+ = 1.68M$, and $r_l^- = 1.32M$. In (b) the parameter choice is $\epsilon = -0.7$. Here $r_s^+ = 1.61M$, and r_l^\pm are not defined.

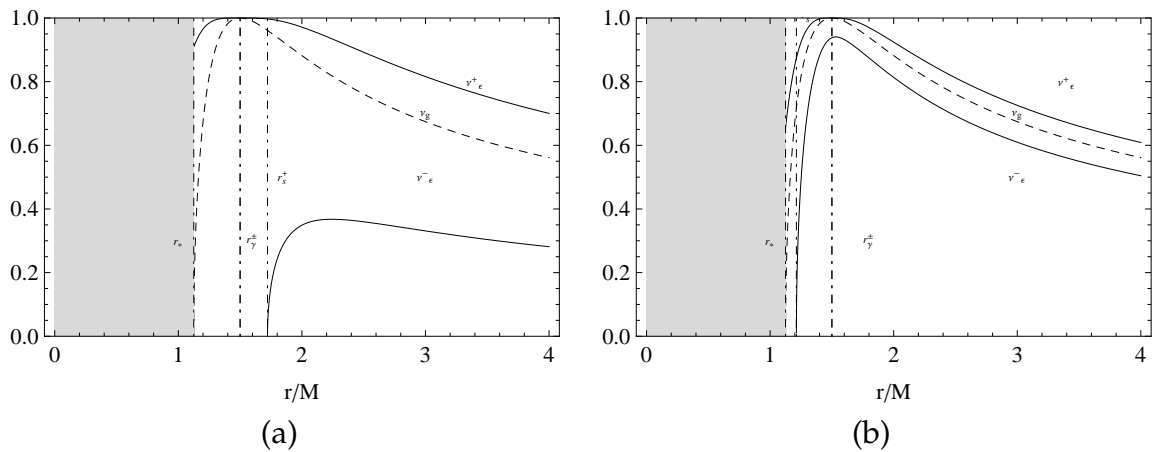


Figure 6.40: The positive solution of the linear velocity v_ϵ is plotted as a function of the radial distance r/M for $Q/M = \sqrt{9/8}$ and different values of the ratio ϵ . In this case $r_\gamma^+ = r_\gamma^- = 3/2M$, $r_* \equiv 9/8M$, and $\epsilon_l = 0$. The geodesic velocity v_g is also shown (dashed curve). Shaded region is forbidden. In (a) the parameter choice is $\epsilon = -0.7$ with $r_s^+ = 1.72M$. In (b) the parameter choice is $\epsilon = -0.2$ with $r_s^+ = 1.2M$.

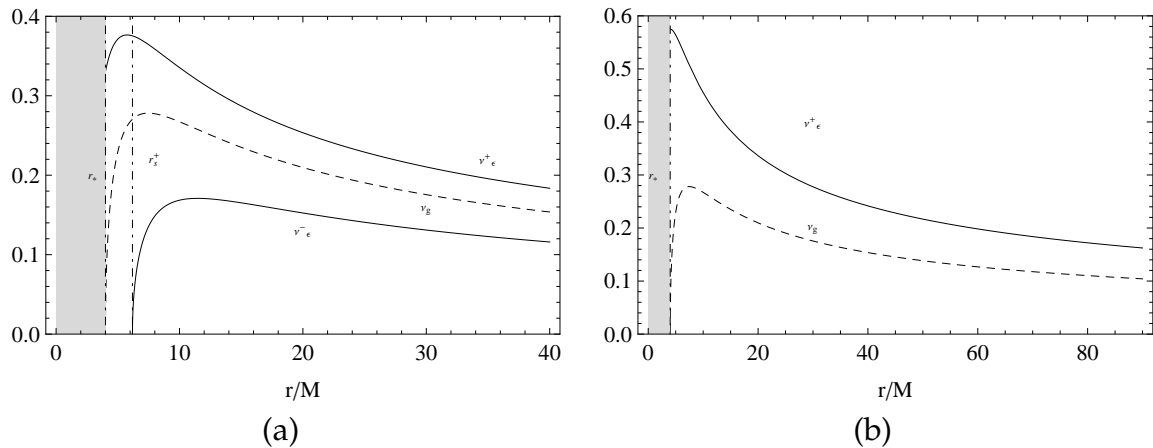


Figure 6.41: The positive solution of the linear velocity v_ϵ is plotted as a function of the radial distance r/M for $Q/M = 2$ and different values of the ratio ϵ . In this case $r_* \equiv Q^2/M \approx 4M$. The geodesic velocity v_g is also shown (dashed curve). Shaded region is forbidden. In (a) the parameter choice is $\epsilon = -0.2$. Here $r_s^+ = 6.2M$. In (b) the parameter choice is $\epsilon = -0.7$. Here $r_s^+ = 1.48M$.

To formulate the main results of this work in a plausible manner, let us suppose that an accretion disk around a RN gravitational source can be made of test particles moving along circular orbits [68]. Then, in the case of black hole we find two different types of accretion disks made of charged test particles. The first type consists of a disk that begins at a minimum radius R and can extend to infinity, in principle. In the second possible configuration, we find a circular ring of charged particles with radii (r_{int}, r_{ext}) , surrounded by the disk, i. e., with $r_{ext} < R$. For certain choices of the parameter ϵ the exterior disk might be composed only of neutral particles. A study of the stability of circular orbits shows that the second structure of a ring plus a disk is highly unstable. This means that test particles in stable circular motion around RN black holes can be put together to form only a single disk that can, in principle, extend to infinity.

In the case of RN naked singularities we find the same two types of accretion disks. The explicit values of the radii r_{min} , r_{ext} , and R depend on the values of the ratios ϵ and Q/M , and differ significantly from the case of black holes. In fact, we find that the case of naked singularities offers a much richer combination of values of the charge–to–mass ratios for which it is possible to find a structure composed of an interior ring plus an exterior disk. A study of the stability of this specific situation shows that for certain quite general combinations of the parameters the configuration is stable. This result implies that test particles in stable circular motion around RN naked singularities can be put together to form either a single disk that can extend, in principle, to infinity or a configuration of an interior ring with an exterior disk. This is the main difference between black holes and naked singularities from the viewpoint of these hypothetical accretion disks made of test particles.

The question arises whether it is possible to generalize these results to the case of more realistic accretion disks around more general gravitational sources, taking into account, for instance, the rotation of the central body, [69, 70]. It seems reasonable to expect that in the case of Kerr and Kerr–Newman naked singularities, regions can be found where stable circular motion is not allowed so that an accretion disk around such an object would exhibit a discontinuous structure. Indeed, some preliminary calculations of circular geodesics in the field of rotating compact objects support this expectation. Thus, we can conjecture that the discontinuities in the accretion disks around naked singularities are a consequence of the intensity of the repulsive gravity effects that characterize these speculative objects. Furthermore, it was recently proposed that static compact objects with quadrupole moment can be interpreted as describing the exterior gravitational field of naked singularities [71, 72]. It would be interesting to test the above conjecture in this relatively simple case in which rotation is absent. If the conjecture turns out to be true, it would give us the possibility of distinguishing between black holes and naked singularities by observing their accretion disks.

7 Equatorial circular motion in Kerr spacetime

7.1 Introduction

The Kerr spacetime describes the exterior gravitational field of a rotating mass M with specific angular momentum $a = J/M$, where J is the total angular momentum of the gravitational source. In Boyer–Lindquist coordinates, the Kerr metric has the form

$$ds^2 = dt^2 - \frac{\rho^2}{\Delta} dr^2 - \rho^2 d\theta^2 - (r^2 + a^2) \sin^2 \theta d\phi^2 - \frac{2M}{\rho^2} r (dt - a \sin^2 \theta d\phi)^2, \quad (7.1.1)$$

where

$$\Delta \equiv r^2 - 2Mr + a^2, \quad \text{and} \quad \rho^2 \equiv r^2 + a^2 \cos^2 \theta. \quad (7.1.2)$$

This metric is an axisymmetric, stationary (nonstatic) asymptotically flat solution of Einstein equations in vacuum. The redshift infinity surface and event horizons are described respectively by the equations

$$g_{tt} = 0, \quad g^{rr} = 0. \quad (7.1.3)$$

Then, the solutions of these equations are respectively

$$r_{\pm}^0 = M \pm \sqrt{M^2 - a^2 \cos^2 \theta}, \quad \text{and} \quad r_{\pm} = M \pm \sqrt{M^2 - a^2}. \quad (7.1.4)$$

Considering that $\theta \in [0, \pi]$, the radii r_{\pm}^0 and r_{\pm} exist when $|a| \leq M$ (Kerr black hole); in particular, for $|a| = M$ (extreme Kerr black hole) the two horizons coincide, $r_+ = r_- = M$. The outer static limit is r_+^0 , it corresponds to the outer boundary of the ergosphere.

A naked singularity case occurs when $|a| > M$ (for more details about the Kerr metric see, for instance, [21, 73, 74] and [75, 76, 77, 78]).

The most important limiting cases are the Schwarzschild metric which is recovered for $a = 0$, and the Minkowski metric of special relativity for $a = M = 0$. The Kerr metric in Boyer–Lindquist coordinates is singular when $\rho = 0$ and when $\Delta = 0$. However, a calculation of the Kretschmann curvature scalar reveals that a true curvature singularity occurs only for $\rho = 0$. Therefore, the surface represented by $r = 0$ and $\theta = \pi/2$ corresponds to an

intrinsic curvature singularity [79, 21, 73, 80].

In previous works [32, 31, 81], the motion of test particles along circular orbits around static, spherically symmetric spacetimes was investigated in detail. We are now interested in studying the more general case of a stationary, axisymmetric spacetimes. The study of the circular motion around compact objects is of particular interest in the context of astrophysics. Indeed, an infinitesimal thin disk of test particles traveling in circular orbits can be considered as an idealized model for an accretion disk of matter surrounding the central body. Such an idealized model could be used, for instance, to estimate the amount of energy released by matter being accreted by the central mass [82]. In addition, one can ask the question whether this hypothetical accretion disk carries information about the nature of the central compact object. In a recent work [32, 31, 81], this question was answered positively. Indeed, we found that the geometric structure of the infinitesimal thin disk around a Reissner-Nordström compact object strongly depends on the mass-to-charge ratio.

In the present work, we generalize our previous analysis and study the motion of test particles along circular orbits on the equatorial plane of the Kerr spacetime. We are especially interested in studying the differences between the gravitational field of black holes and naked singularities. Test particles moving along circular orbits are particularly appropriate to measure the effects generated by naked singularities. For the sake of simplicity, we limit ourselves to the case of equatorial trajectories because they are confined in the equatorial geodesic plane. This is a consequence of the fact that the Kerr solution is invariant under reflections with respect to the equatorial plane. Non-equatorial geodesics present an additional difficulty because the corresponding planes are not geodesic. This case will not be considered in the present work.

7.2 Circular orbits

We consider the circular motion of a test particle of mass μ in the background represented by the Kerr metric (7.1.1). We limit ourselves to the case of orbits situated on the equatorial plane only which are defined by means of the conditions

$$\theta = \pi/2, \quad \text{and} \quad \frac{d\theta}{d\tau} = 0, \quad (7.2.1)$$

where τ is the particle's proper time. We note that for $\theta = \pi/2$ the outer boundary of the ergosphere Eq. (7.1.4) is $r_+^0 = 2M$ while $r_-^0 = 0$.

The tangent vector u^a to a curve $x^\alpha(\tau)$ is $u^\alpha = dx^\alpha/d\tau = \dot{x}^\alpha$. The momentum $p^\alpha = \mu\dot{x}^\alpha$ of a particle with mass μ can be normalized so that $g_{\alpha\beta}\dot{x}^\alpha\dot{x}^\beta = -k$, where $k = 0, 1, -1$ for null, spacelike and timelike curves, respectively.

Since the metric is independent of ϕ and t , the covariant components p_ϕ

and p_t of the particle's four-momentum are conserved along its geodesic. Thus, we use the fact that the quantity

$$E \equiv -g_{\alpha\beta}\zeta_t^\alpha p^\beta \quad (7.2.2)$$

is a constant of motion, where $\zeta_t = \partial_t$ is the Killing field representing stationarity. In general, we may interpret E , for timelike geodesics, as representing the total energy of the test particle for a particle coming from radial infinity, as measured by a static observer at infinity. On the other hand, the rotational Killing field $\zeta_\phi = \partial_\phi$ yields the following constant of motion

$$L \equiv g_{\alpha\beta}\zeta_\phi^\alpha p^\beta. \quad (7.2.3)$$

We interpret L as the angular momentum of the particle.

In this work, we analyze circular orbits involving a potential function $V(r)$. It represents that value of E/μ that makes r into a "turning point" ($V = E/\mu$), in other words, that value of E/μ at which the (radial) kinetic energy of the particle vanishes [83]. The (positive) effective potential is

$$V = -\frac{B}{2A} + \frac{\sqrt{B^2 - 4AC}}{2A}, \quad (7.2.4)$$

where [79, 21, 73, 74, 80]

$$A \equiv (r^2 + a^2)^2 - a^2\Delta, \quad (7.2.5)$$

$$B \equiv -2aL(r^2 + a^2 - \Delta), \quad (7.2.6)$$

$$C \equiv a^2L^2 - (M^2r^2 + L^2)\Delta. \quad (7.2.7)$$

The negative solution of the effective potential equation

$$V^- \equiv -\frac{B}{2A} - \frac{\sqrt{B^2 - 4AC}}{2A} \quad (7.2.8)$$

can be studied by using the following symmetry

$$V(L) = -V^-(-L). \quad (7.2.9)$$

We can note that the potential function (7.2.4) is invariant under the mutual transformation $a \rightarrow -a$ and $L \rightarrow -L$. Therefore, we will limit our analysis to the case of positive values of a for co-rotating ($L > 0$) and counter-rotating orbits ($L < 0$).

The investigation of the motion of test particles in the spacetime (7.1.1) is thus reduced to the study of motion in the effective potential V . We will focus

on (timelike) circular orbits for which (see also [84])

$$\dot{r} = 0, \quad V = E/\mu, \quad \partial V/\partial r = 0. \quad (7.2.10)$$

Moreover, we use the following notation for the angular momentum solutions

$$\frac{L_{\pm}}{\mu M} \equiv \frac{\left| \frac{a^2}{M^2} \pm 2\frac{a}{M} \sqrt{\frac{r}{M} + \frac{r^2}{M^2}} \right|}{\sqrt{\frac{r^2}{M^2} \left(\frac{r}{M} - 3 \right) \mp 2\frac{a}{M} \sqrt{\frac{r^3}{M^3}}}}, \quad (7.2.11)$$

and the corresponding energies

$$\frac{E_{\pm}^{(+)}}{\mu} \equiv \frac{E(L_{\pm})}{\mu} = \frac{(r^5 M)^{1/4} \left| [a^2 + (r-2M)r] \left(a \mp \sqrt{\frac{r^3}{M}} \right) \right|}{\sqrt{(r-3M)\sqrt{\frac{r}{M} \mp 2a}} + 2arL_{\pm}} + 2arL_{\pm}, \quad (7.2.12)$$

$$r [r^3 + a^2(r + 2M)]$$

and

$$\frac{E_{\pm}^{(-)}}{\mu} \equiv \frac{E(-L_{\pm})}{\mu} = \frac{(r^5 M)^{1/4} \left| [a^2 + (r-2M)r] \left(a \mp \sqrt{\frac{r^3}{M}} \right) \right|}{\sqrt{(r-3M)\sqrt{\frac{r}{M} \mp 2a}} - 2arL_{\pm}} - 2arL_{\pm}, \quad (7.2.13)$$

$$r [r^3 + a^2(r + 2M)]$$

respectively. The investigation of the above expressions for the angular momentum and energy of the test particle for different values of the radial coordinate allows us to extract physical information about the behavior of the gravitational source. We mention for an analysis of the test particle motion in Kerr spacetime for example [85, 86, 87, 88, 89, 90, 91, 92, 93, 94, 95, 96, 97, 98, 99, 100, 101, 102, 103, 104, 105, 106].

7.3 Black holes

In this section we shall consider the black hole case $0 < a \leq M$. In the non-extreme black hole case ($0 < a < M$), it is $g_{tt} > 0$ for $0 < r < r_-^0$ and $r > r_+^0$. Inside the interval $r_-^0 < r < r_+^0$ the metric component g_{tt} changes its sign. Moreover, g_{tt} vanishes for $r = r_{\pm}^0$ and $0 < \cos^2 \theta \leq 1$, and also at $r = 2M$ for $\theta = \pi/2$. The location of these hypersurfaces is such that $r_-^0 < r_- < r_+ < r_+^0$.

The region $r_-^0 < r < r_+^0$, where $g_{tt} < 0$, is called ergoregion. In this region the Killing vector $\zeta_t^a = (1, 0, 0, 0)$ becomes spacelike or $g_{ab} \zeta_t^a \zeta_t^b = g_{tt} < 0$. This fact implies in particular that a static observer, i.e. an observer with four velocity proportional to ζ_t^a so that $\dot{\theta} = \dot{r} = \dot{\phi} = 0$, cannot exist inside the ergoregion; an observer inside this region is forced to move.

For the extreme black hole case ($a = M$) it holds $r_- = r_+ = M$. Then,

$g_{tt} > 0$ for $0 < r < r_-^0$ and $r > r_+^0$ when $0 \leq \cos^2 \theta < 1$, and for $0 < r < M$ and $r > M$ when $\cos^2 \theta = 1$; moreover, $g_{tt} = 0$ at $r = r_{\pm}^0$ in the interval $0 \leq \cos^2 \theta < 1$, and at $r = M$ for $\cos^2 \theta = 1$. The location of the special radii is such that $r_-^0 < r_- = r_+ < r_+^0$ for $0 \leq \cos^2 \theta < 1$ and $r_-^0 = r_- = r_+ = r_+^0$ for $\cos^2 \theta = 1$.

To investigate the solutions of the conditions of circular motion given by Eq. (7.2.10) it is convenient to introduce the following radii

$$r_a \equiv 4M \cos \left[\frac{1}{6} \arccos \left[-1 + 2 \frac{a^2}{M^2} \right] \right]^2, \quad (7.3.1)$$

$$r_{c2} \equiv 4M \sin \left[\frac{1}{6} \arccos \left[1 - 2 \frac{a^2}{M^2} \right] \right]^2, \quad (7.3.2)$$

$$r_{\gamma} \equiv 2M \left(1 + \sin \left[\frac{1}{3} \arcsin \left[1 - 2 \frac{a^2}{M^2} \right] \right] \right), \quad (7.3.3)$$

which have the two limiting cases

$$r_a = r_{\gamma} = 3M, \quad r_{c2} = 0 \quad \text{for } a = 0, \quad (7.3.4)$$

and

$$r_a = 4M, \quad r_{c2} = r_{\gamma} = M \quad \text{for } a = M, \quad (7.3.5)$$

The dependence of these radii from the specific angular momentum is shown in Fig. 7.1. It is then possible to show that circular orbits can exist only for $r > r_{\gamma}$ and that there are two regions with different values for the angular momentum, namely

$$r_{\gamma} < r \leq r_a, \quad \text{where } L = L_-, \quad (7.3.6)$$

and

$$r > r_a, \quad \text{where } L = -L_+, \quad \text{and } L = L_-. \quad (7.3.7)$$

Moreover, in the extreme black hole case, $a = M$, the circular orbits are situated at

$$r = r_a = 4M, \quad (7.3.8)$$

with two different possible values for the angular momentum

$$L = \frac{13}{4\sqrt{2}}M\mu \quad \text{with } E = \frac{5}{4\sqrt{2}}\mu, \quad \text{and } L = -\frac{13}{4\sqrt{2}}M\mu \quad \text{with } E = \frac{149}{140\sqrt{2}}\mu. \quad (7.3.9)$$

As for the first interval $r_{\gamma} < r \leq r_a$, the behavior of the corresponding energy and angular momentum is illustrated in Fig. 7.2. First we note that the area covered by this region increases as the specific angular momentum of the black hole increases. Whereas r_a and r_{γ} coincide and equal $3M$ for

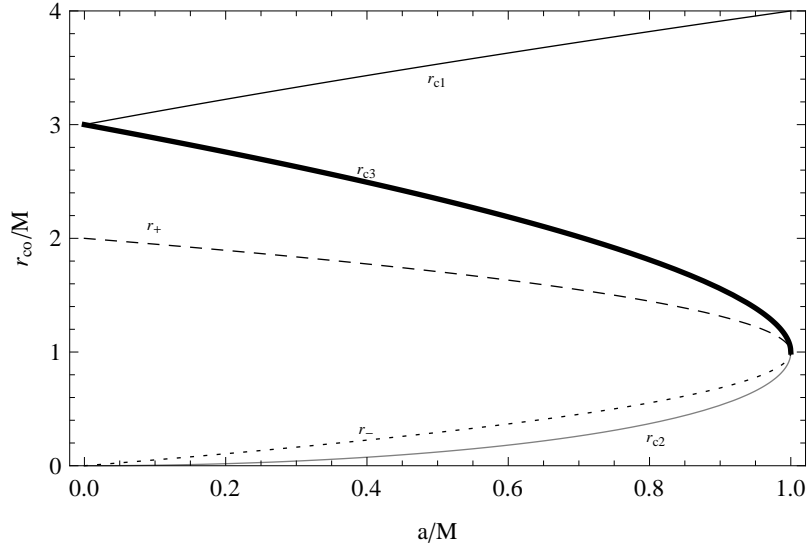


Figure 7.1: The outer horizon r_+ (dashed curve), the inner horizon r_- (dotted curve), and r_a (black curve), r_{c2} (gray curve), and r_γ (thick black curve) are plotted as function of the black hole intrinsic angular momentum a/M . The dotted dashed gray line represents the outer boundary of the ergosphere $r_+^0 = 2M$.

nonrotating black holes ($a = 0$), their maximum separation is reached in the case of extreme black holes ($a = M$) for which r_γ coincides with the outer horizon radius. In the region $r > r_a$, circular orbits are allowed with different values of the angular momentum (the particular case with $L = -L_+$ is illustrated in Fig. 7.3).

We see that in the gravitational field of a black hole with $0 < a < M$, particles with angular momentum $L = L_-$ can exist in the entire region $r > r_\gamma$. As the radius r_γ is approached the angular momentum L_- and the corresponding energy $E_-^{(+)} = E(L_-)$ diverge, indicating that the hypersurface $r = r_\gamma$ is lightlike, i.e., it is the limiting orbit for timelike particles with $L = L_-$. Moreover, particles with angular momentum $L = -L_+$ can move along circular orbits in the interval $r > r_a$, and the limiting lightlike counter-rotating orbit corresponds to $r = r_a$ where both L_+ and the energy $E_+^{(-)} = E(-L_+)$ diverge.

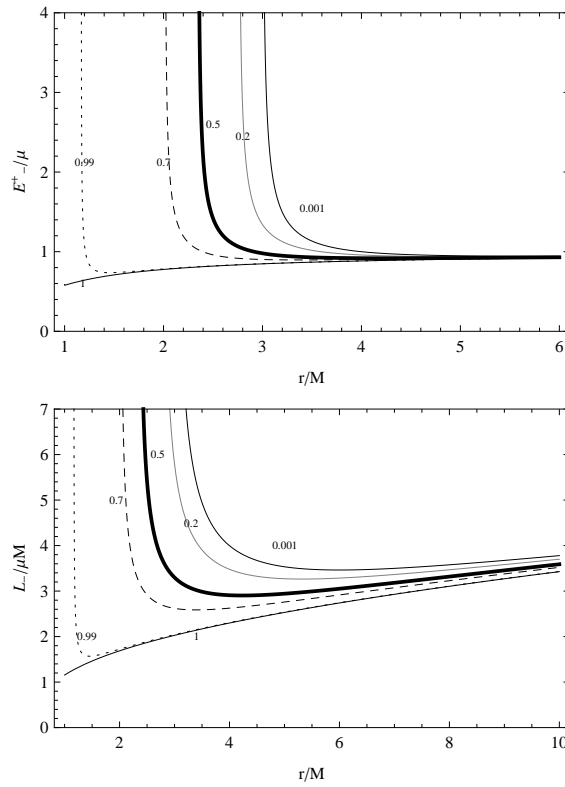


Figure 7.2: The energy $E_-^{(+)} \equiv E(L_-)$ (upper plot) and the angular momentum L_- (bottom plot) of circular orbits in a rotating Kerr black hole with angular momentum $0 < a \leq M$, for selected values of a/M in the interval $r > r_\gamma$. For $a \neq M$ the energy $E_-^{(+)}$ is always positive and diverges as r approaches r_γ . The dotted dashed gray line represents the outer boundary of the ergosphere $r_+^0 = 2M$.

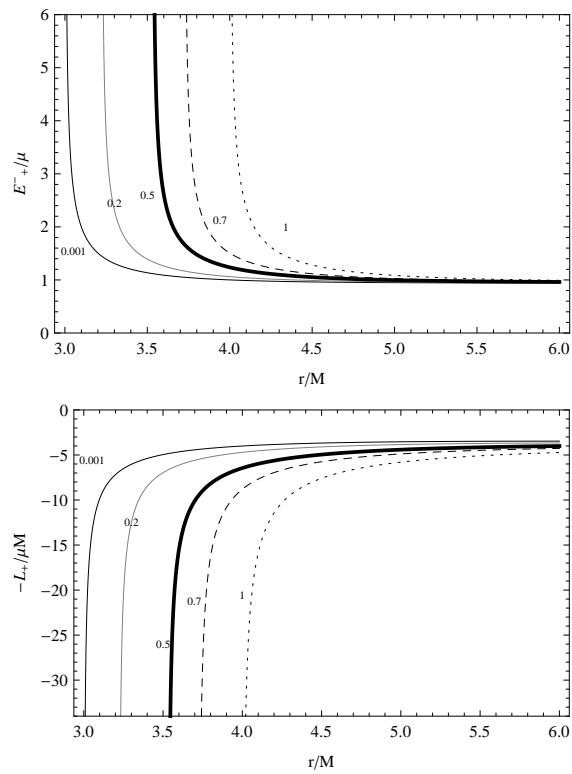


Figure 7.3: The energy $E_+^{(-)} \equiv E(-L_+)$ and angular momentum $L = -L_+$ of circular orbits in a Kerr black hole with angular momentum $0 < a \leq M$, for selected values of a/M in the region $r > r_a$. The energy $E_+^{(-)}$ is always positive and diverges as r approaches r_a .

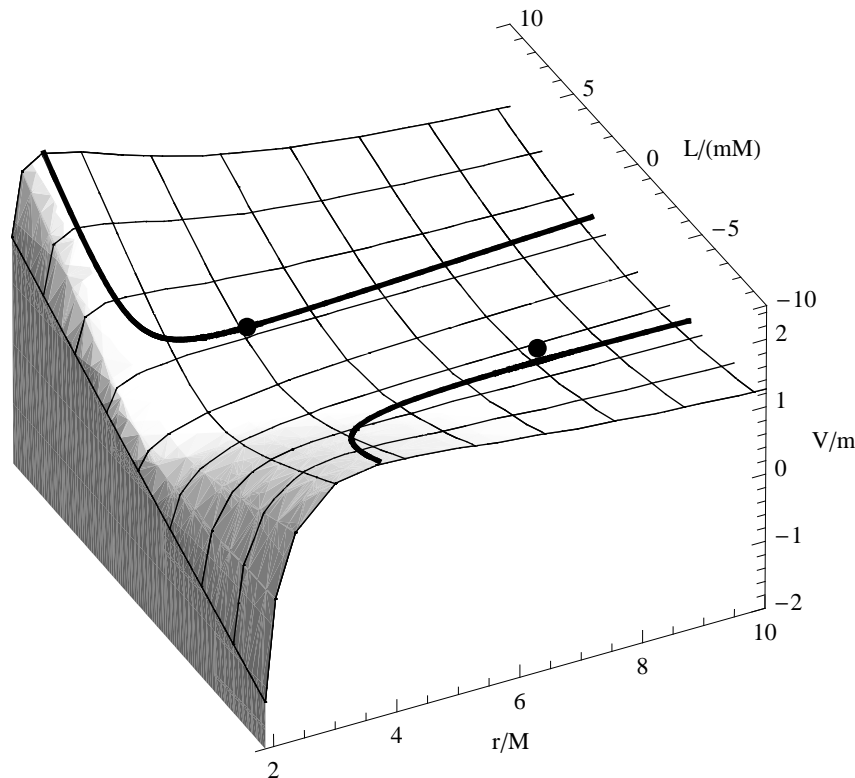


Figure 7.4: The effective potential V/m for a neutral particle of mass μ in a Kerr black hole with $a/M = 0.5$ is plotted as a function of r/M in the range $[1.71, 10]$ for the radial coordinate and in the range $[-10, 10]$ for the angular momentum $L/(\mu M)$. The outer horizon is situated at $r_+ = (1 + 1/\sqrt{2})M$ (see text). Circular orbits exist for $r > 2[1 + \sin(\pi/18)]M \approx 2.347M$. The solid curve represents the location of circular orbits (stable and unstable). Stable (unstable) circular orbits are minima (maxima) of the effective potential function. The last stable circular orbits are represented by a point. The minima are located at $r = 4.233M$ with $L = 2.903/(M\mu)$ and $E = 0.918\mu$, and at $r = 7.554M$ with $L = -3.884/(M\mu)$ and $E = 0.955\mu$.

7.3.1 Stability

From the physical viewpoint it is important to find the minimum radius for stable circular orbits which is determined by the inflection points of the effective potential function, i.e., by the condition

$$\partial^2 V / \partial^2 r = 0. \quad (7.3.10)$$

The behavior of the effective potential (7.2.4) for a fixed value of a/M and different values of the particle angular momentum $L/(M\mu)$ is sketched in Fig. 7.4. The radii of the last stable circular orbits are written as [80, 107]

$$r_{\text{isco}}^{\mp} = M \left[3 + Z_2 \mp \sqrt{(3 - Z_1)(3 + Z_1 + 2Z_2)} \right], \quad (7.3.11)$$

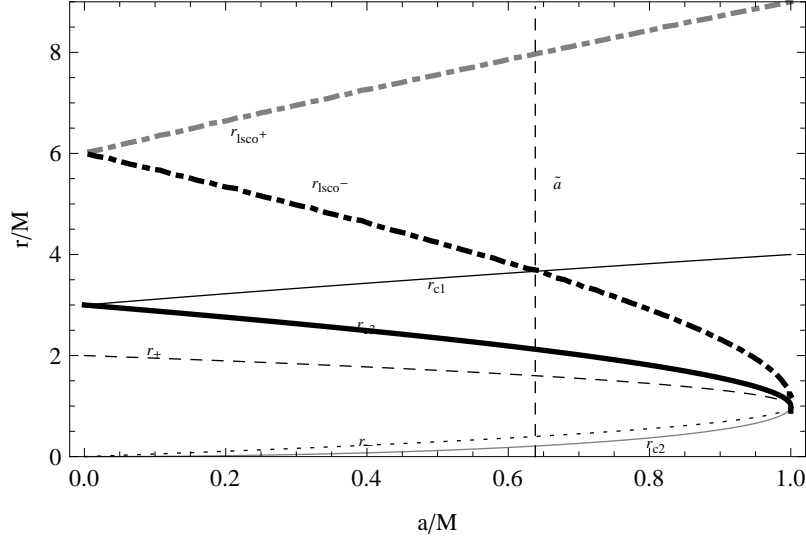


Figure 7.5: The outer horizon r_+ (dashed curve), the inner horizon r_- (dotted curve), and r_a (black curve), r_{c2} (gray curve), r_γ (thick black curve), last stable circular orbits r_{lsc0}^+ (dot-dashed black curve) and r_{lsc0}^- (dotdashed gray curve) are plotted as functions of the black hole intrinsic angular momentum a/M . The curves r_{lsc0}^+ and r_{lsc0}^- represent the radius of the last stable circular orbit for particles with angular momentum $-L_+$ and L_- , respectively. Circular orbits with $L = L_-$ exist for $r/M > r_\gamma$ and with $L = -L_+$ for $r > r_a$. The line $\tilde{a} \approx 0.638285M$ is also plotted. The dotted dashed gray line represents the outer boundary of the ergosphere $r_+^0 = 2M$.

where

$$Z_1 \equiv 1 + \left(1 - \frac{a^2}{M^2}\right)^{1/3} \left[\left(1 + \frac{a}{M}\right)^{1/3} + \left(1 - \frac{a}{M}\right)^{1/3} \right], \quad (7.3.12)$$

and

$$Z_2 \equiv \sqrt{3 \frac{a^2}{M^2} + Z_1^2}. \quad (7.3.13)$$

In particular, for $a = 0$ we have that $r_{lsc0}^+ = 6M$, and when $a = M$ we obtain $r_{lsc0}^- = M$ for co-rotating orbits and $r_{lsc0}^+ = 9M$ for counter-rotating orbits (see also Fig. 7.5). In general, the radii r_{lsc0}^+ and r_{lsc0}^- correspond to the last stable circular orbit of a test particle with angular momentum L_+ and L_- , respectively.

In Fig. 7.6 the energy $E_{lsc0}^\pm/\mu = E(r_{lsc0}^\pm)/\mu$ and the angular momentum $L_{lsc0}^\pm/\mu = L(r_{lsc0}^\pm)/\mu$ of the last stable circular orbits are plotted as functions of the ratio a/M . One can see that

$$E_{lsc0}^+ \leq E_{lsc0}^-, \quad \text{and} \quad E_{lsc0}^+ = E_{lsc0}^- \quad \text{for} \quad a = 0. \quad (7.3.14)$$

Moreover, as the ratio a/M increases, the energy E_{lsc0}^+ decreases and the en-

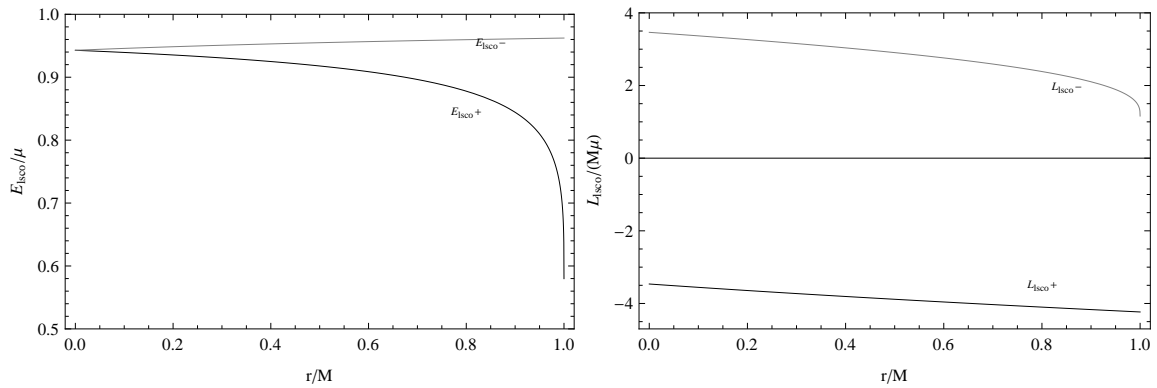


Figure 7.6: The energy E_{lSCO}/μ and the angular momentum $L_{lSCO}^{\pm}/(M\mu)$ of the last stable circular orbit as functions of the ratio $a/M \leq 1$ of a Kerr black hole.

ergy E_{lSCO}^- increases. Instead, the corresponding angular momenta of the test particles decrease as the intrinsic angular momentum increases.

To classify the circular orbits in a Kerr black hole it is convenient to distinguish two different regions: The first one is $a \in [0, \tilde{a}]$, where $\tilde{a} \approx 0.638285M$ is the value at which r_a and r_{lSCO}^- coincide, and the second one is $a \in]\tilde{a}, 1[$.

In the first region $a \in [0, \tilde{a}]$, where $r_a < r_{lSCO}^-$, we see that there exist unstable circular orbits with $L = L_-$ in the interval $r_{\gamma} < r < r_a$. Moreover, in the interval $r_a < r < r_{lSCO}^-$ there are unstable circular orbits with $L = L_-$ and $L = -L_+$. In $r_{lSCO}^- < r < r_{lSCO}^+$ there are stable circular orbits with $L = L_-$ and unstable orbits with $L = -L_+$. Finally, in the region $r > r_{lSCO}^+$ there are stable circular orbits with $L = L_-$ as well as with $L = -L_+$.

Let us consider the second region $a \in]\tilde{a}, 1[$ where $r_a > r_{lSCO}^-$. We see that in the interval $r_{\gamma} < r < r_{lSCO}^-$ there are unstable circular orbits with $L = L_-$. Moreover, in $r_{lSCO}^- < r < r_a$ there are stable orbits with $L = L_-$. In the region $r_a < r < r_{lSCO}^+$ there are stable circular orbits with $L = L_-$ and unstable orbits with $L = -L_+$. Finally, for $r > r_{lSCO}^+$ there are stable circular orbits with $L = L_-$ and $L = -L_+$. The classification of circular orbits in this case is summarized in Table 7.1.

A detailed analysis of the behavior of the energy, angular momentum and effective potential of test particles is presented in Figs. 7.7 and 7.8 for $a/M = 0.5 < \tilde{a}$, in Figs. 7.9 and 7.10 for $a/M = 0.7 > \tilde{a}$, and finally in Figs. 7.11 and 7.12 for the limiting case of an extreme black hole $a/M = 1$.

The case $0 < a < M$		
Region	Angular momentum	Stability
$]r_\gamma, r_a[$	L_-	r_{Isco}^-
$]r_a, \infty[$	$-L_+ (L_-)$	$r_{Isco}^+ (r_{Isco}^-)$
$0 < a < \tilde{a} (r_a < r_{Isco}^-)$		
$]r_\gamma, r_a[$	L_-	Unstable
$]r_a, r_{Isco}^-[$	$(L_-, -L_+)$	Unstable
$]r_{Isco}^-, r_{Isco}^+[$	$L_- (-L_+)$	Stable (Unstable)
$]r_{Isco}^+, \infty[$	$(L_-, -L_+)$	Stable
$\tilde{a} \leq a < M (r_a \leq r_{Isco}^-)$		
$]r_\gamma, r_{Isco}^-[$	L_-	Unstable
$]r_{Isco}^-, r_a[$	L_-	Stable
$]r_a, r_{Isco}^+[$	$L_- (-L_+)$	Stable (Unstable)
$]r_{Isco}^+, \infty[$	$(L_-, -L_+)$	Stable

Table 7.1: Classification of circular orbits of test particles in a Kerr black hole. Here $\tilde{a} \approx 0.638285M$. For each region we present the value of the orbital angular momentum and the stability property.

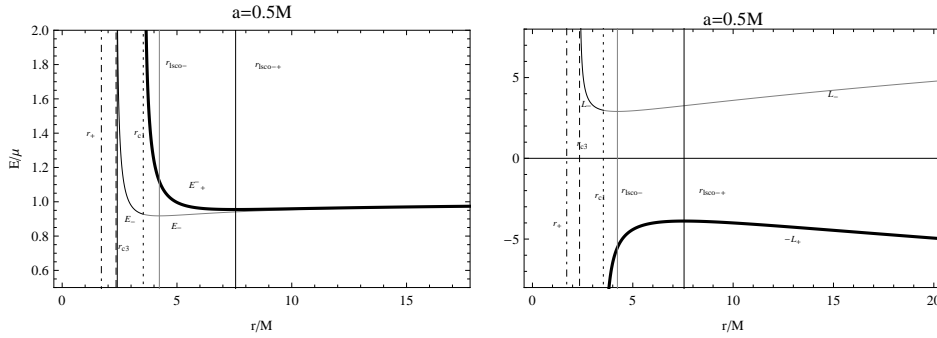


Figure 7.7: The energy E/μ (left plot) and the angular momentum $L/(\mu M)$ (right plot) of circular orbits in a Kerr black hole with $a = 0.5M$ as functions of the radial coordinate r/M . The energy $E_+^{(-)} \equiv E(-L_+)$ and the angular momentum $-L_+$ are represented by thick black curves, and the energy $E_-^{(+)} \equiv E(L_-)$ and the angular momentum L_- by black curves. In $r_\gamma < r < r_a$ there are unstable circular orbits with L_- . For $r_a < r < r_{Isco}^-$ there are unstable circular orbits with L_- and $-L_+$. For $r_{Isco}^- < r < r_{Isco}^+$ there are stable circular orbits with L_- and unstable with $-L_+$, finally for $r > r_{Isco}^+$ there are stable circular orbits with L_- and $-L_+$. The radii $r_+ = 1.70711M$, $r_\gamma = 2.3473M$, $r_a = 3.53209M$ and $r_{Isco}^- = 4.233M$, and $r_{Isco}^+ = 7.55458M$ are also plotted. It is evident that $E(-L_+) > E(L_-)$. The dotted dashed gray line represents the outer boundary of the ergosphere $r_+^0 = 2M$.

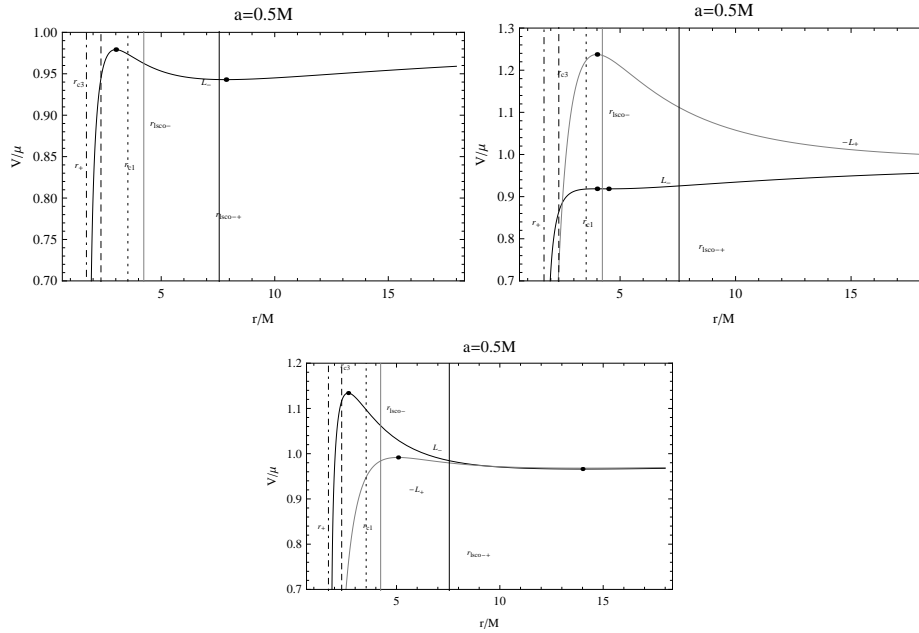


Figure 7.8: The effective potential V/μ of a Kerr black hole with $a = 0.5M$ as a function of r/M . The radii $r_+ = 1.70711M$, $r_\gamma = 2.3473M$, $r_a = 3.53209M$, $r_{ISCO}^- = 4.233M$, and $r_{ISCO}^+ = 7.55458M$ are also plotted. The left upper plot shows the effective potential with orbital angular momentum $L = L_- = 3.29806M\mu$ for which we find a minimum (stable orbit) at $r = 7.85256M$ with energy $E_-/\mu = 0.942949$ and a maximum (unstable orbit) at $r = 3M$ with $E_-/\mu = 0.979181$. The right upper plot corresponds to an effective potential with orbital angular momentum $L = L_- = 2.90877\mu$ (black curve) and $L = -L_+ = -6.45235M\mu$ (gray curve). For $L = L_-$ there is a minimum (stable orbit) at $r = 4.49925M$ with $E_- = 0.918487\mu$ and a maximum (unstable orbit) at $r = 4M$ with $E_- = 0.918559\mu$. For $L = -L_+$ there is a maximum (unstable orbit) at $r = 4M$ with $E_+^{(-)} = 1.23744\mu$. The bottom plot is for an effective potential with orbital angular momentum $L = L_- = 4.09649\mu$ (black curve) and $L = -L_+ = -4.36042M\mu$ (gray curve). For $L = L_-$ there is a minimum (stable orbit) at $r = 14M$ with $E_- = 0.96609\mu$ and a maximum (unstable orbit) at $r = 2.65996M$ with $E_- = 1.134\mu$. For $L = -L_+$ there is a maximum (unstable orbit) at $r = 5.07411M$ with $E_+^{(-)} = 0.991686\mu$ and a minimum (stable orbit) at $r = 14M$ with $E_+^{(-)} = 0.968052\mu$. The dotted dashed gray line represents the outer boundary of the ergosphere $r_+^0 = 2M$.

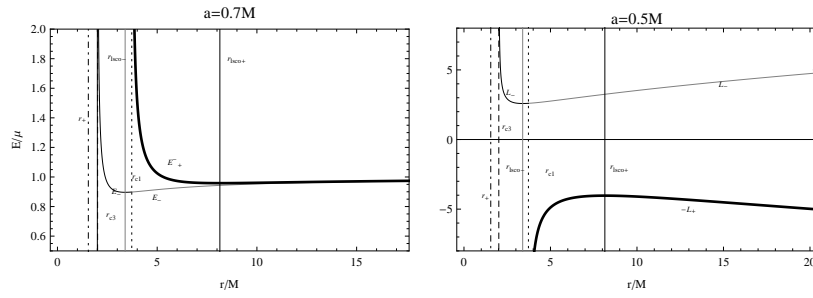


Figure 7.9: The energy E/μ (left plot) and the angular momentum $L/(\mu M)$ (right plot) of circular orbits in a Kerr black hole with $a = 0.7M$ as functions of r/M . The energy $E_+^- \equiv E(-L_+)$ and the angular momentum $-L_+$ are represented by thick black curves, and the energy $E_+^+ \equiv E(L_-)$ and the angular momentum L_- by black curves. The radii $r_+ = 1.54772M$, $r_\gamma = 2.01333M$, $r_a = 3.72535M$, $r_{lsc0}^- = 3.39313M$, and $r_{lsc0}^+ = 8.14297M$ are also plotted. The dotted dashed gray line represents the outer boundary of the ergosphere $r_+^0 = 2M$. In $r_\gamma < r < r_{lsc0}^-$ there are unstable circular orbits with L_- ; in $r_{lsc0}^- < r < r_a$ there are stable orbits with L_- ; in $r_a < r < r_{lsc0}^+$ there are stable circular orbits with L_- and unstable with $-L_+$; finally, for $r > r_{lsc0}^+$ there are stable circular orbits with L_- and $-L_+$. It is clear that $E(-L_+) > E(L_-)$.

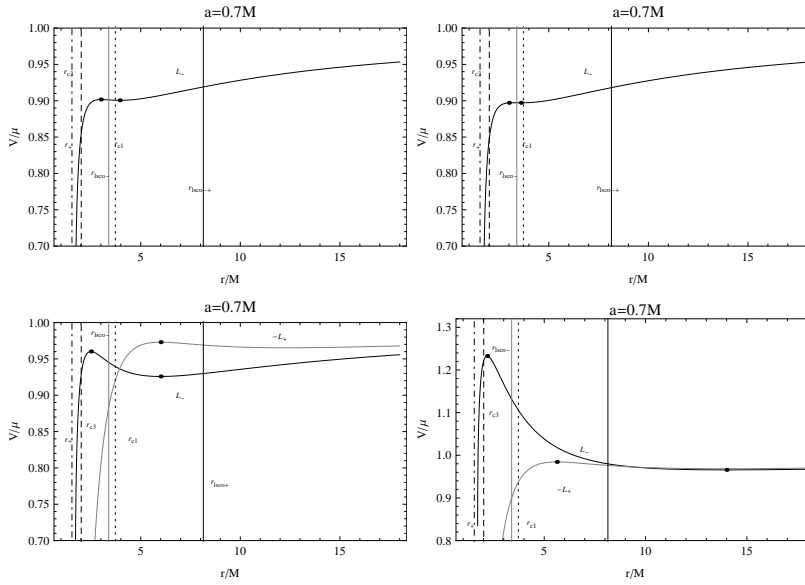


Figure 7.10: The effective potential V/μ of a Kerr black hole spacetime with $a = 0.7M$ as function of r/M . The radii $r_+ = 1.54772M$, $r_\gamma = 2.01333M$, $r_a = 3.72535M$, $r_{ISCO}^- = 3.39313M$, and $r_{ISCO}^+ = 8.14297M$ are plotted. The left upper plot represents the effective potential with orbital angular momentum $L = L_- = 2.61948M\mu$ for which we find a minimum (stable orbit) at $r = 3.9473M$ with $E_- = 0.900551\mu$, and a maximum (unstable orbit) at $r = 3M$ with $E_- = 0.901712\mu$. The right upper plot shows an effective potential with orbital angular momentum $L = L_- = 2.59216M\mu$ for which there exists a minimum (stable orbit) at $r = 3.6M$ with $E_- = 0.897167\mu$, and a maximum (unstable orbit) at $r = 3M$ with $E_- = 0.897167\mu$. The left bottom plot corresponds to effective potentials with orbital angular momenta $L = L_- = 2.91563\mu$ (black curve) and $L = -L_+ = -4.2694M\mu$ (gray curve). For $L = L_-$ there is a minimum (stable orbit) at $r = 6M$ with $E_- = 0.925818\mu$, and a maximum (unstable orbit) at $r = 2.50052M$ with $E_- = 0.960213\mu$. For $L = -L_+$ there is a maximum (unstable orbit) at $r = 6M$ with $E_+^{(-)} = 0.973034\mu$. The right bottom plot is for effective potentials with orbital angular momenta $L = L_- = 4.05058\mu$ (black curve) and $L = -L_+ = -4.42036M\mu$ (gray curve). For $L = L_-$ there is a minimum (stable orbit) at $r = 14M$ with $E_- = 0.965775\mu$, and a maximum (unstable orbit) at $r = 2.1819M$ with $E_- = 1.23283\mu$. For $L = -L_+$ there is a maximum (unstable orbit) at $r = 5.6208M$ with $E_+^{(-)} = 0.98443\mu$, and a minimum (stable orbit) at $r = 14M$ with $E_+^{(-)} = 0.968527\mu$. The dotted dashed gray line represents the outer boundary of the ergosphere $r_+^0 = 2M$.

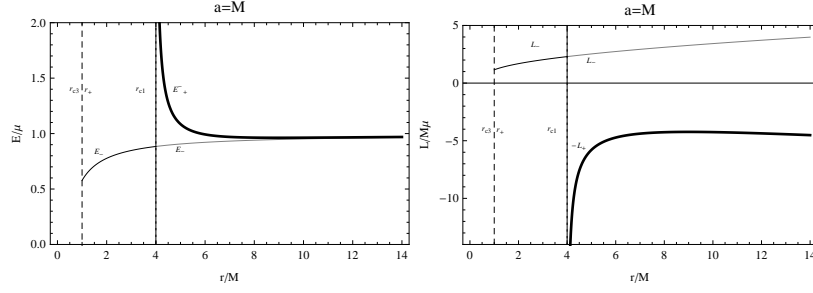


Figure 7.11: The energy E/μ (left plot) and the angular momentum $L/(\mu M)$ (right plot) of circular orbits in an extreme Kerr black hole ($a = M$) as functions of the radial coordinate r/M . The energy $E(-L_+)$ and the angular momentum $-L_+$ are represented by thick black curves, and the energy $E(L_-)$ and the angular momentum L_- by black curves. The radii $r_+ = r_\gamma = M$ (dashed curve) and $r_a = 4M$ (black curve) are also plotted. There exist circular orbits with $L = L_-$ in $r > r_\gamma$. The energy $E(L_-)$ is always positive and decreases as r approaches r_γ . Circular orbits with $L = -L_+$ exist also in $r > r_+$. The energy $E(-L_+)$ is always positive and increases as r approaches r_a . It is evident that $E(-L_+) > E(L_-)$.

To present the main result of our analysis in a plausible manner it is convenient to introduce the idea of a hypothetical accretion disk formed by test particles on circular orbits around the central massive object. We consider this model only in the region $r > r_+^0$. The structure of such an accretion disk depends explicitly on the stability properties of the test particles. In fact, as mentioned above the radii r_{lsc0}^- and r_{lsc0}^+ represent the last stable orbits for particles with angular momentum $L = L_-$ (corotating particles) and $L = -L_+$ (counter-rotating particles), respectively. Then, in the disk contained within the radii $[r_{lsc0}^-, r_{lsc0}^+]$ only the corotating particles can move along stable trajectories. If a counter-rotating particle is located inside this disk (this is possible if the radius of the orbit is $r > r_a$), its orbit is unstable and it must decay into an orbit with radius $r > r_{lsc0}^+$. Consequently, the outer disk with $r > r_{lsc0}^+$ can be build of corotating and counter-rotating particles which are both stable in this region. The size of the inner disk $[r_{lsc0}^-, r_{lsc0}^+]$ depends on the value of the intrinsic angular momentum of the black hole a ; the maximum size is reached in the case of an extreme black hole ($a = M$) with $r_{lsc0}^+ - r_{lsc0}^- = 8M$ whereas for $a = 0$ the radii coincide $r_{lsc0}^+ = r_{lsc0}^-$ and the disk disappears (cf. Fig. 7.5).

7.4 Naked singularities

In the naked singularity case ($a > M$), it is $g_{tt} > 0$ for $0 < r < r_-^0$ and $r > r_+^0$ when $0 \leq \cos^2 \theta < 1/a^2$, for $r > 0$ with $r \neq r_-^0$ when $\cos^2 \theta = 1/a^2$, and finally for $r > 0$ when $1/a^2 < \cos^2 \theta \leq 1$. Moreover, $g_{tt} = 0$ at $r = 2M$ if $\theta = \pi/2$, at $r = r_\pm^0$ for $0 < \cos^2 \theta < 1/a^2$, and at $r = r_-^0$ for $\cos^2 \theta = 1/a^2$. As in the black hole case, in the region (r_-^0, r_+^0) the Killing vector $\xi_t^a = (1, 0, 0, 0)$ becomes spacelike. On the equatorial plane, $\theta = \pi/2$, it is $r_+^0 = 2M$ and

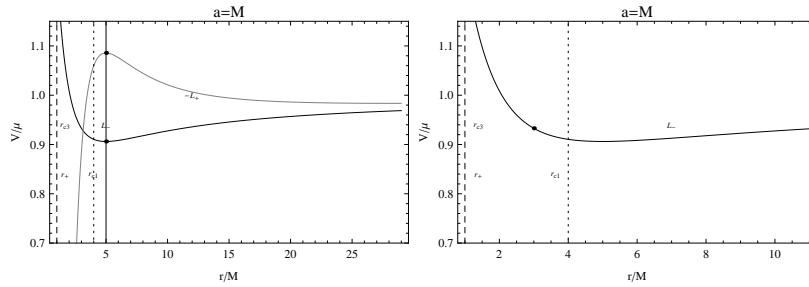


Figure 7.12: The effective potential V/μ of an extreme Kerr black hole for a test particle with a fixed orbital angular momentum as function of r/M . The radii $r_+ = r_\gamma = M$ (dashed curve) and $r_a = 4M$ (black curve) are plotted. The dotted dashed gray line represents the outer boundary of the ergosphere $r_+^0 = 2M$. The left plot shows the effective potentials with orbital angular momenta $L = L_-$ (black curve) and $L = -L_+$ (gray curve). For $L = L_-$ there is a minimum (stable orbit) at $r = 5M$ with $L_- = 2.53075M\mu$ and $E_- = 0.906154\mu$. For $L = -L_+$ there is a maximum (unstable orbit) at $r = 5M$ with $-L_+ = -5.79614M\mu$ and $E_+^- = 1.08576\mu$. There exist circular orbits with $L = L_-$ in the region $r > r_\gamma$, and orbits with $L = -L_+$ in the region $r > r_+$. The dotted dashed gray line represents the outer boundary of the ergosphere $r_+^0 = 2M$.

$r_-^0 = 0$. In this case, the timelike Killing vector becomes spacelike in the region $0 < r < r_+^0$, for all $a > M$.

According to the results presented in Sec. 7.2, to explore the motion of test particles along circular orbits we must solve the following equations

$$\dot{r} = 0, \quad V = E/\mu, \quad \partial V/\partial r = 0 \quad (7.4.1)$$

for the effective potential (7.2.4) with $a > M$, taking into account that in this case no horizons exist. It turns out that it is convenient to study separately the range $a \geq 3\sqrt{3}/4M$ (see Sec. 7.4.1) and the range $M < a < 3\sqrt{3}/4M$ (see Sec. 7.4.2) for the values of the intrinsic angular momentum of the naked singularity.

7.4.1 The case $a \geq (3\sqrt{3}/4)M$

In this case we find that for all $r > 0$ there exist circular orbits with angular momentum $L = L_-$ and energy $E_-^{(+)} = E(L_-)$. In Fig. 7.13 we illustrate the behavior of the energy and angular momentum of test particles for this case.

An analysis of the effective potential shows that a second class of circular orbits with $L = -L_+$ and energy $E_+^{(-)} = E(-L_+)$ can be found in the region

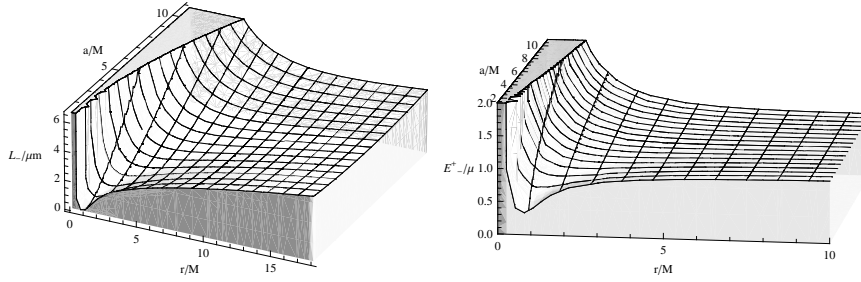


Figure 7.13: Angular momentum and energy of test particles in a Kerr naked singularity with $a \geq (3\sqrt{3}/4)M$. The angular momentum $L = L_-$ (left plot) and the energy $E_-^{(+)} \equiv E(L_-)$ (right plot) of circular orbits are plotted as functions of $r > 0$ and $a \geq (3\sqrt{3}/4)M$. The particle's energy is always positive. It is possible to note a region of minima for the energy corresponding to the minima of L_- .

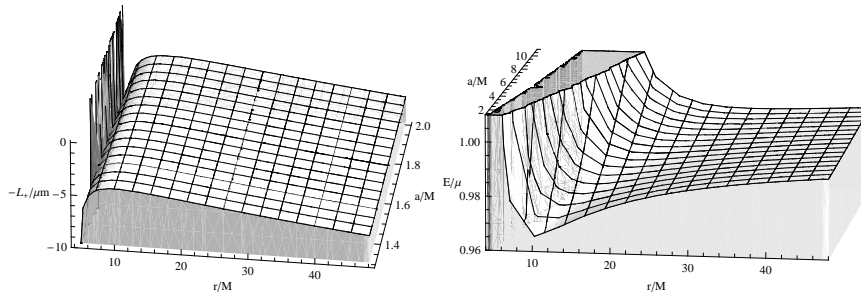


Figure 7.14: Angular momentum and energy of test particles in a Kerr naked singularity with $a \geq (3\sqrt{3}/4)M$. The angular momentum $L = -L_+$ (left plot) and the energy $E_+^{(-)} \equiv E(-L_+)$ (right plot) of circular orbits are plotted as functions of $r > r_a$ and $a \geq (3\sqrt{3}/4)M$. The particle's energy is always positive. It is possible to note a region of minima for the energy corresponding to the minima of $-L_+$.

$r > r_a$ where

$$\frac{r_a}{M} \equiv 2 + \frac{1 + \left(2\frac{a^2}{M^2} - 1 + 2\sqrt{\frac{a^4}{M^4} - \frac{a^2}{M^2}}\right)^{2/3}}{\left(2\frac{a^2}{M^2} - 1 + 2\sqrt{\frac{a^4}{M^4} - \frac{a^2}{M^2}}\right)^{1/3}}. \quad (7.4.2)$$

The expression for the energy and angular momentum of the test particles in this region is depicted in Fig. 7.14.

The special radius r_a and the angular momentum for this radius $L(r_a)/(\mu M)$ increase as the intrinsic angular momentum of the naked singularity increases, as shown in Fig. 7.15. Notice that we are using the same notation r_a for the radius (7.3.1) of a black hole and the radius (7.4.2) of a naked singularity. Although these radii are different in their definitions, we use the same notation because in the limiting case $a = M$ they both have the same limiting value

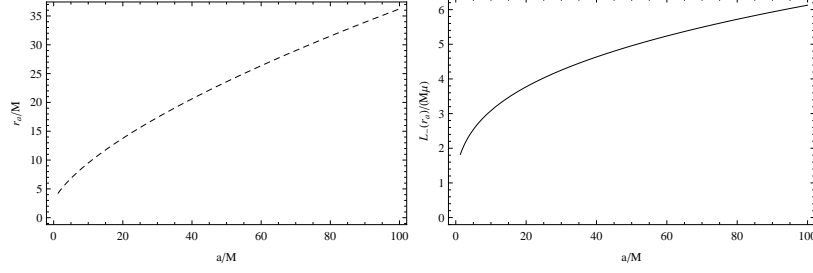


Figure 7.15: The graphic shows the radius r_a/M (left plot) as a function of the intrinsic angular momentum parameter a/M in the interval $(3\sqrt{3}/4, 100)$, and the particle orbital angular momentum $L(r_a)/(\mu M)$ (right plot) as a function of a/M . The dotted dashed gray line represents the outer boundary of the ergosphere $r_+^0 = 2M$.

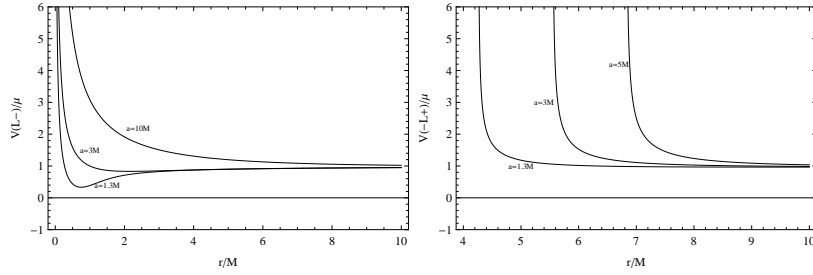


Figure 7.16: The energy of circular orbits in a Kerr naked singularity with source angular momentum $a \geq (3\sqrt{3}/4)M$ is plotted in terms of the radial coordinate r/M for selected values of a/M . The left plot corresponds to particles with $L = L_-$, and the right plot is particles with $L = -L_+$. The energy is always positive and diverges as the limiting radius is approached. The dotted dashed gray line represents the outer boundary of the ergosphere $r_+^0 = 2M$.

$r_a = 4M$. This will turn out later on to be convenient when we compare the results of black holes with those of naked singularities.

The energies $E(L_-)$ and $E(-L_+)$ for the two classes of test particles allowed in this are compared in Fig. 7.16. For particles with angular momentum $L = L_-$ we see that the energy diverges as the limiting value $r \rightarrow 0$ is approached. Similarly, for particles with $L = -L_+$ the energy diverges as the radius approaches the limiting value $r \rightarrow r_a$, indicating that the orbit located at $r = r_a$ is lightlike.

We now study the stability of the test particles in this specific case. An analysis of the turning points of the potential (7.2.4) indicates that the radius of the last stable circular orbit for particles with $L = L_-$ (located in the region $r > 0$) is given by

$$\bar{r}_{lsc0} \equiv M \left(3 - Z_2 + \sqrt{(3 - Z_1)(3 + Z_1 - 2Z_2)} \right), \quad (7.4.3)$$

where Z_1 and Z_2 were defined in Eq. (7.3.12) and Eq. (7.3.13), respectively.

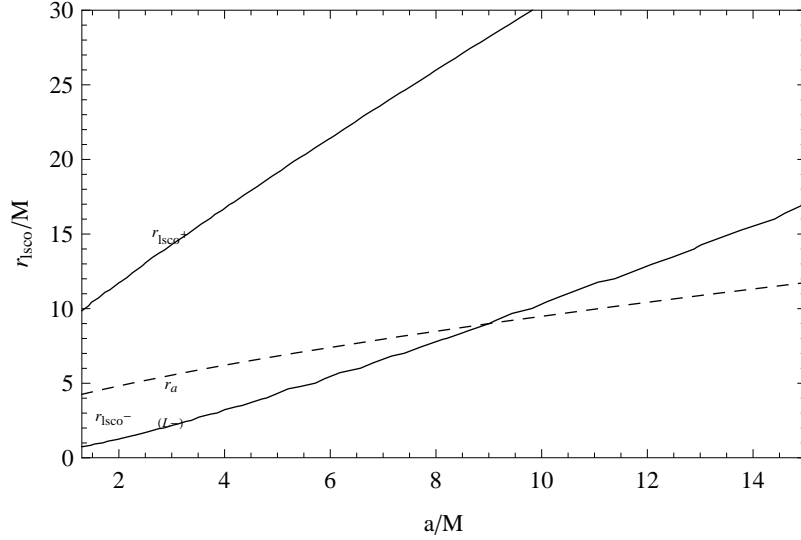


Figure 7.17: Radius of the last stable circular orbits for test particles in a Kerr naked singularity with $a \geq \frac{3\sqrt{3}}{4}M$. The dotted dashed gray line represents the outer boundary of the ergosphere $r_+^0 = 2M$. The radius \bar{r}_{lSCO} (r_{lSCO}^+) is the limiting minimum radius of stability for particles with $L = L_-$ ($L = -L_+$).

Moreover, for particles with $L = -L_+$ located at $r > r_a$ there exists a minimum radius $r = r_{lSCO}^+$ for the last stable circular orbit. The expression for r_{lSCO}^+ is given in Eq. (7.3.11). The behavior of this limiting radii in terms of the intrinsic angular momentum of the naked singularity is depicted in Fig. 7.17. It follows that both radii increase as the value of a/M increases.

It turns out that it is necessary to distinguish two different regions, namely $a/M \in [3\sqrt{3}/4, 9]$ and $a/M \in]9, +\infty[$.

The region $a/M \in [3\sqrt{3}/4, 9]$

In the first region $a/M \in [3\sqrt{3}/4, 9]$ which is characterized by

$$\bar{r}_{lSCO} < r_a < r_{lSCO}^+, \quad \text{and} \quad \bar{r}_{lSCO} = r_a \quad \text{for} \quad a \approx 9M, \quad (7.4.4)$$

there exist unstable circular orbits with $L = L_-$ in the interval $0 < r < \bar{r}_{lSCO}$, and stable orbits with $L = L_-$ in the interval $\bar{r}_{lSCO} < r < r_a$. Moreover, in the region $r_a < r < r_{lSCO}^+$ there are stable orbits with angular momentum $L = L_-$, and unstable orbits with angular momentum $L = -L_+$. Finally, for $r > r_{lSCO}^+$ there are stable orbits with $L = L_-$ and $L = -L_+$. In Fig. 7.18 we present a summary of this case.

As a concrete example for this case we consider now the motion of test particles around a naked singularity with $a = \frac{3\sqrt{3}}{4}M$. In this case, circular orbits with orbital angular momentum $L = L_-$ exist in the range $r > 0$, and

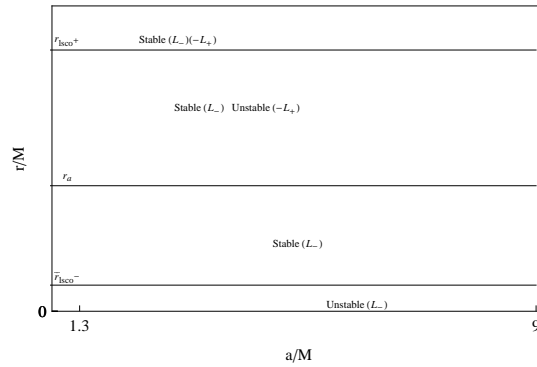


Figure 7.18: Orbits stability in a Kerr naked singularity with $\frac{3\sqrt{3}}{4}M \leq a \lesssim 9$. The different radii of the last stable circular orbits r_{lsc0} are plotted in terms of the intrinsic angular momentum a/M .

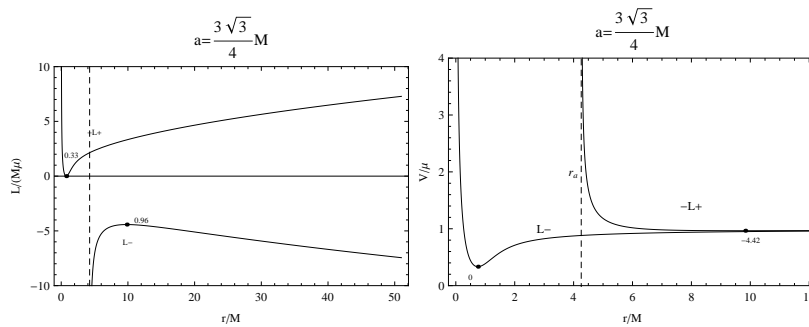


Figure 7.19: The angular momentum and the energy of test particles in the field of a Kerr naked singularity with $a = 3\sqrt{3}/4M \approx 1.30M$ are plotted as functions of the radial coordinate r/M . The dots represent the last stable circular orbits; numbers close to the points denote the energy V/μ of the last stable circular orbit. For $r > r_a \approx 4.2592M$ there exist circular orbits with angular momentum $L = -L_+$, and for all $r > 0$ with $L = L_-$ (see text). For $r = 0.75M$ the particle has $L = 0$ and energy $E \approx 0.333M$. The dotted dashed gray line represents the outer boundary of the ergosphere $r_+^0 = 2M$.

with $L = -L_+$ in the range $r > r_a \approx 4.259M$. The energy and angular momentum of these circular orbits are plotted in Figs. 7.19.

In Fig. 7.20 the effective potential is plotted for different values of the orbital angular momentum. In particular, an “orbit” with zero angular momentum ($L = 0$) and energy $E \approx 0.333M$ exists for $r = 0.75M$ (see also Sec. 7.4.3).

From the analysis of the effective potential it follows that the turning points are located at $r_{lsc0}^+ \approx 9.828M$ where $L_{lsc0}^+ \approx -4.421\mu M$ and $V_{lsc0}^+ \approx 0.96\mu$. Moreover, in the interval $0 < r < r_{lsc0}^-$ the orbits with angular momentum $L = L_-$ are unstable; in the interval $r_{lsc0}^- < r < r_a$ the orbits with $L = L_-$ are stable; and for $r_a < r < r_{lsc0}^+$ we see that the orbits with $L = L_-$ are stable and those with $L = -L_+$ are unstable. Finally, in the range $r > r_{lsc0}^+$, the orbits with $L = -L_+$ and $L = L_-$ are both stable.

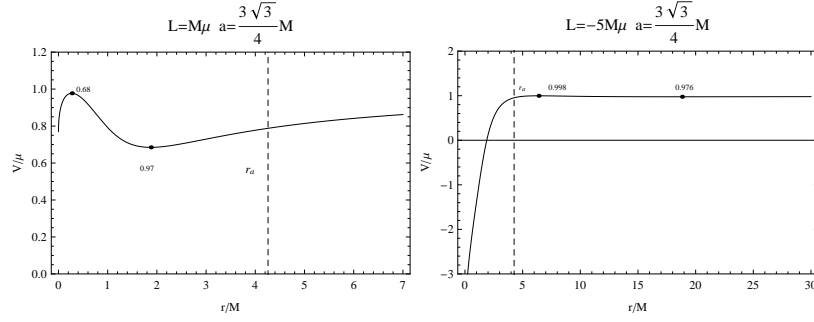


Figure 7.20: The effective potential of a naked singularity with $a = \frac{3\sqrt{3}}{4}M$ for fixed values of the particle angular momentum $L/(M\mu)$. The dotted dashed gray line represents the outer boundary of the ergosphere $r_+^0 = 2M$. The radius r_a is also plotted (see text). The dots denote the critical points of the potential. Numbers close to the dots denote the energy V/μ of the maxima and minima of the effective potential.

The region $\frac{a}{M} \in]9, +\infty[$

In the second region ($a \gtrsim 9M$) which is characterized by

$$r_a < \bar{r}_{lsc0} < r_{lsc0}^+, \quad (7.4.5)$$

there are unstable orbits with angular momentum $L = L_-$ in the interval $0 < r < r_a$ and with $L = L_-$ and $L = -L_+$ in the interval $r_a < r < \bar{r}_{lsc0}$. Moreover, for $\bar{r}_{lsc0} < r < r_{lsc0}^+$ there are stable orbits with $L = L_-$ and unstable ones with $L = -L_+$. Finally, for $r > r_{lsc0}^+$ there are stable orbits with both $L = L_-$ and $L = -L_+$. In Fig. 7.21 a schematic summary of this case is presented.

As a concrete example of this case we now analyze the circular motion of test particles around a naked singularity with $a = 2M$. In this case, circular orbits with angular momentum $L = L_-$ exist in the entire range $r > 0$, and with $L = -L_+$ in the range $r > r_a \approx 4.822M$. The energy and the angular momentum of the circular orbits are plotted in Figs. 7.22.

In Fig. 7.23, the effective potential of circular orbits is plotted for selected values of the orbital angular momentum in terms of the radial distance. The turning points of the effective potential are $r_{lsc0}^+ \approx 11.702M$ for which $L_{lsc0}^+ \approx -4.814\mu M$ and $V_{lsc0}^+ \approx 0.971\mu$, and $r_{lsc0}^- \approx 1.263M$ with $L_{lsc0}^- \approx 0.645\mu M$ and $V_{lsc0}^- \approx 0.687\mu$.

The distribution of circular orbits is as follows: In the interval $0 < r < \bar{r}_{lsc0}$ there exist unstable orbits with $L = L_-$ which become stable for $\bar{r}_{lsc0} < r < r_a$; in the interval $r_a < r < r_{lsc0}^+$ the orbits with $L = L_-$ are stable while those with $L = -L_+$ are unstable. In the outer region $r > r_{lsc0}^+$ orbits with $L = -L_+$ and $L = L_-$ are both stable. To illustrate the results of the analysis of this case, we consider in the region $r > r_+^0$ the model of an accretion disk made of stable particles moving on circular orbits around the central naked

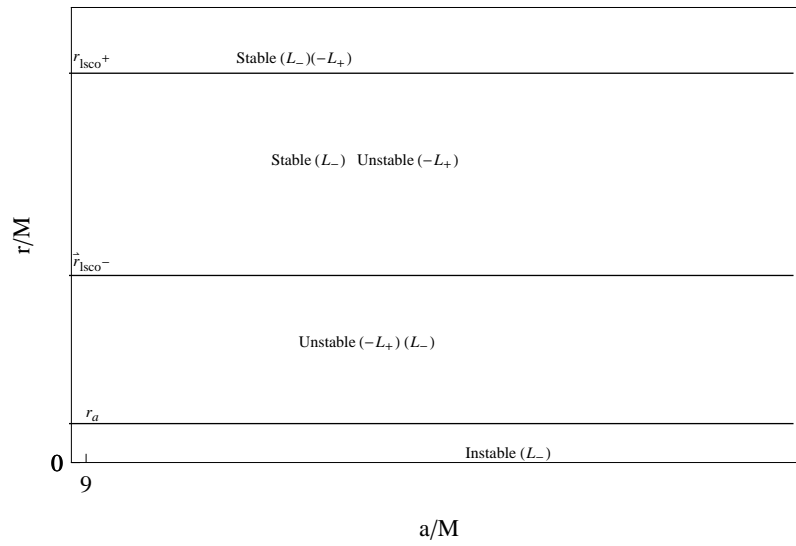


Figure 7.21: Orbits stability in a Kerr naked singularity with $a \gtrsim 9M$. The radii r_{lSCO} of the last stable circular orbits are plotted as functions of the intrinsic angular momentum a/M . The radius $r = r_a$ is also plotted.

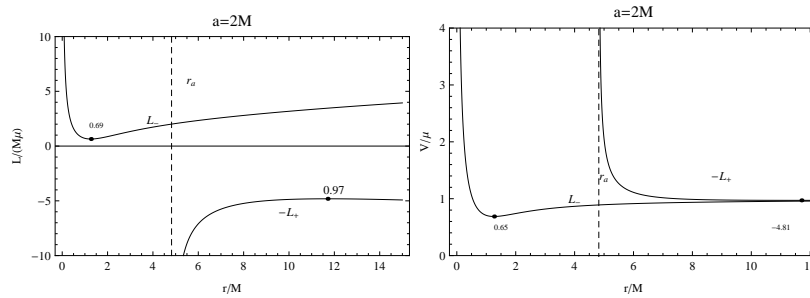


Figure 7.22: The angular momentum and the energy of circular orbits in a Kerr naked singularity with $a = 2M$, as functions of the radial distance r/M . The dotted dashed gray line represents the outer boundary of the ergosphere $r_+^0 = 2M$. The dots denote the position of the last stable circular orbits, and the numbers close to the dots indicate the value of the corresponding energy V/μ or angular momentum $L/(M\mu)$. In the range $r > r_a \approx 4.822M$ there exist circular orbits with $L = -L_+$, and in $r > 0$ with $L = L_-$ (see text).

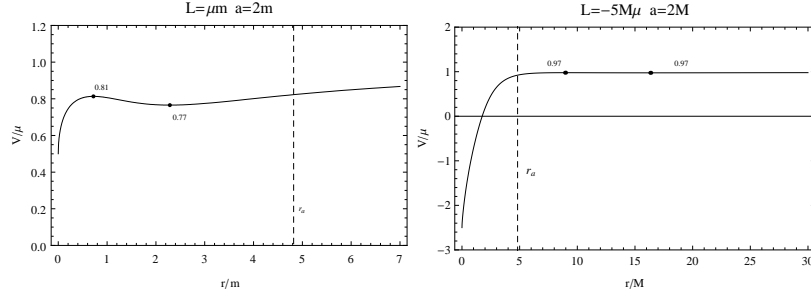


Figure 7.23: The effective potential of a naked singularity with $a = 2M$ for fixed values of the particle angular momentum $L/(M\mu)$. The radius r_a is also plotted (see text). The dotted dashed gray line represents the outer boundary of the ergosphere $r_+^0 = 2M$. The dots represent the critical points of the potential. Numbers close to the dots indicate the energy V/μ of the maxima and minima of the effective potential.

singularity. We find an accretion disk composed of an interior disk contained within the radii $[\bar{r}_{lsc0}, r_{lsc0}^+]$ in which stable particles with angular momentum $L = L_-$ co-rotate with the central singularity. A second disk is located at $r > r_{lsc0}^+$ and contains co-rotating particles with angular momentum $L = L_-$ and counter-rotating particles with $L = -L_+$. We see that the structure of this accretion disk is similar to that found in Sec. 7.3 for black holes. The only difference is that in the case of a naked singularity the interior disk situated within the radii $[\bar{r}_{lsc0}, r_{lsc0}^+]$ has a minimum size of $r_{lsc0}^+ - \bar{r}_{lsc0} > 8M$, whereas in the case of a black hole the size of the inner disk is always less than $8M$ and disappears as $a \rightarrow 0$.

7.4.2 The case $M < a < (3\sqrt{3}/4)M$

For this range of values of the intrinsic angular momentum of the naked singularity we find that there are circular orbits with angular momentum $L = -L_+$ and energy $E(-L_+)$ only in the region $r > r_a$. In Fig. 7.24 we present the parameters for the circular orbits.

From the expression for the effective potential and the conditions for circular motion it follows that in this case two additional regions arise. Indeed, in the intervals $0 < r < \hat{r}_-$ and $r \geq \hat{r}_+$ there exist circular orbits with angular momentum $L = L_-$ and energy $E(L_-)$ (see Fig. 7.25). Moreover, in the interval $\hat{r}_- < r < \hat{r}_+$ we observe circular orbits with angular momentum $L = -L_-$ and energy $E(-L_-)$ (see Fig. 7.26), where

$$\hat{r}_{\pm} \equiv \frac{1}{\sqrt{6}} \left[\Sigma \pm \sqrt{\frac{6\sqrt{6}a^2M}{\Sigma} - \Sigma^2 - 6a^2} \right], \quad (7.4.6)$$

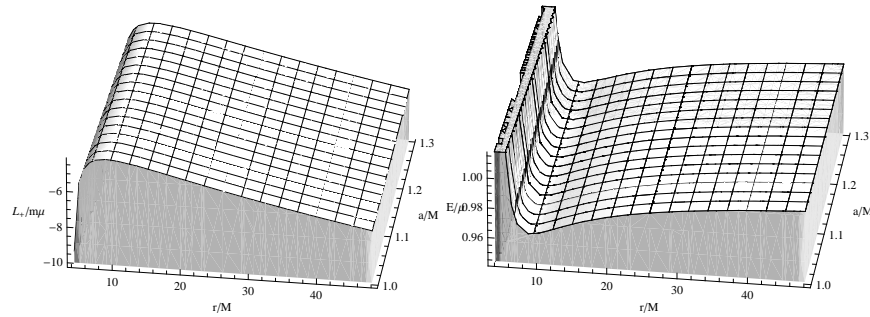


Figure 7.24: Circular motion around a naked singularity with $M < a < (3\sqrt{3}/4)M$. The angular momentum $L = -L_+$ (left plot) and the energy $E_+^{(-)} \equiv E(-L_+)$ (right plot) for circular orbits are plotted as functions of a in the range $1 < a/M < 3\sqrt{3}/4$ and r in the range $r > r_a$. The particle energy is always positive with a region of minima corresponding to the minima of $-L_+$.

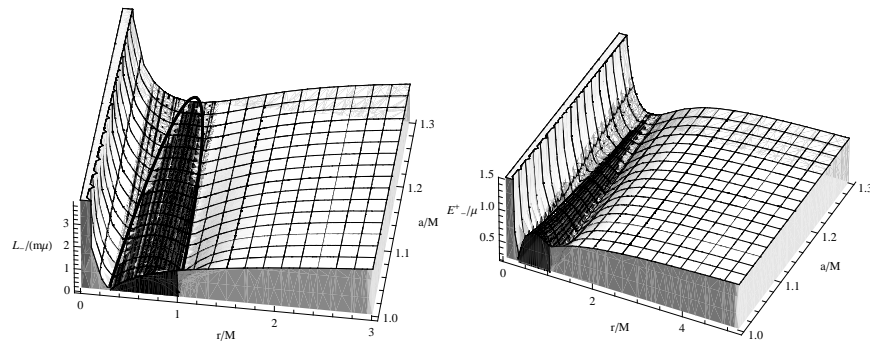


Figure 7.25: Circular motion around a naked singularity with $M < a < (3\sqrt{3}/4)M$. The angular momentum $L = L_-$ (left plot) and the energy $E_- \equiv E(L_-)$ (right plot) of circular orbits are plotted as functions of a in the range $1 < a/M < 3\sqrt{3}/4$ and r in the intervals $r > \hat{r}_+$ and $0 < r < \hat{r}_-$. The region $\hat{r}_- < r < \hat{r}_+$ is represented as a dark region. As r/M approaches the singularity, the particle energy and angular momentum diverge. As r/M approaches \hat{r}_- from the left and \hat{r}_+ from the right, the particle energy and angular momentum decrease.

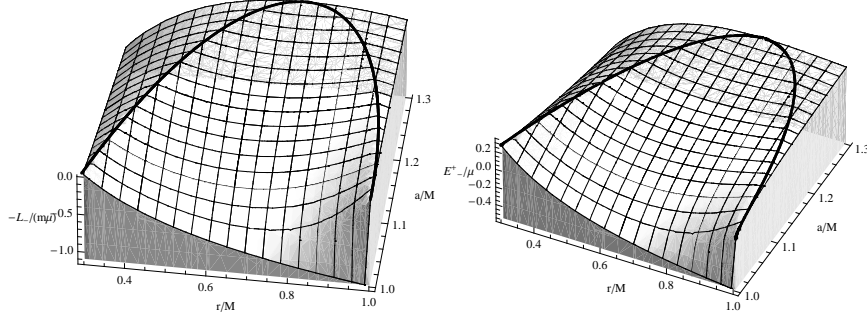


Figure 7.26: Circular motion around a naked singularity with $M < a < (3\sqrt{3}/4)M$. The angular momentum $L = -L_-$ (left plot) and the energy $E_- \equiv E(-L_-)$ (right plot) of circular orbits are plotted as functions of a in the range $1 < a/M < 3\sqrt{3}/4$ and of r in the interval $\hat{r}_- < r < \hat{r}_+$. The black curves represent the radii \hat{r}_- and \hat{r}_+ . The presence of negative values for the particle energy is evident.

with

$$\Sigma = \sqrt{\frac{4a^4}{\sigma^{1/3}} + \sigma^{1/3} - 2a^2}, \quad (7.4.7)$$

and

$$\sigma = \left(27M^2a^4 - 8a^6 + 3M\sqrt{81M^2a^8 - 48a^{10}} \right). \quad (7.4.8)$$

The behavior of these special radii is illustrated in Fig. 7.27.

Notice that the energy of circular orbits $E(-L_+)$ in the interval $0 < r < \hat{r}_-$ and in $r \geq \hat{r}_+$ (see Fig. 7.28), and the energy $E(L_-)$ in the interval $r > r_a$ are always positive (see Fig. 7.29). On the contrary, the energy $E(-L_-)$ of circular orbits within the region $\hat{r}_- < r < \hat{r}_+$ can be negative. In particular, we see that $E(-L_-) = 0$ for $a = \bar{a}$, where

$$\bar{a} \equiv -(r - 2M)\sqrt{\frac{r}{M}}, \quad (7.4.9)$$

or for the orbital radii $r = \bar{r}_1$ and $r = \bar{r}_2$, where

$$\frac{\bar{r}_1}{M} \equiv \frac{8}{3} \sin \left(\frac{1}{6} \arccos \left[1 - \frac{27a^2}{16M^2} \right] \right)^2, \quad (7.4.10)$$

and

$$\frac{\bar{r}_2}{M} \equiv \frac{4}{3} \left(1 + \sin \left[\frac{1}{3} \arcsin \left[1 - \frac{27a^2}{16M^2} \right] \right] \right), \quad (7.4.11)$$

which are the solutions of the equation $a = \bar{a}$.

We can see that $E(-L_-) < 0$ for $M < a < \sqrt{32/27}M$ in the interval $\bar{r}_1 < r < \bar{r}_2$. Otherwise, for $a > \sqrt{32/27}M$, the energy $E(-L_-)$ is always strictly positive. This behavior is illustrated in Fig. 7.30.

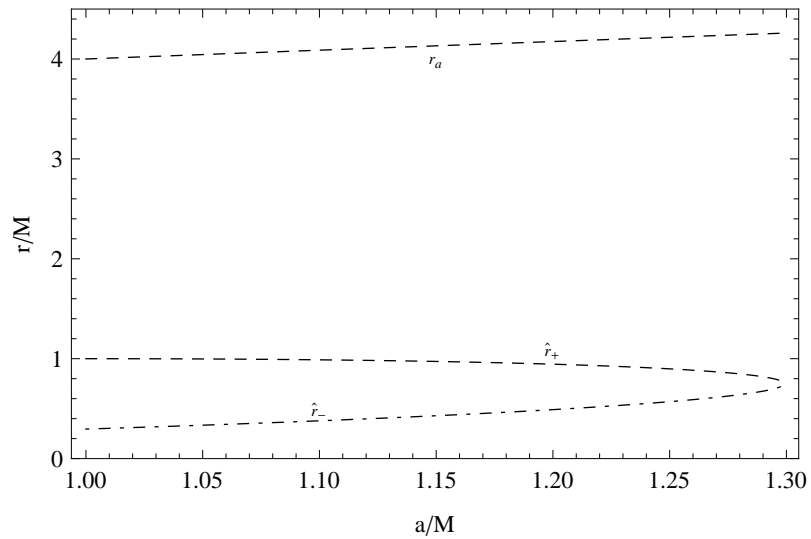


Figure 7.27: The radii r_a and \hat{r}_{\pm} are plotted as functions of a/M . Circular orbits with angular momentum $L = -L_+$ exist for $r > r_a$, with $L = L_-$ in $0 < r < \hat{r}_-$ and $r \geq \hat{r}_+$, and with $L = -L_-$ in $\hat{r}_- < r < \hat{r}_+$ (see text). The dotted dashed gray line represents the outer boundary of the ergosphere $r_+^0 = 2M$.

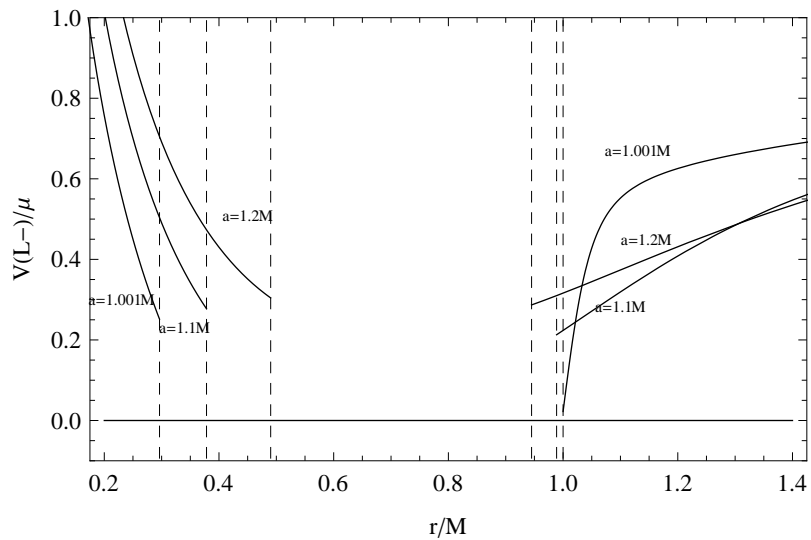


Figure 7.28: The energy $E(L_-)$ of test particles is plotted for selected values of a in the range $M < a < (3\sqrt{3}/4)M$ and for $r > \hat{r}_+$ and $0 < r < \hat{r}_-$.

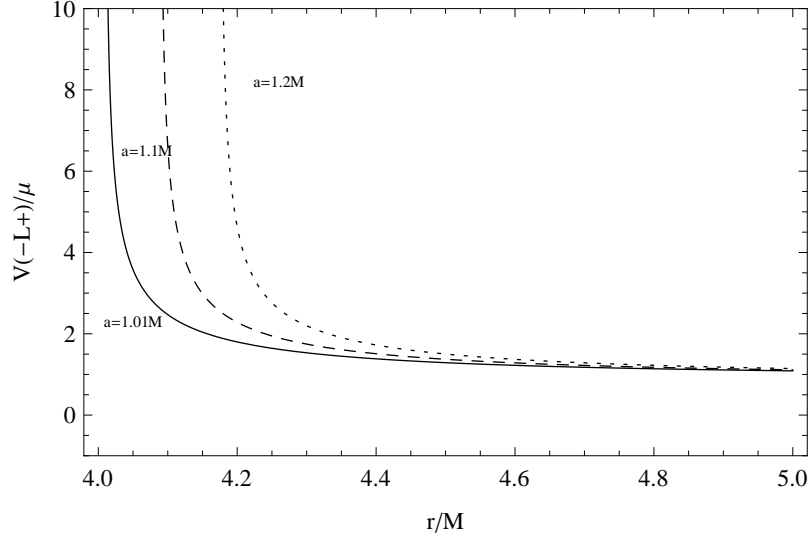


Figure 7.29: The energy $E(-L_+)$ is plotted for selected values of a in the range $M < a < (3\sqrt{3}/4)M$ and for $r > r_a$. The energy $E(-L_+)$ is always strictly positive and increases as the angular momentum a/M increases.

The stability of circular orbits is determined by the turning points of the effective potential. For this case we find numerically two turning points r_{lsc0}^+ and \tilde{r}_{lsc0}^- with $\hat{r}_- < \tilde{r}_{lsc0}^- < \hat{r}_+$ and $r_{lsc0}^+ > r_a$ (see Fig. 7.31), where

$$\tilde{r}_{lsc0}^- \equiv 3 - Z_2 - \sqrt{(3 - Z_1)(3 + Z_1 - 2Z_2)}. \quad (7.4.12)$$

The radii r_{lsc0}^+ and \tilde{r}_{lsc0}^- correspond to the last stable circular orbits with angular $L = -L_+$ and $L = -L_-$ respectively. Then, the distribution of circular orbits in the different regions is as follows:

- In the region $0 < r < \hat{r}_-$, the orbits with $L = L_-$ are unstable.
- In the region $\hat{r}_- < r < \tilde{r}_{lsc0}^-$, the orbits with $L = -L_-$ are unstable.
- In the region $\tilde{r}_{lsc0}^- < r < \hat{r}_+$, the orbits with $L = -L_-$ are stable.
- In the region $\hat{r}_+ < r < r_a$, the orbits with $L = L_-$ are stable.
- In the region $r_a < r < r_{lsc0}^+$, the orbits with $L = -L_+$ are unstable and those with $L = L_-$ are stable.
- In the region $r > r_{lsc0}^+$, the orbits with $L = -L_+$ and $L = L_-$ are stable.

The summary of this case is sketched in Fig. 7.32. As a concrete example, we investigate in detail circular motion around a naked singularity with $a =$

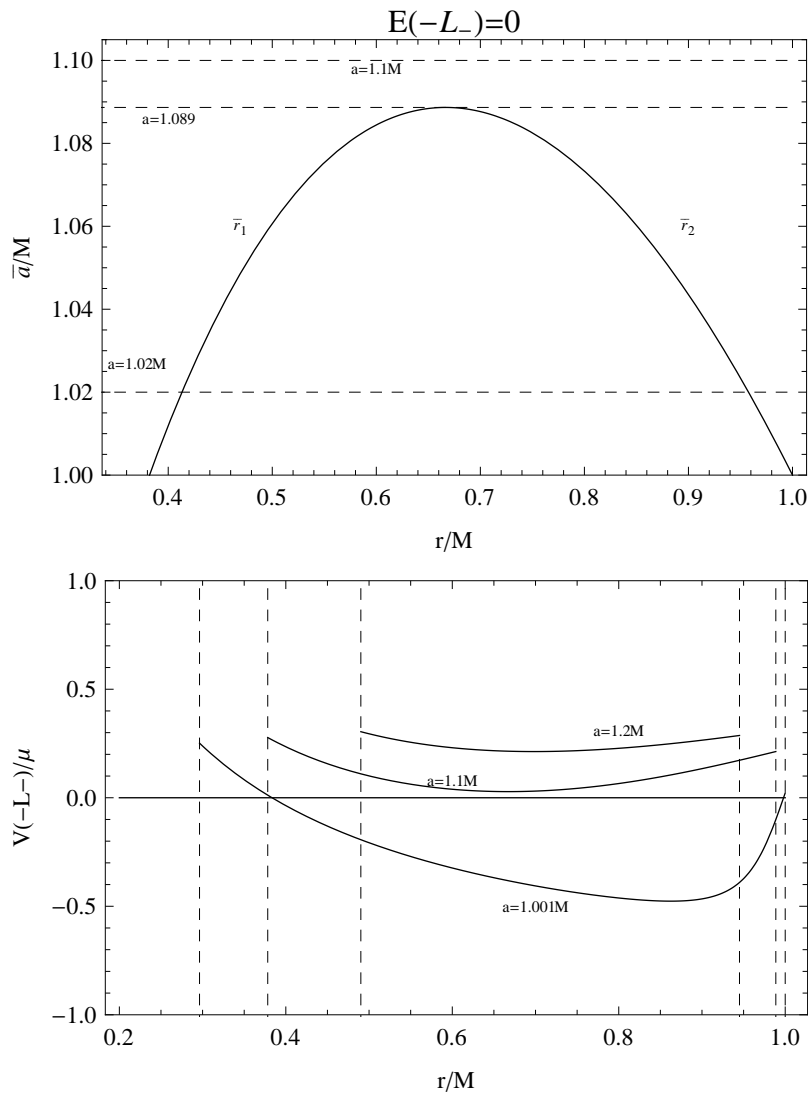


Figure 7.30: The angular momentum $\bar{a} = -(r - 2M)\sqrt{r/M}$ is plotted as a function of r . The energy vanishes, $E(-L_-) = 0$, for $a = \bar{a}$, and is negative, $E(-L_-) < 0$, for $1 < a < \sqrt{32/27}M$ in the interval $\bar{r}_1 < r < \bar{r}_2$. For $a > \sqrt{32/27}M$ the energy $E(-L_-)$ is always strictly positive. For a naked singularity with momentum $a = 1.02M$ the energy $E(-L_-) = 0$ at $r = 0.41M$ and $r = 0.96M$, and $E(-L_-) < 0$ in $0.41M < r < 0.96M$. For $a = \sqrt{32/27}M$ the energy $E(-L_-) = 0$ at $r = 2/3M$, whereas $E(-L_-) > 0$ for $a = 1.1M$. In the upper bottom plot, the energy $E(-L_-)$ is plotted for selected values of a/M in the interval $\hat{r}_- < r < \hat{r}_+$.

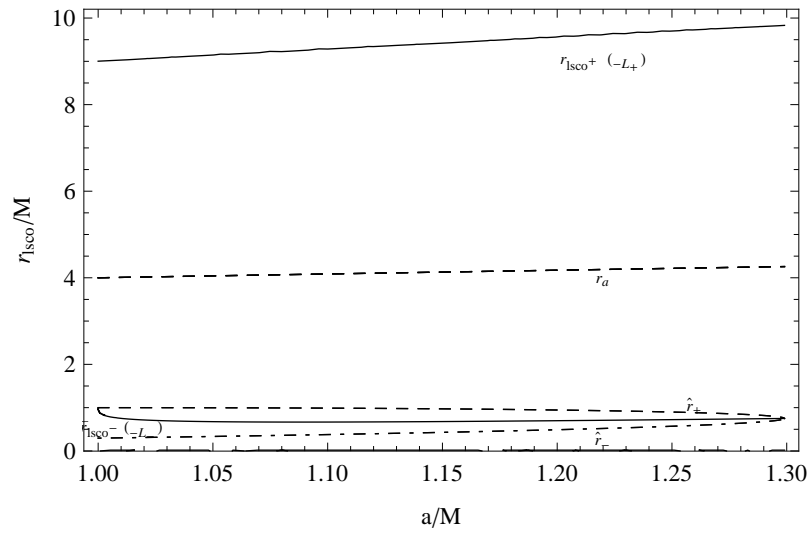


Figure 7.31: The radii r_{isco}^{\pm} of the last stable circular orbits are plotted as functions of the intrinsic angular momentum a in the interval $M < a < \frac{3\sqrt{3}}{4}M$. The radii r_a and \hat{r}_{\pm} are also plotted. The particle angular momentum L_{\pm} is also denoted for some particular radii.

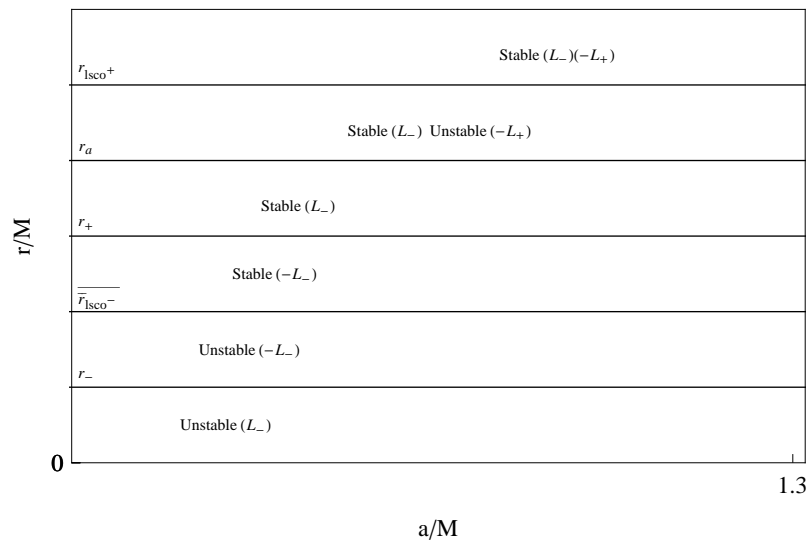


Figure 7.32: Stability of circular orbits in a Kerr naked singularity with $M < a < \frac{3\sqrt{3}}{4}M$. The radii r_{isco}^+ and \tilde{r}_{isco}^- of the last stable circular orbits as functions of the ratio a/M . The special radii r_a and \hat{r}_{\pm} are also plotted.

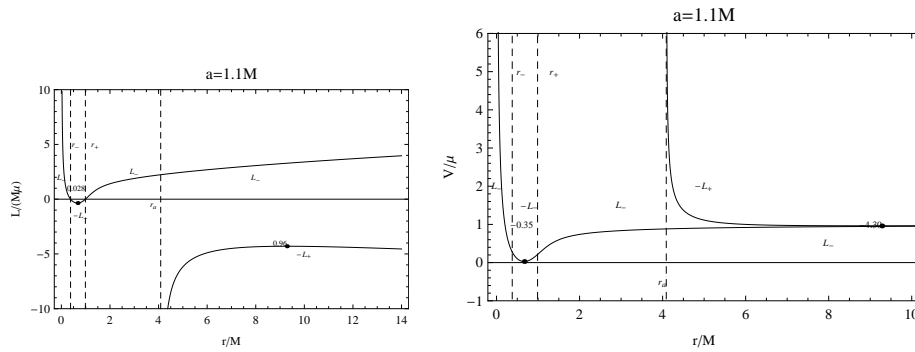


Figure 7.33: Angular momentum and energy of circular orbits in a Kerr naked singularity with $a = 1.1M$. The dots denote the position of the last stable circular orbits, and the numbers close to the dots indicate the value of the energy V/μ or the angular momentum of the last stable circular orbits. In $r > r_a \approx 4.088M$, the particles have angular momentum $L = -L_+$; in $0 < r < \hat{r}_- \approx 0.378M$ and $r \geq \hat{r}_+ \approx 0.989M$, there exist particles with $L = L_-$; in $\hat{r}_- < r < \hat{r}_+$, there exist particles with $L = -L_-$.

$1.1M$. The radii that determine the distribution of test particles in this gravitational field are: $\hat{r}_- \approx 0.378M$, $\tilde{r}_{lsc0}^- \approx 0.989M$, $\hat{r}_+ \approx 0.989M$, $r_a \approx 4.088M$, and $r_{lsc0}^+ \approx 9.280M$. In Fig. 7.33, we illustrate the behavior of the angular momentum and the energy of circular orbits for this special case.

In Fig. 7.34, we show the behavior of the effective potential for some selected values of the orbital angular momentum. The turning points of the effective potential are located at $r_{lsc0}^+ \approx 9.280M$, where $L_{lsc0}^+ \approx -4.298\mu M$ and $V_{lsc0}^+ \approx 0.963\mu$, and at $\tilde{r}_{lsc0}^- \approx 0.667M$, where $L_{lsc0}^- \approx -0.354\mu M$ and $V_{lsc0}^- \approx 0.028\mu$.

The essential results of our analysis can be described by using the model of an accretion disk around the central naked singularity. Considering the properties and positions of the different radii and the positions of the last stable circular orbits, we conclude that the stable accretion disk is composed of three different disks. The internal disk is situated between the radii \tilde{r}_{lsc0}^- and \hat{r}_+ and is made of stable particles of counter-rotating particles with angular momentum $L = -L_-$. Particles situated on the boundary radius \hat{r}_+ turn out to be characterized by a zero value of the angular momentum (cf. Sec. 7.4.3). A second disk made of stable corotating particles with angular momentum $L = L_-$ is situated in the region $\hat{r}_+ < r < r_{lsc0}^+$. Finally, the exterior stable disk is situated in the region $r > r_{lsc0}^+$ and contains corotating particles with $L = L_-$ and counter-rotating particles with $L = -L_+$.

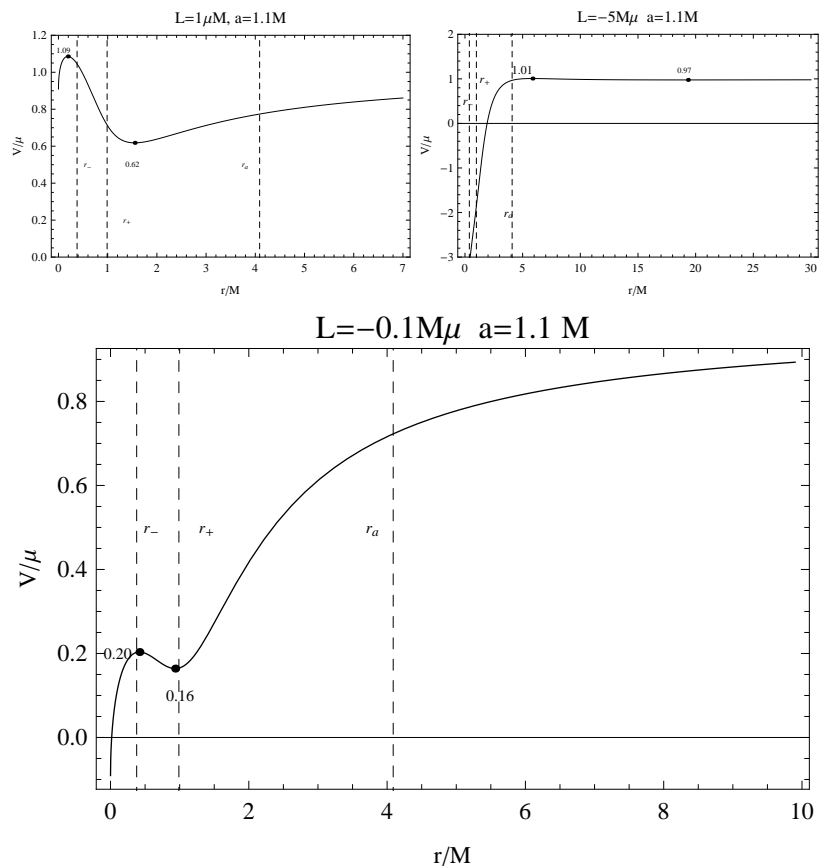


Figure 7.34: The effective potential of a naked singularity with $a = 1.1M$ for fixed values of the particle angular momentum $L/(M\mu)$. The radii r_a and \hat{r}_\pm are also plotted. The dots denote the critical points of the potential. Numbers close to the dots indicate the energy V/μ of the maxima and minima of the effective potential. The dotted dashed gray line represents the outer boundary of the ergosphere $r_+^0 = 2M$.

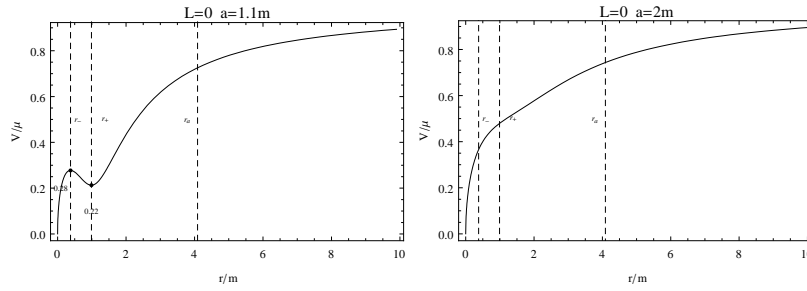


Figure 7.35: The effective potential of a Kerr naked singularity with angular momentum parameter $a = 1.1M$ and $a = 2M$ is plotted for the particle orbital angular momentum $L/(M\mu) = 0$ as a function of the radius r/M . The radii r_a and \hat{r}_{\pm} are also plotted for both cases (see text). The dots represent the critical points of the potential, and the numbers close to the dots indicate the energy V/μ of the maxima and minima of the effective potential. In the case $a = 2M$ no extreme points are observed in the potential.

7.4.3 Orbits with zero angular momentum

An interesting phenomenon that occurs only in the gravitational field of naked singularity is the existence of “circular orbits” with zero angular momentum, as defined by the conditions

$$V = E/\mu, \quad V'(r) = 0, \quad L = 0. \quad (7.4.13)$$

This fact can be interpreted as a consequence of the repulsive gravity effects that characterize the dynamics in the field of the naked singularity. For the repulsive gravity effects in the Kerr spacetime see, for example, [108, 59]. From the expression for the angular momentum derived in Sec. 7.2 one can show that the solution (7.4.13) is allowed only for naked singularities with intrinsic angular momentum within the interval $1 < a/M \leq 3\sqrt{3}/4$. Outside this interval, i.e. for $a/M > 3\sqrt{3}/4$, no orbits exist with zero angular momentum. The behavior of the corresponding effective potential is illustrated in Fig. 7.35.

A further analysis shows that the particles with $L = 0$ are situated on the radii \hat{r}_{\pm} , and that the radius \hat{r}_{-} corresponds to unstable particles while the radius \hat{r}_{+} is within the region of stability. This situation is illustrated in Fig. 7.36.

The analysis of the energy of test particles with $L = 0$ is presented in Fig. 7.37. For the stable particles that are situated on the radius \hat{r}_{+} we can note that the energy is always positive and finite. The maximum value of the energy is reached at the ratio $a/M = 3\sqrt{3}/4$ and the minimum value with $E(\hat{r}_{+}) \rightarrow 0$ corresponds to the limit of the extreme black hole $a/M \rightarrow 1$.

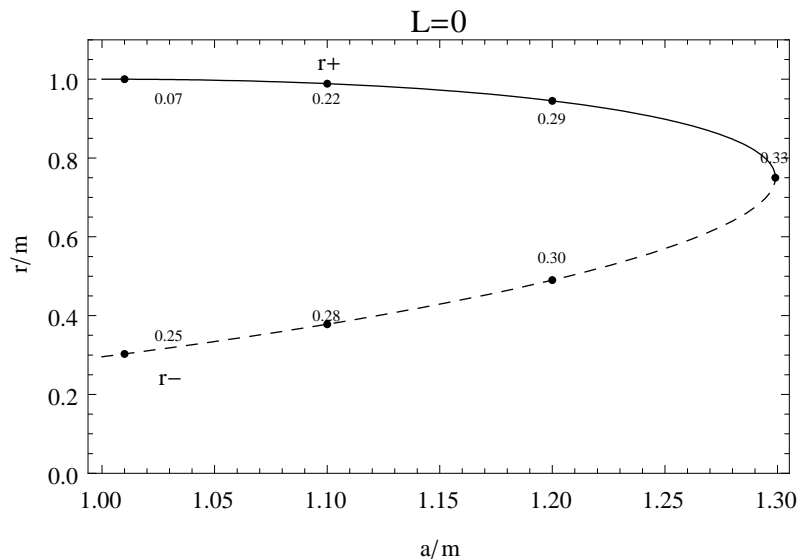


Figure 7.36: Location of particles with $L = 0$ in a Kerr naked singularity with $1 < a/M \leq 3\sqrt{3}/4$. The picture plots the locus of the critical points of the effective potential V/μ with (particle) angular momentum $L/(M\mu) = 0$. The radius of these “circular” orbits is plotted as a function of the source angular momentum a/M . Numbers close to the dots indicate the value of the energy V/μ .

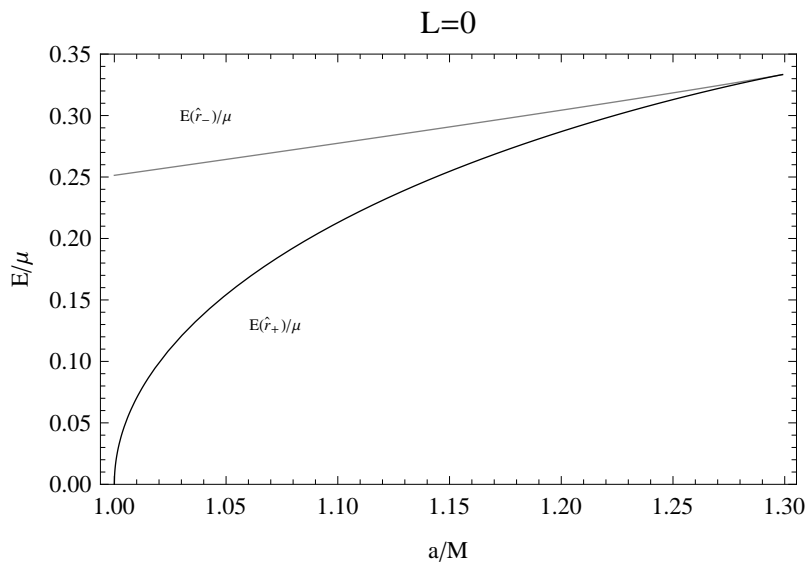


Figure 7.37: The energy particles with $L = 0$ in a naked singularity with $1 < a/M \leq 3\sqrt{3}/4$. The orbits are located on the radii $r = \hat{r}_+$ (stable) and $r = \hat{r}_-$ (unstable). The energies $E(\hat{r}_+)$ (black curve) and $E(\hat{r}_-)$ (gray curve) are plotted as functions of the intrinsic angular momentum a/M . It is possible to see that $E(\hat{r}_+) < E(\hat{r}_-)$ for $1 < a/M < 3\sqrt{3}/4$, and $E(\hat{r}_+) = E(\hat{r}_-)$ for $a/M = 3\sqrt{3}/4$.

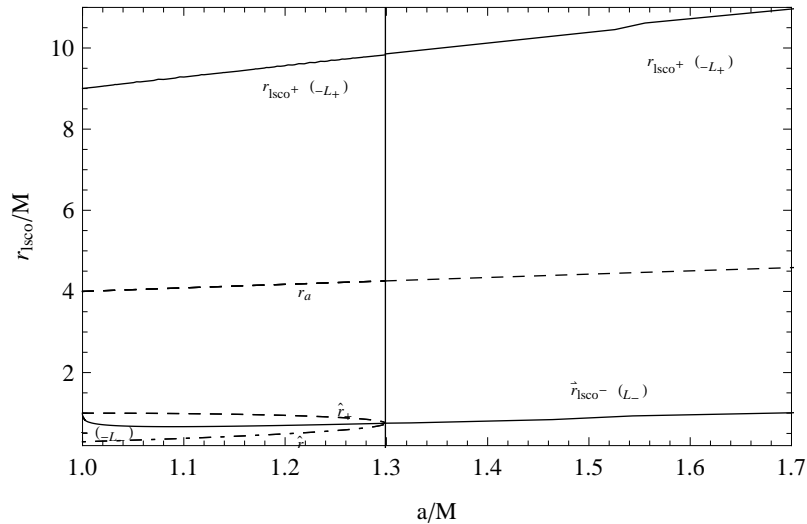


Figure 7.38: The radii r_{lSCO} of the turning points of the effective potential and the special radii r_a and \hat{r}_{\pm} are plotted as functions of the ratio a/M within the interval $[1, 1.7]$. The dotted dashed gray line represents the outer boundary of the ergosphere $r_+^0 = 2M$.

7.4.4 Summary of the naked singularity and black hole cases

In the investigation of the circular motion of test particles around a Kerr naked singularity we found that it is necessary to analyze separately the two regions $a \geq \frac{3\sqrt{3}}{4}M$ and $M < a < \frac{3\sqrt{3}}{4}M$. The distribution of orbits depends on the position of the special radii \hat{r}_{\pm} , given by Eq. (7.4.6), r_a , given by Eq. (7.4.2), and the position of the last stable circular orbits r_{lSCO}^+ , as given in Eq.(7.3.11), \tilde{r}_{lSCO}^- in Eq. (7.4.12) and \bar{r}_{lSCO} , as given in Eq.(7.4.3). Notice that although the radius \bar{r}_{lSCO} is the geometric continuation of the radius \tilde{r}_{lSCO}^- for the interval $a/M > 3\sqrt{3}/4$, their values are determined by different analytical expressions as follows from Eqs.(7.3.11) and (7.4.3). The arrangement of these radii in the interval $1 < a/M < 1.7$ is depicted in Fig. 7.38.

The tables 7.2 and 7.3 summarize the distribution and stability properties of test particles in circular motion in the field of a rotating naked singularity for the two different regions of values of the intrinsic angular momentum.

For the sake of completeness, we show in Fig. 7.39 the behavior of the energies $E_{lSCO}^+ = E(r_{lSCO}^+)$ and $E_{lSCO}^- = E(r_{lSCO}^-)$ and angular momenta $L_{lSCO}^+ = L(r_{lSCO}^+)$ and $L_{lSCO}^- = L(r_{lSCO}^-)$, for the last stable circular orbits in terms of the ratio a/M of the naked singularity. Notice that, as expected from a physical viewpoint, for a fixed value of the ratio a/M the energy of the exterior last stable circular orbit $E(r_{lSCO}^+)$ is always smaller than the corresponding energy of the interior particle $E(r_{lSCO}^-)$.

Our analysis of Kerr black holes and naked singularities shows that the properties of circular orbits depend strongly on their radial distance with respect to the central source. The critical radii that are found in the analysis

Case: $M < a < (3\sqrt{3}/4)M$

Region	Angular momentum	Stability
$]0, \hat{r}_- [$	L_-	\tilde{r}_{lsc0}
$] \hat{r}_-, \hat{r}_+ [$	$-L_-$	\tilde{r}_{lsc0}
$] \hat{r}_+, \infty [$	L_-	\tilde{r}_{lsc0}
$] r_a, \infty [$	$-L_+$	r_{lsc0}^+
$]0, \hat{r}_- [$	L_-	Unstable
$] \hat{r}_-, \tilde{r}_{lsc0} [$	$-L_-$	Unstable
$] \tilde{r}_{lsc0}, \hat{r}_+ [$	$-L_-$	Stable
$] \hat{r}_+, r_a [$	L_-	Stable
$] r_a, r_{lsc0}^+ [$	$L_- (-L_+)$	Stable (Unstable)
$] r_{lsc0}^+, \infty [$	$(L_-, -L_+)$	Stable

Table 7.2: Distribution and stability properties of circular orbits for a test particle in a Kerr naked singularity with $M < a < (3\sqrt{3}/4)M$. For each region we present the value of the orbital angular momentum of the particle as determined by Eq. (7.2.11).

Case: $a \geq (3\sqrt{3}/4)M$

Region	Angular momentum	Stability
$]0, \infty [$	L_-	\tilde{r}_{lsc0}
$] r_a, \infty [$	$-L_+$	r_{lsc0}^+
$(3\sqrt{3}/4)M < a < 9M$ ($\tilde{r}_{lsc0} < r_a < r_{lsc0}^+$)		
$]0, \tilde{r}_{lsc0} [$	L_-	Unstable
$] \tilde{r}_{lsc0}, r_a [$	L_-	Stable
$] r_a, r_{lsc0}^+ [$	$L_- (-L_+)$	Stable (Unstable)
$] r_{lsc0}^+, \infty [$	$(L_-, -L_+)$	Stable
$a \geq 9M$ ($r_a < \tilde{r}_{lsc0} < r_{lsc0}^+$)		
$]0, r_a [$	L_-	Unstable
$] r_a, \tilde{r}_{lsc0} [$	$(L_-, -L_+)$	Unstable
$] \tilde{r}_{lsc0}, r_{lsc0}^+ [$	$L_- (-L_+)$	Stable (Unstable)
$] r_{lsc0}^+, \infty [$	$(L_-, -L_+)$	Stable

Table 7.3: Distribution and stability properties of circular orbits for a test particle in a Kerr naked singularity with $a \geq (3\sqrt{3}/4)M$. For each region we present the value of the orbital angular momentum of the particle as determined by Eq. (7.2.11).

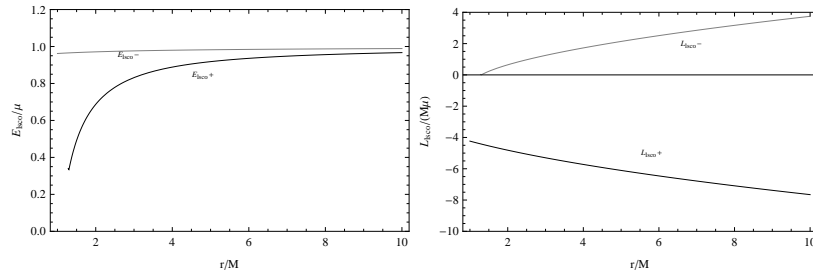


Figure 7.39: Behavior of the E_{lsc0}/μ and the angular momentum for the last stable circular orbits as functions of the intrinsic angular momentum of the naked singularity.

of the conditions for circular motion determine the angular momentum and the energy of the test particles. The arrangement of those special radii and the positions of the last stable circular orbits is depicted in Fig. 7.40 for the relevant ranges of the ratio a/M .

The radii r_a , r_γ , \hat{r}_+ , and \hat{r}_- determine the angular momentum and direction of rotation of test particles at a given distance from the central source. In addition, the radii r_{lsc}^\pm determine the position of the last stable circular orbits with a given angular momentum of the test particle.

If we imagine an infinitesimal thin disk made of test particles in circular orbits around the central compact object, the above results show that the geometric structure of the disk is sufficient to distinguish between black holes and naked singularities. For such hypothetical disk to be a meaningful approximation of a physically realizable disk, it is necessary that the individual particle orbits be stable with respect to infinitesimal perturbations. In the case of radial perturbations, stability is guaranteed as a consequence of the fact that the disk is made of stable particles in circular motion, as described above. As for perturbations out of the equatorial plane, the analysis of stability has been performed by using the geodesic equations [109], the phase space method [110], and the Rayleigh criterion [111, 112]. Although the last method has been applied only to static central sources, the generalization to include rotating sources seems to be straightforward. All those methods show that equatorial circular orbits around a Kerr black hole are stable under out-of-equatorial-plane perturbations as long as the angular momentum per unit mass of the test particles increases monotonically as the distance to the axis of symmetry increases. A complementary analysis must be performed in the case of naked singularities; however, a brief inspection of the analytical results obtained by using the phase space method seems to indicate that the stability does not depend drastically on the mass-to-angular-momentum ratio of the central body. In general, one can expect that the stability with respect to radial and out-of-equatorial-plane perturbations depends on the ratio of source rotation to particle angular momentum.

7.5 Remarks

In this work, we investigated the circular motion of test particles around a rotating central mass whose gravitational field is described by the Kerr spacetime. We limit ourselves to the study of circular orbits situated on the equatorial plane $\theta = \pi/2$. First, we derive the conditions for the existence of circular orbits by using the fact the geodesic motion in this case can be reduced to the motion of test particles in an effective potential. In this procedure, two constants of motion arise, E and L , which are interpreted as the energy and the angular momentum of the test particles, respectively. We concentrate on the analysis of the conditions for the existence of circular orbits

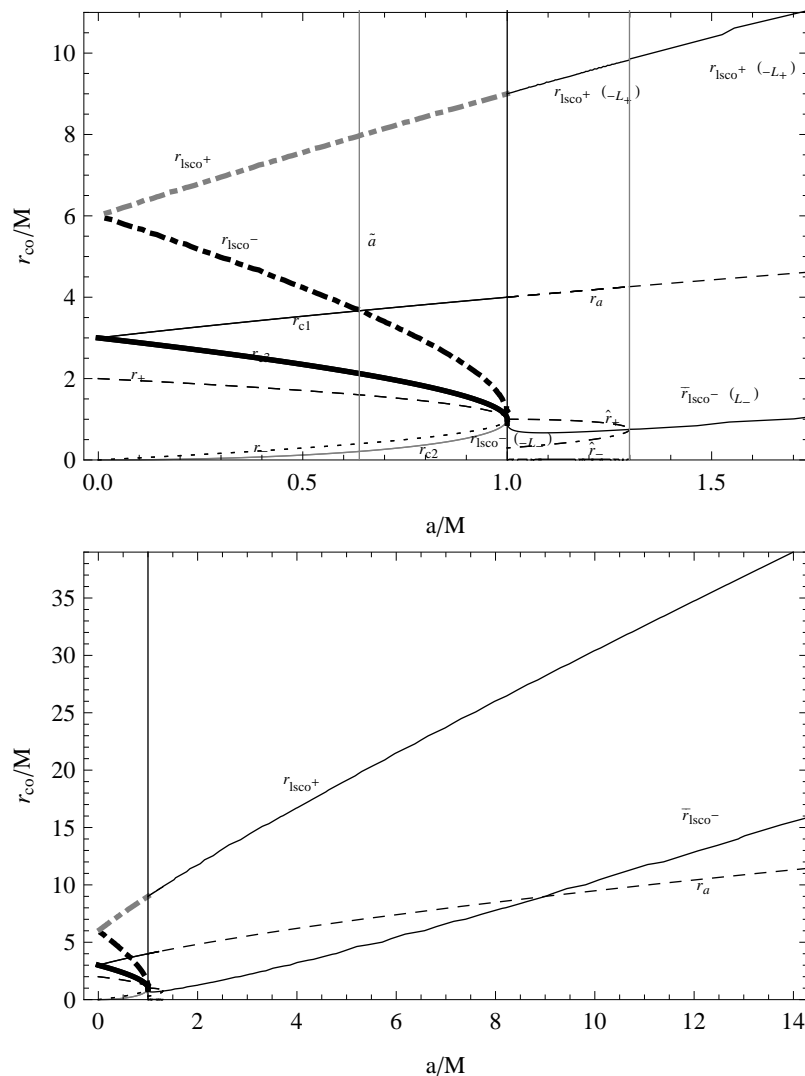


Figure 7.40: Arrangement of the radii determining the properties of circular orbits around a rotating central mass. The upper plot is for black holes and naked singularities with intrinsic angular momentum $a/M \in [0, 1.7]$. The bottom plot is for rotating naked singularities with $a/M \in [1.7, 14]$. The dotted dashed gray line represents the outer boundary of the ergosphere $r_+^0 = 2M$.

and their consequences for the values of the energy and angular momentum of the test particles. Our analysis covers completely the range of values of the intrinsic angular momentum of the central mass, including black holes and naked singularities. We find all the regions of the equatorial plane where circular motion is allowed and analyze the behavior of the energy and the angular momentum of the test particles in those regions. Moreover, the stability properties of all the allowed circular orbits was investigated in detail.

For our analysis we consider separately the case of black holes with ratio $a/M \leq 1$ and naked singularities $a/M > 1$, where M is the mass and a is the specific angular momentum J/M of the central body. Moreover, in the case of naked singularities it turns out that the physical properties of the circular motion depend on the value of the ratio a/M so that it is necessary to explore two different ranges: $1 < a/M < 3\sqrt{3}/4$ and $a/M > 3\sqrt{3}/4$. The essential part of our results can be formulated in a plausible manner by using the model of an accretion disk made of stable test particles which are rotating around the central mass.

In the case of a black hole ($a/M \leq 1$), we find that the accretion disk is composed of an interior disk situated within the radii $[r_{lsc0}^-, r_{lsc0}^+]$ and an exterior disk in the region $r > r_{lsc0}^+$, where r_{lsc0}^\pm represent the radius of the last stable circular orbit with angular momentum $L = \mp L_\pm$; moreover, the value of L_\pm depends on the radius r of the circular orbit and on the ratio a/M of the central body [cf. Eq.(7.2.11)]. A similar accretion disk is found around naked singularities with $a/M > 3\sqrt{3}/4$. The only difference is that in the case of a naked singularity the interior disk, situated within the radii $[\bar{r}_{lsc0}^-, r_{lsc0}^+]$, has a minimum size of $r_{lsc0}^+ - \bar{r}_{lsc0}^- > 8M$, whereas in the case of a black hole the size of the inner disk is always less than $8M$ and disappears as $a \rightarrow 0$.

For naked singularities in the range $1 < a/M \leq 3\sqrt{3}/4$ we find that the stable accretion disk is composed of three different disks. The internal disk is situated between the radii \tilde{r}_{lsc0}^- and $\hat{r}_+ < r_{lsc0}^+$ and is made of stable counter-rotating particles with angular momentum $L = -L_-$. The radius \hat{r}_+ corresponds to circular orbits with zero angular momentum ($V = E/\mu$, $V'(r) = 0$, $L = 0$). A second disk made of stable corotating particles with angular momentum $L = L_-$ is situated in the region $\hat{r}_+ < r < r_{lsc0}^+$. Finally, the exterior stable disk is situated in the region $r > r_{lsc0}^+$ and contains corotating particles with $L = L_-$ and counter-rotating particles with $L = -L_+$. We conclude that the main difference between a rotating black hole and a rotating naked singularity consists in the different geometric structure of their accretion disks.

The study of the dynamics of test particles around compact rotating objects is surely interesting from the point of view of the astrophysical phenomenology. However, an immediate application of this study will be in the physics of the accretion disks as observed around astrophysical rotating objects (see [113, 114, 115] and also [117, 108, 118, 119], for the problem concerning the extended theories of gravity see for example [120]). The matter constituents,

plasma elements, are the material of the electromagnetic jets as seen in the X-rays and γ -ray emissions. In this respect, a detailed and proper description of the test particle dynamics is the first step towards the construction of a realistic model for accretion disks around Kerr sources (see [121, 108, 122, 123], and also [124] and [125]).

In this work, we also explored the physics of naked singularities (see also [32, 31, 60, 81]). As no naked singularity has been yet observed and furthermore the existence of these objects is still a subject under intensive theoretical debate, the analysis of the dynamical properties of these objects is clearly important either for a formalization of a complete theoretical picture of the physical features of these solutions, or for observational issues [126, 127], [128, 129, 130, 131] see also [132, 34]. We expect to generalize this work to include the physical contribution of a charged source, therefore, exploring the Kerr–Newman metric which properly describes the spacetime of a rotating, electrically charged, compact object in general relativity [83].

8 On the search for interior solutions

It is well known that Newtonian theory of gravitation provides an adequate description of the interior and exterior gravitational field of conventional astrophysical objects. Indeed, the expansion of the gravitational potential in terms of multipole moments turned out to be the cornerstone to understand the and solve the corresponding field equations.

On the other hand, the discovery of exotic compact objects such as quasars and pulsars together with the possibility of continued gravitational collapse to a black hole points to the importance of relativistic gravitation in astrophysics. Moreover, advances in space exploration and the development of modern measuring techniques have made it necessary to take relativistic effects into account even in the Solar system. It is therefore of importance and interest to describe the relativistic gravitational fields of astrophysical compact objects in terms of their multipole moments, in close analogy with the Newtonian theory, taking into account their rotation and their internal structure.

In this context, the first exterior solution with only a monopole moment was discovered by Schwarzschild [133], soon after the formulation of Einstein's theory of gravity. In 1917, Weyl [4] showed that the problem of finding static axisymmetric vacuum solutions can generically be reduced to a single linear differential equation whose general solution can be represented as an infinite series. The explicit form of this solution resembles the corresponding solution in Newtonian's gravity, indicating the possibility of describing the gravitational field by means of multipole moments. In 1918, Lense and Thirring [134] discovered an approximate exterior solution which, apart from the mass monopole, contains an additional parameter that can be interpreted as representing the angular momentum of the massive body. From this solution it became clear that, in Einstein's relativistic theory, rotation generates a gravitational field that leads to the dragging of inertial frames (Lense-Thirring effect). This is the so-called gravitomagnetic field which is of special importance in the case of rapidly rotating compact objects. The case of a static axisymmetric solution with monopole and quadrupole moment was analyzed in 1959 by Erez and Rosen [9] by using spheroidal coordinates which are specially adapted to describe the gravitational field of nonspherically symmetric bodies. The exact exterior solution which considers arbitrary values for the angular momentum was found by Kerr only in 1963.

The problem of finding exact solutions changed dramatically after Ernst [2] discovered in 1968 a new representation of the field equations for stationary axisymmetric vacuum solutions. In fact, this new representation was the starting point to investigate the Lie symmetries of the field equations. Today, it is known that for this special case the field equations are completely integrable and solutions can be obtained by using the modern solution generating techniques [12]. In this work, we will analyze a particular class of solutions, derived by Quevedo and Mashhoon [136] in 1991, which in the most general case contains infinite sets of gravitational and electromagnetic multipole moments. Hereafter this solution will be denoted as the QM solution.

As for the interior gravitational field, the situation is more complicated. There exists in the literature a reasonable number of interior spherically symmetric solutions which can be matched with the exterior Schwarzschild metric. Nevertheless, a major problem of classical general relativity consists in finding a physically reasonable interior solution for the exterior Kerr metric. Although it is possible to match numerically the Kerr solution with the interior field of an infinitely tiny rotating disk of dust, such a hypothetical system does not seem to be of relevance to describe astrophysical compact objects. It is now widely believed that the Kerr solution is not appropriate to describe the exterior field of rapidly rotating compact objects. Indeed, the Kerr metric takes into account the total mass and the angular momentum of the body. However, the moment of inertia is an additional characteristic of any realistic body which should be considered in order to correctly describe the gravitational field. As a consequence, the multipole moments of the field created by a rapidly rotating compact object are different from the multipole moments of the Kerr metric. For this reason a solution with arbitrary sets of multipole moments, such as the QM solution, can be used to describe the exterior field of arbitrarily rotating mass distributions.

In the case of slowly rotating compact objects it is possible to find approximate interior solutions with physically meaningful energy-momentum tensors and state equations. Because of its physical importance, we will study the Hartle-Thorne [138, 139] interior solution which can be coupled to an approximate exterior metric. Hereafter this solution will be denoted as the HT solution. One of the most important characteristics of this family of solutions is that the corresponding equation of state has been constructed using realistic models for the internal structure of relativistic stars. Semi-analytical and numerical generalizations of the HT metrics with more sophisticated equations of state have been proposed by different authors. A comprehensive review of these solutions is given in [137]. In all these cases, however, it is assumed that the multipole moments (quadrupole and octupole) are relatively small and that the rotation is slow.

To study the physical properties of solutions of Einstein's equations, Fock [141] proposed an alternative method in which the parameters entering the

exterior metric are derived by using physical models for the internal structure of the body. In this manner, the significance of the exterior parameters become more plausible and the possibility appear of determining certain aspects of the interior structure of the object by using observations performed in the exterior region of the body. Fock's metric in its first-order approximation was recently generalized in 1985 by Abdildin [142] to include the case of a rotating object.

8.1 The Hartle-Thorne metrics

To second order in the angular velocity, the structure of compact objects can be approximately described by the mass and quadrupole moments. An important consequence of this approximation is that the equilibrium equations reduce to a set of ordinary differential equations. Hartle and Thorne [138, 139] explored the gravitational field of rotating stars in this slow rotation approximation. This formalism can be applied in most compact objects including pulsars with millisecond rotational periods, but it shows large discrepancies in the case of rapidly rotating relativistic objects near the mass-shedding limit [137], i. e., when the angular velocity of the object reaches the angular velocity of a particle in a circular Keplerian orbit at the equator. An additional property of this formalism is that it can be used to match the interior solution with an approximate exterior solution. In the following subsections we will present the interior and exterior metric and introduce notations which will be used throughout the paper.

If a compact object is rotating slowly, the calculation of its equilibrium properties reduces drastically because it can be considered as a linear perturbation of an already-known non-rotating configuration. This is the main idea of Hartle's formalism [138]. To simplify the computation the following conditions are assumed to be satisfied.

- 1) There exists an one-parameter equation of state. The matter in equilibrium configuration is assumed to satisfy a one-parameter equation of state, $\mathcal{P} = \mathcal{P}(\mathcal{E})$, where \mathcal{P} is the pressure and \mathcal{E} is the density of total mass-energy.
- 2) Axial and reflection symmetry. The configuration is symmetric with respect to an arbitrary axis which can be taken as the rotation axis. Furthermore, the rotating object should be invariant with respect to reflections about a plane perpendicular to the axis of rotation.
- 3) Uniform rotation. Only uniformly rotating configurations were considered. It was shown previously that configurations which minimize the total mass-energy (e.g., all stable configurations) must rotate uniformly [145].
- 4) Slow rotation. This means that angular velocities Ω are small enough so that the fractional changes in pressure, energy density and gravitational field due to the rotation are all less than unity, i.e.

$$\Omega^2 \ll \left(\frac{c}{\mathcal{R}}\right)^2 \frac{GM}{c^2 \mathcal{R}} \quad (8.1.1)$$

where \mathcal{M} is the mass and \mathcal{R} is the radius of the non-rotating configuration. The above condition is equivalent to the physical requirement $\Omega \ll c/\mathcal{R}$.

When the equilibrium configuration described above is set into slow rotation, the geometry of space-time around it and its interior distribution of stress-energy are changed. With an appropriate choice of coordinates, the perturbed geometry is described by

$$ds^2 = e^\nu [1 + 2(h_0 + h_2 P_2)] dt^2 - \frac{[1 + 2(m_0 + m_2 P_2)/(R - 2M')]}{1 - 2M'/R} dR^2 - R^2 [1 + 2(v_2 - h_2) P_2] [d\Theta^2 + \sin^2 \Theta (d\phi - \omega dt)^2] + O(\Omega^3) \quad (8.1.2)$$

Here M' is the mass of non-rotating star, $P_2 = P_2(\cos \Theta)$ is the Legendre polynomial of second order, ω is "the angular velocity of the local inertial frame" which is the function of R and is proportional to the star's angular velocity Ω , and h_0, h_2, m_0, m_2, v_2 are all functions of R that are proportional to Ω^2 .

In the above coordinate system the fluid inside the star moves with the 4-velocity appropriate to uniform and rigid rotation [140], of which the contravariant components are

$$u^t = (g_{tt} + 2\Omega g_{t\phi} + \Omega^2 g_{\phi\phi})^{-1/2}, \quad u^\phi = \Omega u^t, \quad u^R = u^\Theta = 0. \quad (8.1.3)$$

The quantity

$$\bar{\omega} \equiv \Omega - \omega, \quad (8.1.4)$$

which appears in the expression for u^t , is the angular velocity of the fluid relative to the local inertial frame. It plays a fundamental role in the equations of structure below. The density of mass-energy and pressure of the fluid are affected by rotation because the rotation deforms the star. In the interior of the star at given (R, Θ) , in a reference frame that is momentarily moving with the fluid, the pressure is

$$\mathcal{P} \equiv P + (E + P)(p_0^* + p_2^* P_2) = P + \Delta P; \quad (8.1.5)$$

the density of mass-energy is

$$\mathcal{E} \equiv E + (E + P)(dE/dP)(p_0^* + p_2^* P_2) = E + \Delta E. \quad (8.1.6)$$

Here, p_0^* and p_2^* are dimensionless functions of R , proportional to Ω^2 , which

describe the pressure perturbation; all other parameters were defined above. The stress-energy tensor for the fluid in the rotating star is

$$T_{\mu}^{\nu} = (\mathcal{E} + \mathcal{P})u_{\mu}u^{\nu} - \mathcal{P}\delta_{\mu}^{\nu}. \quad (8.1.7)$$

The rotational perturbations of the star's structure are described by the functions $\bar{\omega}, h_0, m_0, p_0^*, h_2, m_2, v_2, p_2^*$. These functions are calculated from Einstein's field equations (for details see [138, 139]).

The HT metric describing the exterior field of a slowly rotating slightly deformed object is given by

$$\begin{aligned} ds^2 = & \left(1 - \frac{2\mathcal{M}}{R}\right) \left[1 + 2k_1 P_2(\cos \Theta) + 2 \left(1 - \frac{2\mathcal{M}}{R}\right)^{-1} \frac{J^2}{R^4} (2 \cos^2 \Theta - 1)\right] dt^2 \\ & - \left(1 - \frac{2\mathcal{M}}{R}\right)^{-1} \left[1 - 2k_2 P_2(\cos \Theta) - 2 \left(1 - \frac{2\mathcal{M}}{R}\right)^{-1} \frac{J^2}{R^4}\right] dR^2 \\ & - R^2 [1 - 2k_3 P_2(\cos \Theta)] (d\Theta^2 + \sin^2 \Theta d\phi^2) + 4 \frac{J}{R} \sin^2 \Theta dt d\phi \end{aligned} \quad (8.1.8)$$

where

$$\begin{aligned} k_1 &= \frac{J^2}{\mathcal{M}R^3} \left(1 + \frac{\mathcal{M}}{R}\right) + \frac{5}{8} \frac{Q - J^2/\mathcal{M}}{\mathcal{M}^3} Q_2^2 \left(\frac{R}{\mathcal{M}} - 1\right), \\ k_2 &= k_1 - \frac{6J^2}{R^4}, \\ k_3 &= k_1 + \frac{J^2}{R^4} + \frac{5}{4} \frac{Q - J^2/\mathcal{M}}{\mathcal{M}^2 R} \left(1 - \frac{2\mathcal{M}}{R}\right)^{-1/2} Q_2^1 \left(\frac{R}{\mathcal{M}} - 1\right), \end{aligned}$$

and

$$Q_2^1(x) = (x^2 - 1)^{1/2} \left[\frac{3x}{2} \ln \frac{x+1}{x-1} - \frac{3x^2 - 2}{x^2 - 1} \right], \quad (8.1.9)$$

$$Q_2^2(x) = (x^2 - 1) \left[\frac{3}{2} \ln \frac{x+1}{x-1} - \frac{3x^3 - 5x}{(x^2 - 1)^2} \right], \quad (8.1.10)$$

are the associated Legendre functions of the second kind. The constants \mathcal{M}, J and Q are related to the total mass, angular momentum and mass quadrupole moment of the rotating star, respectively. The total mass of a rotating configuration is defined as $\mathcal{M} = M' + \delta M$, where M' is the mass of non-rotating configuration and δM is the change in mass of the rotating from the non-rotating configuration with the same central density. It should be stressed that in the terms involving J^2 and Q the total mass \mathcal{M} can be substituted by M' since δM is already a second order term in angular velocity. This form of the metric corrects some misprints of the original paper by Hartle and Thorne

[139] (see also [116] and [117]).

In general the HT metric represents an approximate vacuum solution, accurate to second order in the angular momentum J and to first order in the quadrupole parameter Q . In the case of ordinary stars, such as the Sun, considering the gravitational constant G and the speed of light c , the metric (8.1.8) can be further simplified due to the smallness of the parameters:

$$\frac{GM_{Sun}}{c^2\mathcal{R}_{Sun}} \approx 10^{-6}, \quad \frac{GJ_{Sun}}{c^3\mathcal{R}_{Sun}^2} \approx 10^{-12}, \quad \frac{GQ_{Sun}}{c^2\mathcal{R}_{Sun}^3} \approx 10^{-12}. \quad (8.1.11)$$

There are two ways to incorporate this limit into the metric (8.1.8): either as $R \rightarrow \infty$ or as $c \rightarrow \infty$. As for the first case, it is necessary that R be a well-defined radial coordinate, whereas the second one can be carried out in an invariant manner only by using the frame theory developed sometime ago by Ehlers [146]. The result of the limit $R \rightarrow \infty$ has been presented in [139] and the corresponding metric describes the gravitational field of the Sun with an accuracy of one part in 10^{12} . To calculate the limit $c \rightarrow \infty$ in the Ehlers invariant formalism, it is necessary to perform an appropriate coordinate transformation, and to apply the invariant limits as defined in the frame theory. The computations are straightforward and lead to

$$\begin{aligned} ds^2 = & \left[1 - \frac{2GM}{c^2R} + \frac{2GQ}{c^2R^3}P_2(\cos \Theta) + \frac{2G^2MQ}{c^4R^4}P_2(\cos \Theta) \right] c^2 dt^2 \\ & + \frac{4GJ}{c^2R} \sin^2 \Theta dt d\phi - \left[1 + \frac{2GM}{c^2R} - \frac{2GQ}{c^2R^3}P_2(\cos \Theta) \right] dR^2 \\ & - \left[1 - \frac{2GQ}{c^2R^3}P_2(\cos \Theta) \right] R^2 (d\Theta^2 + \sin^2 \Theta d\phi^2). \quad (8.1.12) \end{aligned}$$

This metric describes the gravitational field for a wide range of compact objects, and only in the case of very dense ($GM \sim c^2\mathcal{R}$) or very rapidly rotating ($GJ \sim c^3\mathcal{R}^2$) objects large discrepancies will appear.

If a compact object is rotating slowly, the calculation of its equilibrium properties reduces drastically because it can be considered as a linear perturbation of an already-known non-rotating configuration. This is the main idea of Hartle's formalism [138]. To simplify the computation the following conditions are assumed to be satisfied.

- 1) There exist an one-parameter equation of state. The matter in equilibrium configuration is assumed to satisfy a one-parameter equation of state, $\mathcal{P} = \mathcal{P}(\mathcal{E})$, where \mathcal{P} is the pressure and \mathcal{E} is the density of total mass-energy.
- 2) Axial and reflection symmetry. The configuration is symmetric with respect to an arbitrary axis which can be taken as the rotation axis. Furthermore, the rotating object should be invariant with respect to reflections about a plane perpendicular to the axis of rotation
- 3) Uniform rotation. Only uniformly rotating configurations were consid-

ered. It was shown previously that configurations which minimize the total mass-energy (e.g., all stable configurations) must rotate uniformly [143].

4) Slow rotation. It means that angular velocities Ω are small enough so that the fractional changes in pressure, energy density and gravitational field due to the rotation are all less than unity, i.e.

$$\Omega^2 \ll \left(\frac{c}{\mathcal{R}}\right)^2 \frac{GM}{c^2 \mathcal{R}} \quad (8.1.13)$$

where M is the mass and \mathcal{R} is the radius of the non-rotating configuration. The above condition is equivalent to the physical requirement $\Omega \ll c/\mathcal{R}$.

Under the above assumptions, the line element for the interior solution is given by

$$ds^2 = \left(1 + \frac{2\Phi}{c^2}\right) c^2 dt^2 - \left[1 + \frac{2R}{c^2} \frac{d\Phi_0(R)}{dR} + \Phi_2(R) P_2(\cos \Theta)\right] dR^2 - R^2 \left[1 + \frac{2\Phi_2(R)}{c^2} P_2(\cos \Theta)\right] (d\Theta^2 + \sin^2 \Theta d\phi^2), \quad (8.1.14)$$

where

$$\Phi = \Phi_0(R) + \Phi_2(R) P_2(\cos \Theta), \quad (8.1.15)$$

is the interior Newtonian potential, Φ_0 is the interior Newtonian potential for the non-rotating configuration, Φ_2 is the perturbation due to the rotation, and $P_2(\cos \Theta)$ is the Legendre polynomial of first kind [138]. The interior solution (8.1.14) satisfies Einstein field equations

$$R_\mu^\nu - \frac{1}{2} \delta_\mu^\nu R = \frac{8\pi G}{c^4} T_\mu^\nu \quad (8.1.16)$$

where the stress-energy tensor is that of a perfect fluid

$$T_\mu^\nu = (\mathcal{E} + \mathcal{P}) u^\nu u_\mu + \mathcal{P} \delta_\mu^\nu. \quad (8.1.17)$$

The 4-velocity which satisfies the normalization condition $u^\mu u_\mu = 1$ is

$$u^R = u^\Theta = 0, \quad u^\phi = \Omega u^t, \quad u^t = \left(g_{tt} + 2\Omega g_{t\phi} + \Omega^2 g_{\phi\phi}\right)^{-1/2}, \quad (8.1.18)$$

where the angular velocity Ω is a constant throughout the fluid.

8.2 Fock's approximate method

Fock's first-order approximation metric was recently derived and investigated by Abdildin [147]. Initially this metric was written in its original form

in harmonic coordinate system [148, 149] as follows

$$ds^2 = \left[c^2 - 2U + \frac{2U^2}{c^2} - \frac{2G}{c^2} \int \frac{\rho' \left(\frac{3}{2}v^2 + \Pi - U \right)' - P'_{kk}}{|\vec{r} - \vec{r}'|} (dx')^3 \right] dt^2 - \left[1 + \frac{2U}{c^2} \right] (dx_1^2 + dx_2^2 + dx_3^2) + \frac{8}{c^2} (U_1 dx_1 + U_2 dx_2 + U_3 dx_3) dt, \quad (8.2.1)$$

where U is the Newtonian gravitational potential, ρ is the mass density of the body, v is the speed of the particles inside the body (liquid), Π is the elastic energy per unit mass, P_{ik} is the stress tensor, \vec{U} is the gravitational vector potential. Newton's potential satisfies the equation $\Delta U = 4\pi G\rho$. The solution of this equation which satisfies the asymptotically flatness condition at infinity can be written in the form of a volume integral:

$$U = -G \int \frac{\rho'}{|\vec{r} - \vec{r}'|} dx' dy' dz'. \quad (8.2.2)$$

Furthermore, the vector potential must satisfy the equation $\Delta U_i = 4\pi G\rho v_i$ whose general asymptotically flat solution can be represented as

$$U_i = -G \int \frac{(\rho v_i)'}{|\vec{r} - \vec{r}'|} dx' dy' dz'. \quad (8.2.3)$$

In order to completely determine the metric, it is necessary to calculate the above integrals. Clearly, the result will depend on the internal structure of the body which is determined by the density ρ' and velocity v'_i distributions. Once these functions are given, the calculation of the integrals can be performed in accordance with the detailed formalism developed by Fock [141] and then extended and continued by Abdildin [142] and Brumberg [150]. Introducing spherical coordinates, the resulting metric can be written as

$$ds^2 = \left[c^2 - \frac{2GM}{r} - \kappa \frac{GS_0^2}{c^2 M r^3} (1 - 3 \cos^2 \theta) \right] dt^2 - \left(1 + \frac{2GM}{c^2 r} \right) dr^2 - r^2 (d\theta^2 + \sin^2 \theta d\phi^2) + \frac{4GS_0}{c^2 r} \sin^2 \theta d\phi dt, \quad (8.2.4)$$

where S_0 is the angular momentum of the body, M is the total (effective) mass. Here we added the constant κ and verified that in fact the above metric is an approximate solution for any arbitrary real value of κ . This simple observation allows us to interpret Fock's procedure as a method to find out how the internal structure of the object influences the values of the external parameters. For instance, the total mass in the above metric is M but it can

decomposed as

$$M = m + \frac{\xi}{c^2}, \quad (8.2.5)$$

where m is the rest mass of the body, and ξ is an arbitrary real constant which, as the constant κ , depends on the internal properties of the body. In particular, the cases of a liquid and a solid sphere have been analyzed in detail with the result

$$\xi = \begin{cases} \frac{8}{3}T + \frac{2}{3}\varepsilon, & \text{for a liquid sphere,} \\ 4T + \frac{2}{3}\varepsilon, & \text{for a solid sphere,} \end{cases} \quad \kappa = \begin{cases} \frac{4}{7}, & \text{for a liquid sphere,} \\ \frac{15}{28}, & \text{for a solid sphere.} \end{cases} \quad (8.2.6)$$

where T is the rotational kinetic energy of the body and ε is the energy of mutual gravitational attraction of the particles inside the body. In the case of a static configuration ($S_0 = 0$), the extended metric (8.2.4) reduces to the approximate Schwarzschild metric, where M is the total mass expressed in terms of the internal parameters of the body as given in Eqs.(8.2.5) and (8.2.6). Notice that in this case the field does not depend on the constant κ .

In the general case ($S_0 \neq 0$), the angular momentum of the source generates a gravitational field which, to second order of accuracy in S_0 , depends on the constant κ . This opens the possibility of determining the value of κ by measuring the effects of the gravitomagnetic exterior field on test particles. For planet-like compact objects this effect is quite small. Nevertheless, in the case of test particles in the field of more dense sources it should be possible to perform measurements and determine the value of the parameter κ .

8.3 Matching with the Kerr solution

The Kerr metric [135] in Boyer-Lindquist coordinates [152, 150] can be written as

$$ds^2 = \left(1 - \frac{2\mu\varrho}{\varrho^2 + a^2 \cos^2 \vartheta}\right) c^2 dt^2 - \frac{\varrho^2 + a^2 \cos^2 \vartheta}{\varrho^2 - 2\mu\varrho + a^2} d\varrho^2 - (\varrho^2 + a^2 \cos^2 \vartheta) d\vartheta^2 - \left(\varrho^2 + a^2 + \frac{2\mu\varrho a^2 \sin^2 \vartheta}{\varrho^2 + a^2 \cos^2 \vartheta}\right) \sin^2 \vartheta d\phi^2 - \frac{4\mu\varrho a \sin^2 \vartheta}{\varrho^2 + a^2 \cos^2 \vartheta} cdtd\phi \quad (8.3.1)$$

where

$$\mu = \frac{GM}{c^2}, \quad a = -\frac{S_0}{Mc} \quad (8.3.2)$$

Expanding this metric to the order $\frac{1}{c^2}$, one obtains

$$ds^2 = \left[c^2 - \frac{2GM}{\varrho} + \frac{2GMa^2}{\varrho^3} \cos^2 \vartheta \right] dt^2 - \left(1 + \frac{2GM}{\varrho c^2} - \frac{a^2}{\varrho^2} \sin^2 \vartheta \right) d\varrho^2 - \varrho^2 \left(1 + \frac{a^2}{\varrho^2} \cos^2 \vartheta \right) d\vartheta^2 - \varrho^2 \left(1 + \frac{a^2}{\varrho^2} \right) \sin^2 \vartheta d\phi^2 - \frac{4GMa}{\varrho c} \sin^2 \vartheta d\phi dt. \quad (8.3.3)$$

Furthermore, if we introduce new coordinates $\varrho = \varrho(r, \theta)$, $\vartheta = \vartheta(r, \theta)$ by means of the equations

$$\varrho = r - \frac{a^2 \sin^2 \theta}{2r}, \quad \vartheta = \theta - \frac{a^2 \sin \theta \cos \theta}{2r^2}, \quad (8.3.4)$$

then the Kerr metric (8.3.3) can be reduced to the following form

$$ds^2 = \left[c^2 - 2\frac{GM}{r} - \frac{GS_0^2}{c^2 M r^3} (1 - 3 \cos^2 \theta) \right] dt^2 - \left(1 + \frac{2GM}{c^2 r} \right) dr^2 - r^2 (d\theta^2 + \sin^2 \theta d\phi^2) + \frac{4GS_0}{c^2 r} \sin^2 \theta d\phi dt, \quad (8.3.5)$$

which coincides with the metric (8.2.4) with $\kappa = 1$. Consequently, the extended Fock metric (8.2.4) can be interpreted as describing the exterior field of a rotating body to second order in the angular velocity. The advantage of using Fock's method to derive this approximate solution is that it allows to determine the arbitrary constant κ . In fact, whereas $\kappa = \kappa_L = 4/7$ for a liquid sphere and $\kappa = \kappa_S = 15/28$ for a solid sphere, the value for the Kerr metric $\kappa = \kappa_K = 1$ does not seem to correspond to a concrete internal model. On the other hand, all the attempts to find a physically meaningful interior Kerr solution have been unsuccessful. Perhaps the relationship with Fock's formalism we have established here could shed some light into the structure of the interior counterpart of the Kerr metric.

Furthermore, the coordinate transformation [139]

$$r = R - \frac{a^2}{2R} \left[\left(1 + \frac{2GM}{c^2 R} \right) \left(1 - \frac{GM}{R} \right) + \cos^2 \Theta \left(1 - \frac{2GM}{c^2 R} \right) \left(1 + \frac{3GM}{c^2 R} \right) \right], \quad (8.3.6)$$

$$\theta = \Theta - \frac{a^2}{2R^2} \left(1 + \frac{2GM}{c^2 R} \right) \cos \Theta \sin \Theta, \quad (8.3.7)$$

transforms the approximate Kerr solution into the HT solution (8.1.8) with $J = -\mu a$ and a particular quadrupole parameter $Q = J^2/\mu$.

In this way, we have shown that the extended Fock metric coincides for $\kappa = 1$ with the approximate Kerr solution which, in turn, is equivalent to

the exterior HT solution with a particular value of the quadrupole parameter. The fact that in the Kerr solution the quadrupole moment is completely specified by the angular momentum is an indication that it can be applied only to describe the gravitational field of a particular class of compact objects. A physically meaningful generalization of the Kerr solution should include a set or arbitrary multipole moments which are not completely determined by the angular momentum. In the next section we present a particular exact solution characterized by an arbitrary quadrupole moment.

8.4 The exact Quevedo-Mashhoon metric

In this section we study the general metric describing the gravitational field of a rotating deformed mass found by Quevedo and Mashhoon [8, 136], which is a stationary axisymmetric solution of the vacuum Einstein's equations belonging to the class of Weyl-Lewis-Papapetrou [4, 5, 6]. For the sake of simplicity we consider here a particular solution involving only four parameters: the mass parameter M , the angular momentum parameter a , the quadrupole parameter q , and the additional Zipoy-Voorhees [153, 154] constant δ . For brevity, in this section we use geometric units with $G = c = 1$. The corresponding line element in spheroidal coordinates (t, r, θ, ϕ) with $r \geq \sigma + M_0$, $0 \leq \theta \leq \frac{\pi}{2}$ is given by

$$ds^2 = f(dt - \omega d\phi)^2 - \frac{\sigma^2}{f} \left\{ e^{2\gamma} \left(d\theta^2 + \frac{dr^2}{M_0^2 - 2M_0r + r^2 - \sigma^2} \right) \left(\frac{(M_0 - r)^2}{\sigma^2} - \cos^2 \theta \right) + \left(\frac{(M_0 - r)^2}{\sigma^2} - 1 \right) \sin^2 \theta d\phi^2 \right\}, \quad (8.4.1)$$

where f , ω and γ are functions of r and θ only, and σ is a constant. They have the form $[x = (r - M_0)/\sigma, y = \cos \theta]$

$$f = \frac{R}{L} e^{-2q\delta P_2 Q_2}, \quad (8.4.2)$$

$$\omega = -2a - 2\sigma \frac{\mathfrak{M}}{R} e^{2q\delta P_2 Q_2}, \quad (8.4.3)$$

$$e^{2\gamma} = \frac{1}{4} \left(1 + \frac{M}{\sigma} \right)^2 \frac{R}{(x^2 - 1)^\delta} e^{2\delta^2 \hat{\gamma}}, \quad (8.4.4)$$

where

$$R = a_+ a_- + b_+ b_-, \quad L = a_+^2 + b_+^2, \quad (8.4.5)$$

$$\mathfrak{M} = (x + 1)^{\delta-1} \left[x(1 - y^2)(\lambda + \eta)a_+ + y(x^2 - 1)(1 - \lambda\eta)b_+ \right], \quad (8.4.6)$$

$$\begin{aligned} \hat{\gamma} = \frac{1}{2}(1 + q)^2 \ln \frac{x^2 - 1}{x^2 - y^2} + 2q(1 - P_2)Q_1 + q^2(1 - P_2)[(1 + P_2)(Q_1^2 - Q_2^2) \\ + \frac{1}{2}(x^2 - 1)(2Q_2^2 - 3xQ_1Q_2 + 3Q_0Q_2 - Q_2')]. \end{aligned} \quad (8.4.7)$$

Furthermore

$$a_{\pm} = (x \pm 1)^{\delta-1} [x(1 - \lambda\eta) \pm (1 + \lambda\eta)], \quad (8.4.8)$$

$$b_{\pm} = (x \pm 1)^{\delta-1} [y(\lambda + \eta) \mp (\lambda - \eta)], \quad (8.4.9)$$

with

$$\lambda = \alpha(x^2 - 1)^{\delta-1}(x + y)^{2\delta-2}e^{2q\delta\delta_+}, \quad (8.4.10)$$

$$\eta = \alpha(x^2 - 1)^{\delta-1}(x - y)^{2\delta-2}e^{2q\delta\delta_-}, \quad (8.4.11)$$

$$\delta_{\pm} = \frac{1}{2} \ln \frac{(x \pm y)^2}{x^2 - 1} + \frac{3}{2}(1 - y^2 \mp xy) + \frac{3}{4}[x(1 - y^2) \mp y(x^2 - 1)] \ln \frac{x - 1}{x + 1}, \quad (8.4.12)$$

the quantity α is a constant.

To establish the relationship with the HT solution it is convenient to choose the Zipoy-Voorhees parameter as $\delta = 1 + sq$, where s is a real constant. Then, expanding the metric (8.4.1) to first order in the quadrupole parameter q and to second order in the rotation parameter a , we obtain

$$\begin{aligned} f = 1 - \frac{2M}{r} + \frac{2a^2M \cos^2 \theta}{r^3} + q(1 + s) \left(1 - \frac{2M}{r} \right) \ln \left(1 - \frac{2M}{r} \right) \\ + 3q \left(\frac{r}{2M} - 1 \right) \times \left[\left(1 - \frac{M}{r} \right) (3 \cos^2 \theta - 1) + \left\{ \left(\frac{r}{2M} - 1 \right) (3 \cos^2 \theta - 1) \right. \right. \\ \left. \left. - \frac{M}{r} \sin^2 \theta \right\} \ln \left(1 - \frac{2M}{r} \right) \right], \end{aligned} \quad (8.4.13)$$

$$\omega = \frac{2aMr \sin^2 \theta}{r - 2M}, \quad (8.4.14)$$

$$\begin{aligned} \gamma = \frac{1}{2} \ln \frac{r(r - 2M)}{(r - M)^2 - M^2 \cos^2 \theta} + \frac{a^2}{2} \left[\frac{M^2 \cos^2 \theta \sin^2 \theta}{r(r - 2M)((r - M)^2 - M^2 \cos^2 \theta)} \right] \\ + q(1 + s) \ln \frac{r(r - 2M)}{(r - M)^2 - M^2 \cos^2 \theta} - 3q \left[1 + \frac{1}{2} \left(\frac{r}{M} - 1 \right) \ln \left(1 - \frac{2M}{r} \right) \right] \sin^2 \theta. \end{aligned} \quad (8.4.15)$$

The further simplification $s = -1$, and the coordinate transformation [20]

$$r = R + \mathcal{M}q + \frac{3}{2}\mathcal{M}q \sin^2 \Theta \left[\frac{R}{\mathcal{M}} - 1 + \frac{R^2}{2\mathcal{M}^2} \left(1 - \frac{2\mathcal{M}}{R} \right) \ln \left(1 - \frac{2\mathcal{M}}{R} \right) \right] - \frac{a^2}{2R} \left[\left(1 + \frac{2\mathcal{M}}{R} \right) \left(1 - \frac{\mathcal{M}}{R} \right) - \cos^2 \Theta \left(1 - \frac{2\mathcal{M}}{R} \right) \left(1 + \frac{3\mathcal{M}}{R} \right) \right] \quad (8.4.16)$$

$$\theta = \Theta - \sin \Theta \cos \Theta \left\{ \frac{3}{2}q \left[2 + \left(\frac{R}{\mathcal{M}} - 1 \right) \ln \left(1 - \frac{2\mathcal{M}}{R} \right) \right] + \frac{a^2}{2R} \left(1 + \frac{2\mathcal{M}}{R} \right) \right\} \quad (8.4.17)$$

transforms the approximate QM solution (8.4.13)–(8.4.15) into the HT solution (8.1.8) with parameters

$$\mathcal{M} = M(1 - q), \quad J = -Ma, \quad Q = \frac{J^2}{M} - \frac{4}{5}M^3q. \quad (8.4.18)$$

Introducing units with $G \neq 1$ and $c \neq 1$, in a similar manner, it is also possible to show that choosing $\delta = 1 - q$, and expanding the approximate metric (8.4.13)–(8.4.14) in powers of $1/c^2$, the resulting solution can be made to coincide with Fox’s extended solution (8.2.4). In other words, the parameter κ turns out to be related with the Zipoy-Voorhees parameter δ .

We presented the main exact and approximate solutions of Einstein’s equations which can be used to describe the interior and exterior field of astrophysical compact objects. We found that a particular QM solution, which in general possesses an infinite set of gravitational and electromagnetic multipole moments, contains the exact Kerr metric, as well as the approximate HT and the extended Fock solutions. Moreover, since the HT solution is endowed with its interior counterpart, we conclude that the approximate QM solution (to the second order in the angular momentum and to the first order in the quadrupole parameter) can be matched with the interior HT solution, indicating that it can be used to correctly describe the gravitational field of astrophysical compact objects.

We found that Fock’s formalism can be used to construct models for the inner structure of compact objects from which it is possible to determine the parameters of the exterior approximate solution in terms of the inner parameters. A particular parameter which enters the extended Fock metric turns out to have very specific values in the case of a liquid sphere and a solid sphere. In the case of approximate Kerr metric, this parameter does not seem to correspond to any known interior model analyzed in the framework of Fock’s formalism. This opens the possibility of attacking the problem of finding the interior counterpart of the exterior Kerr metric by using Fock’s method. We expect to investigate this possibility in the near future.

9 Matching with an interior solution

Rather few exact stationary solutions that involve a matter distribution in rotation are to be found in the literature. In particular, the interior solution for the rotating Kerr solution is still unknown. In fact, the quest for a realistic exact solution, representing both the interior and exterior gravitational field generated by a self-gravitating axisymmetric distribution of a perfect fluid mass in stationary rotation is considered as a major problem in general relativity. We believe that the inclusion of a quadrupole in the exterior and in the interior solutions adds a new physical degree of freedom that could be used to search for realistic interior solutions. We will study in this section the entire Riemannian manifold corresponding to the simple case of a static exterior solution with only quadrupole moment.

The simplest generalization of the Schwarzschild spacetime which includes a quadrupole parameter can be obtained from the Zipoy–Voorhees solution with $\delta = 1 - q$. The corresponding line element in spherical-like coordinates can be represented as

$$\begin{aligned}
 ds^2 = & \left(1 - \frac{2m}{r}\right)^{1-q} dt^2 - \left(1 - \frac{2m}{r}\right)^q \\
 & \times \left(1 - \frac{2m}{r}\right)^q \left[\left(1 + \frac{m^2 \sin^2 \theta}{r^2 - 2mr}\right)^{q(2-q)} \left(\frac{dr^2}{1 - \frac{2m}{r}} + r^2 d\theta^2\right) + r^2 \sin^2 \theta d\phi^2 \right].
 \end{aligned} \tag{9.0.1}$$

This solution is axially symmetric and reduces to the spherically symmetric Schwarzschild metric in the limit $q \rightarrow 0$. It is asymptotically flat for any finite values of the parameters m and q . Moreover, in the limiting case $m \rightarrow 0$ it can be shown that the metric is flat. This means that, independently of the value of q , there exists a coordinate transformation that transforms the resulting metric into the Minkowski solution. From a physical point of view this is an important property because it means that the parameter q is related to a genuine mass distribution, i.e., there is no quadrupole moment without mass. To see this explicitly, we calculate the multipole moments of the solution by using the invariant definition proposed by Geroch [18]. The

lowest mass multipole moments M_n , $n = 0, 1, \dots$ are given by

$$M_0 = (1 - q)m, \quad M_2 = \frac{m^3}{3}q(1 - q)(2 - q), \quad (9.0.2)$$

whereas higher moments are proportional to m^3q and can be completely rewritten in terms of M_0 and M_2 . This means that the arbitrary parameters m and q determine the mass and quadrupole which are the only independent multipole moments of the solution. In the limiting case $q = 0$ only the monopole $M_0 = m$ survives, as in the Schwarzschild spacetime. In the limit $m = 0$, with $q \neq 0$, all moments vanish identically, implying that no mass distribution is present and the spacetime must be flat. This is in accordance with the result mentioned above for the metric (9.0.2). Furthermore, notice that all odd multipole moments are zero because the solution possesses an additional reflection symmetry with respect to the equatorial plane.

We conclude that the above metric describes the exterior gravitational field of a static deformed mass. The deformation is described by the quadrupole moment M_2 which is positive for a prolate mass distribution and negative for an oblate one. Notice that in order to avoid the appearance of a negative total mass M_0 the condition $q < 1$ must be satisfied .

9.0.1 Matching conditions

In this subsection we analyze several approaches which could be used to determine the matching hypersurface Σ . Instead of presenting a rigorous analysis, we will present an intuitive method based on the behavior of the curvature and the motion of test particles.

To investigate the structure of possible curvature singularities, we consider the Kretschmann scalar $K = R_{\mu\nu\lambda\tau}R^{\mu\nu\lambda\tau}$. A straightforward computation leads to

$$K = \frac{16m^2(1 - q)^2}{r^{4(2-2q+q^2)}} \frac{(r^2 - 2mr + m^2 \sin^2 \theta)^{2q^2-4q-1}}{(1 - 2m/r)^{2(q^2-q+1)}} L(r, \theta), \quad (9.0.3)$$

with

$$L(r, \theta) = 3(r - 2m + qm)^2(r^2 - 2mr + m^2 \sin^2 \theta) - q(2 - q) \sin^2 \theta [q^2 - 2q + 3(r - m)(r - 2m + qm)]. \quad (9.0.4)$$

In the limiting case $q = 0$, we obtain the Schwarzschild value $K = 48m^2/r^6$ with the only singularity situated at the origin of coordinates $r \rightarrow 0$. In general, one can show that the singularity at the origin, $r = 0$, is present for any values of q . Moreover, an additional singularity appears at the radius $r = 2m$ which, according to the metric (9.0.2), is also a horizon in the sense that the

norm of the timelike Killing tensor vanishes at that radius. Outside the hypersurface $r = 2m$ no additional horizon exists, indicating that the singularities situated at the origin and at $r = 2m$ are naked. Moreover, for values of the quadrupole parameter within the interval

$$q \in \left(1 - \sqrt{3/2}, 1 + \sqrt{3/2}\right) \setminus \{0\} \quad (9.0.5)$$

a singular hypersurface appears at a distance

$$r_{\pm} = m(1 \pm \cos \theta) \quad (9.0.6)$$

from the origin of coordinates. This type of singularity is always contained within the naked singularity situated at the radius $r = 2m$, and is related to a negative total mass M_0 for $q > 1$. Nevertheless, in the interval $q \in (1 - \sqrt{3/2}, 1) \setminus \{0\}$ the singularity is generated by a more realistic source with positive mass.

The analysis of singularities is important to determine the matching hypersurface Σ . Indeed, in the case under consideration it is clear that Σ cannot be situated inside the sphere defined by the radius $r = 2m$. To eliminate all the singularities it is necessary to match the above solution (9.0.2) with an interior solution which covers completely the naked hypersurface $r = 2m$.

Another important aspect related to the presence of naked singularities is the problem of repulsive gravity. In fact, it now seems to be established that naked singularities can appear as the result of a realistic gravitational collapse [155] and that naked singularities can generate repulsive gravity. Currently, there is no invariant definition of repulsive gravity in the context of general relativity, although some attempts have been made by using invariant quantities constructed with the curvature of spacetime [156, 157, 158]. Nevertheless, it is possible to consider an intuitive approach by using the fact that the motion of test particles in stationary axisymmetric gravitational fields reduces to the motion in an effective potential. This is a consequence of the fact that the geodesic equations possess two first integrals associated with stationarity and axial symmetry. The explicit form of the effective potential depends also on the type of motion under consideration.

In the case of a massive test particle moving along a geodesic contained in the equatorial plane ($\theta = \pi/2$) of the Zipoy–Voorhees spacetime (9.0.2), one can show that the effective potential reduces to

$$V_{eff}^2 = \left(1 - \frac{2m}{r}\right)^{1-q} \left[1 + \frac{L^2}{r^2} \left(1 - \frac{2m}{r}\right)^{-q}\right], \quad (9.0.7)$$

where L is constant associated to the angular momentum of the test particle as measured by a static observer at rest at infinity. This expression shows that the behavior of the effective potential strongly depends on the value of the

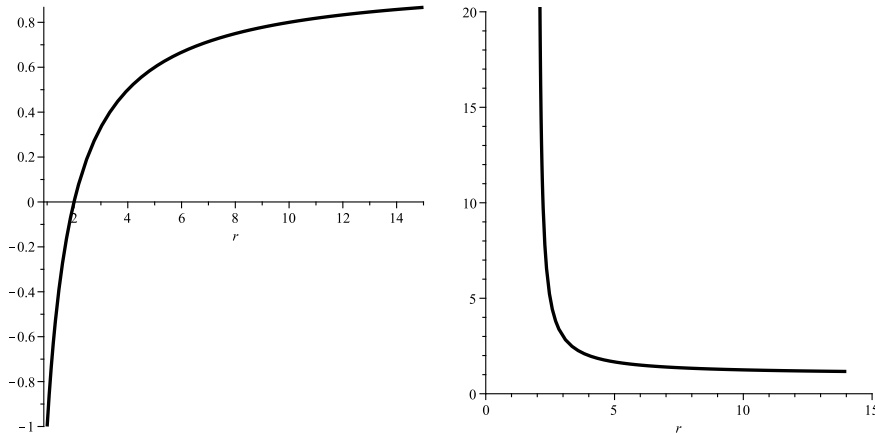


Figure 9.1: The effective potential for the motion of timelike particles. Plot (a) shows the typical behavior of the effective potential of a black hole configuration with $q = 0$. The case of a naked singularity with $q = 1/2$ is depicted in plot (b).

quadrupole parameter q . This behavior is illustrated in Fig. 9.1.

Whereas the effective potential of a black hole corresponds to the typical potential of an attractive field, the effective potential of a naked singularity is characterized by the presence of a barrier which acts on test particles as a source of repulsive gravity. Although this result is very intuitive, the disadvantage of this analysis is that it is not invariant. In fact, a coordinate transformation can be used to arbitrarily change the position of the barrier of repulsive gravity. Moreover, the identification of the spatial coordinate r as a radial coordinate presents certain problems in the case of metrics with quadrupole moments [159]. To avoid this problem we investigate a set of scalars that can be constructed from the curvature tensor and are linear in the parameters that enter the metric, namely, the eigenvalues of the Riemann tensor. Let us recall that the curvature of the Zipoy–Voorhees metric belongs to type I in Petrov’s classification. On the other hand, type I metrics possess three different curvature eigenvalues whose real parts are scalars [160]. The explicit calculation of the curvature eigenvalues for this metric shows [161] that all of them are real and, consequently, they behave as scalars under arbitrary diffeomorphisms. The resulting analytic expressions are rather cumbersome. For this reason we performed a numerical analysis and found out the main differences between black holes and naked singularities. The results are illustrated in Fig. 9.2.

We took a particular eigenvalue which represents the qualitative behavior of all the eigenvalues. In the case of a black hole, the eigenvalue diverges near the origin of coordinates, where the curvature singularity is situated, and it decreases rapidly as r increases, tending to zero at spatial infinity. In the case of a naked singularity the situation changes drastically. The eigenvalue vanishes at spatial infinity and then increases as the value of the radial coordinate

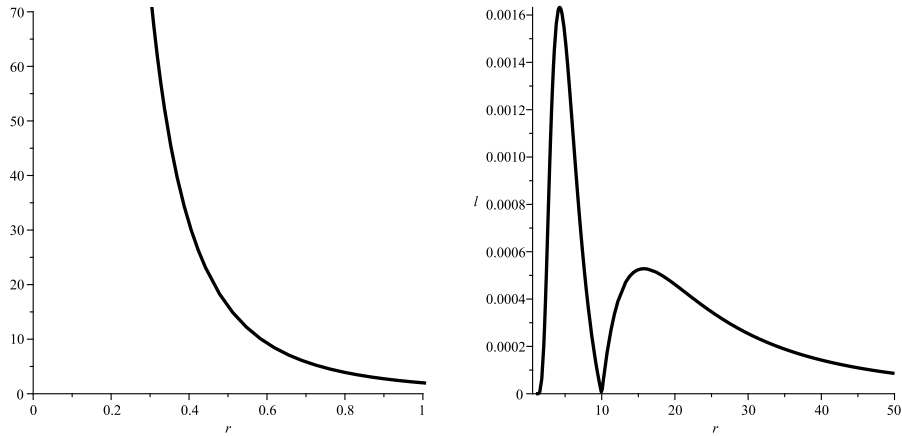


Figure 9.2: Behavior of the curvature eigenvalue on the equatorial plane ($\theta = \pi/2$) of the Zipoy-Voorhees metric. Plot (a) corresponds to a black hole solution with $q = 0$. Plot (b) illustrates the behavior in case of a naked singularity with $q = -2$.

decreases. At a specific radius $r = r_{min}$, the eigenvalue reaches a local maximum and then rapidly decreases until it vanishes. This oscillatory behavior becomes more frequent as the origin of coordinates is approached. It seems plausible to interpret this peculiar behavior as an invariant manifestation of the presence of repulsive gravity. On the other hand, if one would like to avoid the effects of repulsive gravity, one would propose r_{min} as the minimum radius where the matching with an interior solution should be carried out. If we denote the eigenvalue as λ , then r_{min} can be defined invariantly by means of the equation

$$\left. \frac{\partial \lambda}{\partial r} \right|_{r=r_{min}} = 0. \quad (9.0.8)$$

Then, the radius r_{min} determines the matching hypersurface Σ and one could interpret condition (9.0.8) as a C^3 -matching condition. In concrete cases, one must calculate all possible eigenvalues λ_i and all possible points satisfying the matching condition $\partial \lambda_i / \partial r = 0$. The radius r_{min} corresponds then to the first extremum that can be found when approaching the origin of coordinates from infinity. In the next section we will show that this approach can be successfully carried out in the case of the Zipoy-Voorhees metric.

9.0.2 An interior solution

In the search for an interior solution that could be matched to the exterior solution with quadrupole moment given in Eq.(9.0.2), we found that an ap-

proprate form of the line element can be written as

$$ds^2 = f dt^2 - \frac{e^{2\gamma_0}}{f} \left(\frac{dr^2}{h} + d\theta^2 \right) - \frac{\mu^2}{f} d\phi^2, \quad (9.0.9)$$

where

$$e^{2\gamma_0} = (r^2 - 2mr + m^2 \cos^2 \theta) e^{2\gamma(r,\theta)}, \quad (9.0.10)$$

and $f = f(r, \theta)$, $h = h(r)$, and $\mu = \mu(r, \theta)$. This line element preserves axial symmetry and staticity.

The inner structure of the mass distribution with a quadrupole moment can be described by a perfect fluid energy–momentum tensor. In general, in order to solve Einstein’s equations completely, pressure and energy must be functions of the coordinates r and θ . However, if we assume that $\rho = \text{const}$, the resulting system of differential equations is still compatible. The assumption of constant density drastically reduces the complexity of the problem. Then, the corresponding field equations reduce to

$$p_r = -\frac{1}{2}(p + \rho) \frac{f_r}{f}, \quad p_\theta = -\frac{1}{2}(p + \rho) \frac{f_\theta}{f}, \quad (9.0.11)$$

$$\mu_{rr} = -\frac{1}{2h} \left(2\mu_{\theta\theta} + h_r \mu_r - 32\pi p \frac{\mu e^{2\gamma_0}}{f} \right), \quad (9.0.12)$$

$$f_{rr} = \frac{f_r^2}{f} - \left(\frac{h_r}{2h} + \frac{\mu_r}{\mu} \right) f_r + \frac{f_\theta^2}{hf} - \frac{\mu_\theta f_\theta}{\mu h} - \frac{f_{\theta\theta}}{h} + 8\pi \frac{(3p + \rho) e^{2\gamma_0}}{h}. \quad (9.0.13)$$

Moreover, the function γ turns out to be determined by a set of two partial differential equations which can be integrated by quadratures once f and μ are known. The integrability condition of these partial differential equations turns out to be satisfied identically by virtue of the remaining field equations.

Although we have imposed several physical conditions which simplify the form of the field equations, we were unable to find analytic solutions. However, it is possible to perform a numerical integration by imposing appropriate initial conditions. In particular, we demand that the metric functions and the pressure are finite at the axis. Then, it is possible to plot all the metric functions and thermodynamic variables. In particular, the pressure behaves as shown in Fig.9.3.

It can be seen that the pressure is finite in the entire interior domain, and tends to zero at certain hypersurface $R(r, \theta)$ which depends on the initial value of the pressure on the axis. Incidentally, it turns out that by increasing the value of the pressure on the axis, the “radius fuction” $R(r, \theta)$ can be reduced. Furthermore, if we demand that the hypersurface $R(r, \theta)$ coincides with the origin of coordinates, the value of the pressure at that point diverges. From a physical point of view, this is exactly the behavior that is expected from a physically meaningful pressure function.

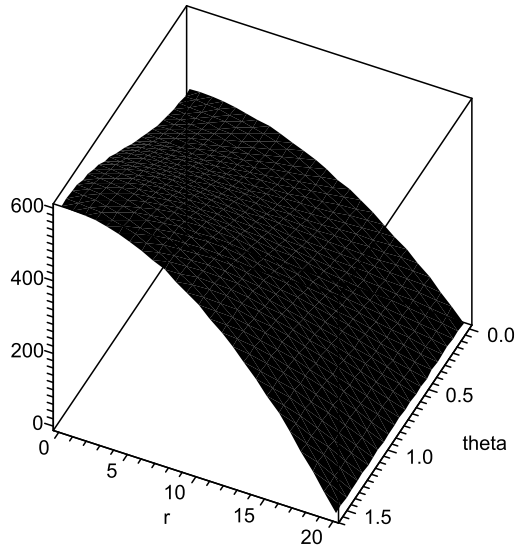


Figure 9.3: Plot of the inner pressure as a function of the spatial coordinates.

This solution can be used to calculate numerically the corresponding Riemann tensor and its eigenvalues. As a result we obtain that the solution is free of singularities in the entire region contained within the radius function $R(r, \theta)$. In particular, one of the eigenvalues presents on the equatorial plane the behavior depicted in Fig.9.4. All the eigenvalues have a finite value at the symmetry axis and decrease as the boundary surface is approached.

To apply the C^3 -matching procedure proposed above we compare the behavior of the eigenvalue plotted in Fig.9.2 with the corresponding eigenvalue plotted in Fig.9.4, using the same scale in both graphics. The result is illustrated in Fig.9.5. It then becomes clear that the first possible point where the matching can be performed is exactly at r_{min} which in this particular case corresponds to $r_{min} \approx 5M_0$. This fixes the initial value of the pressure on the axis which is then used to attack the problem of matching the interior and exterior metric functions. In all the cases we analyzed, we obtained a reasonable matching, with the accuracy of the numerical calculations. We repeated the same procedure for different values of the angular coordinate ($\theta = \pi/4$ and $\theta = 0$), and obtained that the matching can always be reached by fixing in an appropriate manner the arbitrary constants that enter the metric functions f and μ .

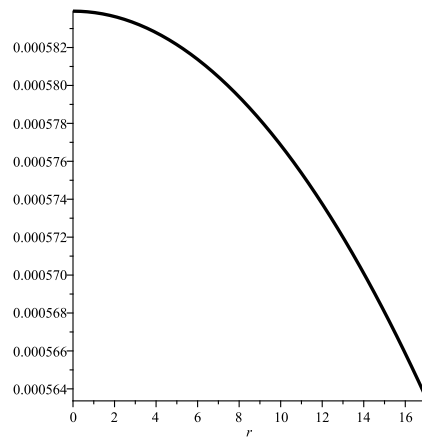


Figure 9.4: Behavior of the curvature eigenvalue on the equatorial plane ($\theta = \pi/2$) of the interior solution.

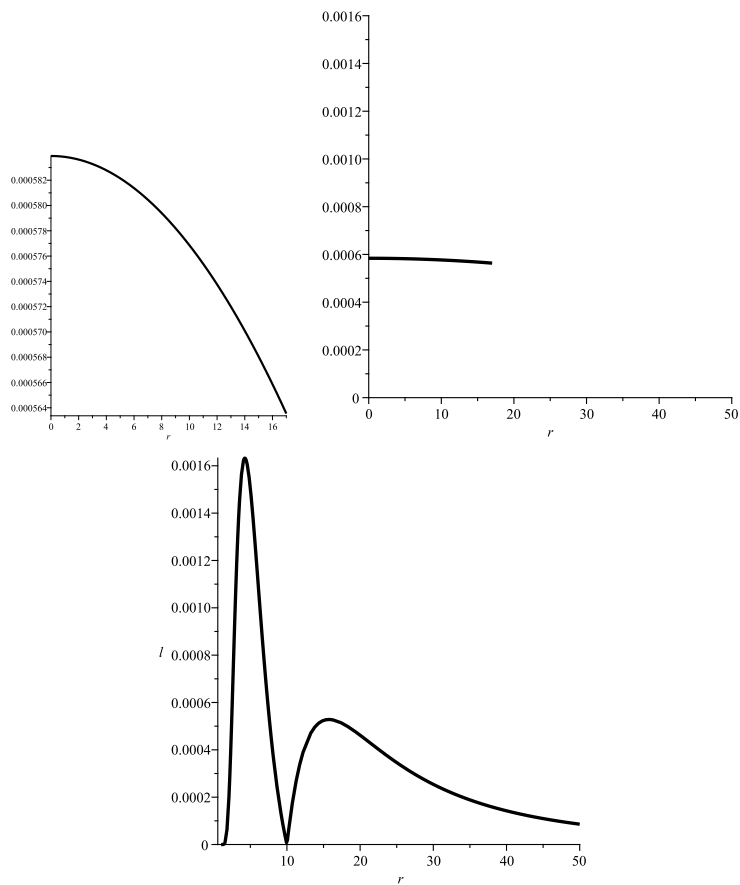


Figure 9.5: Curvature eigenvalues of the interior solution and of the exterior solution with the same scale.

9.1 Concluding remarks

We presented an exact electrovacuum solution of Einstein-Maxwell equations which contains four different sets of multipole moments. An invariant calculation shows that they can be interpreted as the gravitoelectric, gravitomagnetic, electric and magnetic multipole moments. The solution is asymptotically flat and is free of singularities in a region situated around the origin of coordinates. The rotating Kerr metric is contained as a special case. The NUT parameter can also be included by a suitable choice of the arbitrary constants which enter the Ernst potentials. We conclude that this solution can be used to describe the exterior gravitational field a charged rotating mass distribution.

In the particular case of slowly rotating and slightly deformed mass distribution we obtained the explicit form of the metric, and showed that it can be matched with an interior solution which is contained within the class of Hartle-Thorne solutions. This reinforces the conclusion that the solution represents the interior as well as the exterior gravitational field of astrophysical compact objects.

We studied the problem of matching the interior and exterior spacetimes. We propose a C^3 -matching which consists in demanding that the derivatives of a particular curvature eigenvalue are smooth on the matching hypersurface. To prove the validity of this approach we derived an interior solution for the simplest case of a static mass with an arbitrary quadrupole moment, represented by the Zipoy-Voorhees vacuum solution. The numerical integration of the corresponding field equations shows that interior perfect fluid solutions exist which are characterized by a constant density profile with a variable pressure. Fixing the value of the angular coordinate θ , we performed numerically the C^3 -matching. As a result we obtain a minimum radius at which the matching can be carried out and a fixed value for the pressure on the symmetry axis. These values are then used to reach the smooth matching of the interior and exterior metric functions. In all the cases analyzed in this manner we obtained a reasonable numerical matching.

The idea of using the C^3 -matching condition to determine the minimum radius, at which an interior solution can be matched with an exterior one, has been proved also in a particular case where analytical methods can be applied, namely, in the case of the Kerr-Newman class of solutions. The obtained results are reasonable and compatible with other results obtained by analyzing the motion of test particles [162]. These results indicate that it should be possible to determine the minimum radius of an astrophysical compact object by using the idea of the C^3 -matching presented here. To prove this conjecture in general, it will be necessary to use more powerful methods related to the mathematical behavior of geodesics and curvature. This problem is currently under investigation [163]. An important application of this analysis would be to relate the minimum size of a compact object

with its binding energy. As a result we would obtain the maximum binding energy which is physically allowed for an astrophysical compact object.

Bibliography

- [1] H. Stephani, D. Kramer, M. MacCallum, C. Hoenselaers, and E. Herlt, *Exact solutions of Einstein's field equations*, Cambridge University Press, Cambridge UK, 2003.
- [2] F. J. Ernst, *New formulation of the axially symmetric gravitational field problem*, *Phys. Rev.* **167** (1968) 1175; F. J. Ernst, *New Formulation of the axially symmetric gravitational field problem II* *Phys. Rev.* **168** (1968) 1415.
- [3] H. Quevedo and B. Mashhoon, *Exterior gravitational field of a rotating deformed mass*, *Phys. Lett. A* **109** (1985) 13; H. Quevedo, *Class of stationary axisymmetric solutions of Einstein's equations in empty space*, *Phys. Rev. D* **33** (1986) 324; H. Quevedo and B. Mashhoon, *Exterior gravitational field of a charged rotating mass with arbitrary quadrupole moment*, *Phys. Lett. A* **148** (1990) 149; H. Quevedo, *Multipole Moments in General Relativity - Static and Stationary Solutions-*, *Fort. Phys.* **38** (1990) 733; H. Quevedo and B. Mashhoon *Generalization of Kerr spacetime*, *Phys. Rev. D* **43** (1991) 3902.
- [4] H. Weyl, *Zur Gravitationstheorie*, *Ann. Physik (Leipzig)* **54** (1917) 117.
- [5] T. Lewis, *Some special solutions of the equations of axially symmetric gravitational fields*, *Proc. Roy. Soc. London* **136** (1932) 176.
- [6] A. Papapetrou, *Eine rotationssymmetrische Lösung in der Allgemeinen Relativitätstheorie*, *Ann. Physik (Leipzig)* **12** (1953) 309.
- [7] F. J. Hernandez, F. Nettel, and H. Quevedo, *Gravitational fields as generalized string models*, *Grav. Cosmol.* **15**, 109 (2009).
- [8] H. Quevedo, *General Static Axisymmetric Solution of Einstein's Vacuum Field Equations in Prolate Spheroidal Coordinates*, *Phys. Rev. D* **39**, 2904–2911 (1989).
- [9] G. Erez and N. Rosen, *Bull. Res. Council. Israel* **8**, 47 (1959).
- [10] B. K. Harrison, *Phys. Rev. Lett.* **41**, 1197 (1978).
- [11] H. Quevedo, *Generating Solutions of the Einstein–Maxwell Equations with Prescribed Physical Properties*, *Phys. Rev. D* **45**, 1174–1177 (1992).

- [12] W. Dietz and C. Hoenselaers, *Solutions of Einstein's equations: Techniques and results*, (Springer Verlag, Berlin, 1984).
- [13] V. A. Belinski and V. E. Zakharov, *Soviet Phys. – JETP*, **50**, 1 (1979).
- [14] C. W. Misner, *Harmonic maps as models for physical theories*, *Phys. Rev. D* **18** (1978) 4510.
- [15] D. Korotkin and H. Nicolai, *Separation of variables and Hamiltonian formulation for the Ernst equation*, *Phys. Rev. Lett.* **74** (1995) 1272.
- [16] J. Polchinski, *String Theory: An introduction to the bosonic string*, Cambridge University Press, Cambridge, UK, 2001.
- [17] D. Nuñez, H. Quevedo and A. Sánchez, *Einstein's equations as functional geodesics*, *Rev. Mex. Phys.* **44** (1998) 440; J. Cortez, D. Nuñez, and H. Quevedo, *Gravitational fields and nonlinear sigma models*, *Int. J. Theor. Phys.* **40** (2001) 251.
- [18] R. Geroch, *J. Math. Phys.* **11**, 2580 (1970).
- [19] R. O. Hansen, *J. Math. Phys.* **15**, 46 (1974).
- [20] D. Bini, A. Geralico, O. Luongo, and H. Quevedo, *Generalized Kerr space-time with an arbitrary quadrupole moment: Geometric properties vs particle motion*, *Class. Quantum Grav.* **26**, 225006 (2009).
- [21] S. Chandrasekhar, *The Mathematical Theory of Black Holes*, Oxford University Press, New York, 1983.
- [22] J. Levin and G. Perez-Giz, *Phys. Rev. D* **77** (2008) 103005.
- [23] N. Bilic, *PoS P2GC* (2006) 004 [arXiv:astro-ph/0610657].
- [24] S. Grunau and V. Kagramanova, *Phys. Rev. D* **83** (2011) 044009 [arXiv:1011.5399 [gr-qc]].
- [25] E. Hackmann, V. Kagramanova, J. Kunz, and C. Lammerzahl, *Phys. Rev. D* **78**, 124018 (2008).
- [26] V. Kagramanova, J. Kunz, E. Hackmann, and C. Lammerzahl, *Phys. Rev. D* **81**, 124044 (2010).
- [27] E. Hackmann, C. Lammerzahl, V. Kagramanova, and J. Kunz, *Phys. Rev. D* **81**, 044020 (2010).
- [28] E. Hackmann, V. Kagramanova, J. Kunz, and C. Lammerzahl, *Europhys. Lett.* **88**, 30008 (2009).

-
- [29] E. Belbruno and F. Pretorius, arXiv:1103.0585 [gr-qc].
- [30] L. Barack and N. Sago, Phys. Rev. D **83** (2011) 084023.
- [31] D. Pugliese, H. Quevedo and R. Ruffini, Phys. Rev. D **83**, 024021 (2011)
- [32] D. Pugliese, H. Quevedo and R. Ruffini, arXiv:1003.2687 [gr-qc].
- [33] K. S. Virbhadra and G. F. R. Ellis, Phys. Rev. D **65** (2002) 103004.
- [34] K. S. Virbhadra and C. R. Keeton, Phys. Rev. D **77** (2008) 124014 [arXiv:0710.2333 [gr-qc]].
- [35] M. P. Dabrowski, J. Osarczuk, Astroph. Space Sci. 229, 139 (1995).
- [36] M. P. Dabrowski and I. Prochnicka, Phys. Rev. D **66** (2002) 043508 [arXiv:hep-th/0201180].
- [37] V. D. Gladush and M. V. Galadgyi, Kinematics and Physics of Celestial Bodies, 2009, Vol. 25, No. 2, pp. 79-88.
- [38] W. B. Bonnor Class. Quantum Grav. 10 (1993) 2077-2082.
- [39] D. Bini, A. Geralico and R. Ruffini, Phys. Rev. D **75** (2007) 044012.
- [40] D. Bini, A. Geralico and R. Ruffini, Phys. Rev. D **77** (2008) 064020.
- [41] D. Bini, A. Geralico and R. Ruffini, Phys. Lett. A **360** (2007) 515.
- [42] D. Bini, A. Geralico and F. de Felice, Int. J. Mod. Phys. D **14** (2005) 1793.
- [43] P. Pradhan and P. Majumdar, Phys. Lett. A **375** (2011) 474 [arXiv:1001.0359 [gr-qc]].
- [44] V. D. Gladush and M. V. Galadgyi, arXiv:1011.0843 [gr-qc]. DOI: 10.1007/s10714-010-1119-9
- [45] M. Olivares, J. Saavedra, C. Leiva and J. R. Villanueva, arXiv:1101.0748 [gr-qc].
- [46] O. B. Zaslavskii, JETP Lett. **92** (2010) 571 [Pisma Zh. Eksp. Teor. Fiz. **92** (2010) 635] [arXiv:1007.4598 [gr-qc]], DOI :10.1134/S0021364010210010.
- [47] Ragab M. Gad, Astrophysics and Space Science, Vol.330, Issue 1, pp.107-114, 2010Ap SS.330..107G
- [48] G. Dotti and R. J. Gleiser, Class. Quant. Grav. **27** (2010) 185007 [arXiv:1001.0152 [gr-qc]].

- [49] F. de Felice, 1995, *Class. Quantum Grav.* **12**, 1119.
- [50] P. S. Joshi, *Gravitational Collapse and Spacetime Singularities*, (Cambridge Monographs on Mathematical Physics., 2007).
- [51] V. A. Belinski, M. Pizzi and A. Paolino, *AIP Conf. Proc.* **1059** (2008) 3.
- [52] O. Luongo and H. Quevedo, in *Proceedings of MG12, Marcel Grossman Meeting* (to be published).
- [53] M. Pizzi and A. Paolino, *Int. J. Mod. Phys. D* **18** 1955 (2009).
- [54] V. Belinski, M. Pizzi and A. Paolino, *Int. J. Mod. Phys. D* **18** 513 (2009).
- [55] M. Pizzi and A. Paolino, *Int. J. Mod. Phys. A* **23** (2008) 1222.
- [56] A. Paolino and M. Pizzi, *Int. J. Mod. Phys. D* **17** (2008) 1159.
- [57] V. S. Manko, *Phys. Rev. D* **76** (2007) 124032 [arXiv:0710.2158 [gr-qc]].
- [58] G. A. Alekseev and V. A. Belinski, arXiv:0710.2515 [gr-qc].
- [59] G. Preti and F. d. Felice, *Am. J. Phys.* **76** (2008) 671.
- [60] F. de Felice, *Nuovo Cim. B* **122**, 481 (2007).
- [61] A.N. Aliev, ICTP-report, Trieste, Italy, April 1992.
- [62] J. M. Cohen and R. Gautreau, *Phys. Rev. D* **19** (1979) 2273.
- [63] E. P. T. Liang, *Phys. Rev. D* **9** (1974) 3257.
- [64] M. Patil and P. S. Joshi, *Phys. Rev. D* **82** (2010) 104049 [arXiv:1011.5550 [gr-qc]].
- [65] M. Patil, P. S. Joshi and D. Malafarina, *Malafarina, Phys. Rev.* **83**, (2011) 064007.
- [66] A. Qadir and A. A. Siddiqui, *Int. J. Mod. Phys. D* **16** (2007) 25.
- [67] F. Belgiorno, M. Martellini and M. Baldicchi, *Phys. Rev. D* **62** (2000) 084014.
- [68] Z. Kovacs and T. Harko, *Phys. Rev. D* **82** (2010) 124047 [arXiv:1011.4127 [gr-qc]].
- [69] F. D. Lora-Clavijo, P. A. Ospina-Henao and J. F. Pedraza, *Phys. Rev. D* **82** (2010) 084005.
- [70] D. Vogt and P. S. Letelier, *Phys. Rev. D* **70** (2004) 064003.

-
- [71] H. Quevedo, *Gen. Rel. Grav.* **43** (2011) 1141.
- [72] H. Quevedo, arXiv:1012.4030 [gr-qc].
- [73] D. J. Raine, E. Thomas, *Black holes: an introduction*, Imperial College Press, 2010.
- [74] M. P. Hobson, G. P. Efstathiou and A. N. Lasenby, *General Relativity An Introduction for Physicists* Cambridge University Press, 2006.
- [75] J. M. Bardeen, *Nature* **226** (1970) 64.
- [76] J. M. Bardeen, W. H. Press and S. A. Teukolsky, *Astrophys. J.* **178** (1972) 347.
- [77] I. Bredberg, C. Keeler, V. Lysov and A. Strominger, arXiv:1103.2355 [hep-th].
- [78] Z. Stuchlik, *Bull. Astron. Inst. Czechosl.* **31** (1980), 129-144.
- [79] C. Misner, K. Thorne, J. Wheeler, *Gravitation*, Freeman and Company, 1973.
- [80] R. Ruffini, *On the Energetics of Black Holes, Le Astres Occlus* (Les Houches 1972).
- [81] D. Pugliese, H. Quevedo and R. Ruffini, *Phys. Rev. D* **83** (2011) 104052.
- [82] S. Chandrasekhar, *Principles of Stellar Dynamics* (Dover Publications, New York, 1942).
- [83] V. Balek, J. Bicak, Z. Stuchlik *Bull. Astron. Inst. Czechosl.* **40** (1989), 133-165 Publishing House of the Czechoslovak Academy of Sciences.
- [84] D. Bini, R. T. Jantzen *Class. Quantum Grav.* **17** (2000) 16371647.
- [85] P. G. Komorowski, S. R. Valluri and M. Houde, *Class. Quant. Grav.* **26** (2009) 085001.
- [86] P. G. Komorowski, S. R. Valluri and M. Houde, *Class. Quant. Grav.* **27** (2010) 225023.
- [87] P. G. Komorowski, S. R. Valluri and M. Houde, arXiv:1101.0996 [gr-qc].
- [88] E. Hackmann, V. Kagramanova, J. Kunz and C. Lammerzahl, *Europhys. Lett.* **88**, 30008 (2009).
- [89] M. Favata, *Phys. Rev. D* **83** (2011) 024028.

- [90] D. Bini, C. Cherubini, G. Cruciani and R. T. Jantzen, *Int. J. Mod. Phys. D* **13** (2004) 1771.
- [91] D. Bini, P. Carini and R. T. Jantzen, *Int. J. Mod. Phys. D* **6** (1997) 143.
- [92] D. Bini, C. Cherubini, A. Geralico, R. T. Jantzen, *Gen. Rel. Grav.* (2008) 40:9851012.
- [93] F. De Felice and M. Calvani, *Nuovo Cim. B* **10** (1972) 447.
- [94] F. De Felice, *Phys. Rev. D* **19** (1979) 451.
- [95] J. Gariel, M. A. H. MacCallum, G. Marcilhacyand N. O. Santos, arXiv:gr-qc/0702123.
- [96] C. Chicone and B. Mashhoon, *Class. Quant. Grav.* **23** (2006) 4021.
- [97] K. Lake, *Phys. Rev. Lett.* **104** (2010) 211102 [Erratum-*ibid.* **104** (2010) 259903].
- [98] E. Hackmann, C. Lammerzahl, V. Kagramanovaand J. Kunz, *Phys. Rev. D* **81** (2010) 044020.
- [99] D. Bini, F. de Felice and A. Geralico, *Class. Quant. Grav.* **21** (2004) 5427.
- [100] D. Bini, F. de Felice and A. Geralico, *Class. Quant. Grav.* **21** (2004) 5441.
- [101] D. Bini, A. Geralico and R. T. Jantzen, *Class. Quant. Grav.* **22** (2005) 4729.
- [102] D. Bini, A. Geralico, R. T. Jantzen and F. de Felice, *Class. Quant. Grav.* **23** (2006) 3287.
- [103] V. I. Dokuchaev, arXiv:1103.6140 [gr-qc].
- [104] S. Suzuki and K. Maeda *Phys. Rev. D* **58**, 023005 (1998).
- [105] G. A. Gonzalez and F. Lopez-Suspes, arXiv:1104.0346 [gr-qc].
- [106] P. Pani, E. Barausse, E. Berti and V. Cardoso, *Phys. Rev. D* **82** (2010) 044009.
- [107] D. Grumiller and A. M. Piso, arXiv:0909.2041 [astro-ph.SR].
- [108] F. de Felice and Bradley, M., 1988, *Class. Quantum Grav.* **5**, 1577.
- [109] J. M. Bardeen, *Astrophys. J.* **161**, 103 (1970).
- [110] A. Palit, A. Pachenko, N. G. Migranov, A. Bhadra, and K. K. Nandi, *Int. J. Theor. Phys.* **48** (2009) 1271.

-
- [111] P. S. Letelier, *Phys. Rev. D* **68** (2003) 104002.
- [112] J. Ramos-Caro, J. F. Pedraza, and P. S. Letelier, *Mon. Not. R. Astron. Soc.* **413** (2011) 3105.
- [113] K. P. Tod, F. de Felice and M. Calvani, *Nuovo Cim. B* **34** (1976) 365.
- [114] S. W. Wei, Y. X. Liu, H. Guo and C. E. Fu, arXiv:1006.1056 [hep-th].
- [115] A. A. Grib and Y. V. Pavlov, arXiv:1007.3222 [gr-qc].
- [116] E. Berti, F. White, A. Maniopolou and M. Bruni 2005 *Mon. Not. R. Astron. Soc.* **358**, 923-938
- [117] D. Bini, A. Geralico, O. Luongo and H. Quevedo, *Class. Quant. Grav.* **26** (2009) 225006.
- [118] T. Harada and M. Kimura, arXiv:1010.0962 [gr-qc].
- [119] T. Harada and M. Kimura, arXiv:1102.3316 [gr-qc].
- [120] S. Capozziello, M. De Laurentis and A. Stabile, *Class. Quant. Grav.* **27**, 165008 (2010).
- [121] T. Ledvinka, M. Zofka and J. Bicak, arXiv:gr-qc/9801053.
- [122] C. Bambi and N. Yoshida, *Phys. Rev. D* **82** (2010) 124037.
- [123] V. Zhuravlev and P. Ivanov, arXiv:1103.5739.
- [124] D. R. Staicova and P. P. Fiziev, *Astrophys. Space Sci.* **332** (2011)385.
- [125] F. Tamburini, B. Thide, G. Molina-Terriza and G. Anzolin, *Nature Phys.* **7** (2011) 195.
- [126] R. Penrose: *Nuovo Cimento B* 1 (1969) 252.
- [127] S. W. Hawking and G. F. R. Ellis, *Cambridge University Press, Cambridge*, 1973.
- [128] M. Patil and P. S. Joshi, arXiv:1103.1082 [gr-qc].
- [129] P. S. Joshi, D. Malafarina and R. Narayan, arXiv:1106.5438 [gr-qc].
- [130] P. S. Joshi and D. Malafarina, arXiv:1105.4336 [gr-qc].
- [131] M. Patil and P. S. Joshi, arXiv:1103.1083 [gr-qc].
- [132] R. Di Criscienzo, L. Vanzo and S. Zerbini, *JHEP* **1005** (2010) 092.
- [133] K. Schwarzschild, *Sitzungsber. d. Preub. Akad.d.Wissensch.*, 18 (1916).

- [134] H. Thirring and J. Lense, *Z. Phys.* **19**, 156 (1918).
- [135] R. P. Kerr, *Phys. Rev. Letters*, **11**, 237 (1963).
- [136] H. Quevedo and B. Mashhoon, *Phys. Rev. D* **43**, 3902 (1991).
- [137] S. Stergioulas, *Living Rev.* **7**, (2004).
- [138] J. B. Hartle, *Astr. J.* **150**, 1005 (1967).
- [139] J. B. Hartle and K. S. Thorne, *Astr. J.* **150**, 1005 (1967); 1967 *Astr. J.* **153**, 807 (1968).
- [140] K. S. Thorne 1967 in *Houtes energies en astrophysique*, Vol. 3, ed. C. DeWitt, E. Schatzman, and P. Veron (New York: Gordon and Breach).
- [141] V. A. Fock, *Theory of space, time and gravitation*, (Pergamon Press, London, U.K., 1959)
- [142] M. M. Abdildin, *On rotating liquid sphere metric: Questions of field theory* (Alma-Ata University, 1985)
- [143] J. Hartle, and D. Sharp, *Ap.J.*, **147**, 317 (1967).
- [144] A. Papapetrou, *Proc. Roy. Irish Acad.* **52**, 11 (1948).
- [145] J. B. Hartle and D. H. Sharp, *Ap. J.*, **147**, 317 (1967).
- [146] J. Ehlers, *Frame theory* (Springer Verlag, Berlin, 1974)
- [147] M. M. Abdildin, *Mechanics of Einstein gravitation theory* (Alma-Ata University, 1988)
- [148] De Donder *La gravifique einsteinienne* (Paris, 1921)
- [149] K. Lanczos. *Phys.ZS.* **23**, 537 (1923).
- [150] V. A. Brumberg, *Essential Relativistic Celestial Mechanics* (Adam Hilger, Bristol, UK, 1991).
- [151] M. M. Abdildin *Bodies motion problem in General Relativity* (Alma-Ata University, 1994)
- [152] R. H. Boyer and R. W. Lindquist, *J. Math. Phys.* **8**, 265 (1967).
- [153] D. M. Zipoy, *J. Math. Phys.* **7**, 1137 (1966).
- [154] B. Voorhees, *Phys. Rev. D* **2**, 2119 (1970).
- [155] P. S. Joshi, *Gravitational Collapse and Spacetime Singularities* (Cambridge University Press, Cambridge, 2007).

- [156] F. de Felice, *Repulsive gravity and curvature invariants in general relativity*, Ann. de Phys. **14**, 79 (1989).
- [157] G. Preti and F. de Felice, *Light cones and repulsive gravity*, Am. J. Phys. **76**, 671 (2008).
- [158] C. Cherubini, D. Bini, S. Capozziello, and R. Ruffini, *Second order scalar invariants of the Riemann tensor: Applications to black hole space-times*, Int. J. Mod. Phys. D **11**, 827 (2002).
- [159] Ya. V. Zeldovich and I. D. Novikov, *Relativistic Astrophysics* (University of Chicago Press, Chicago, 1971).
- [160] P. Jordan, J. Ehlers and W. Kundt, Akad. Wiss. Main. Abh. Math.-Nat. (1960); see also Ref.[1].
- [161] H. Quevedo, *Multipole moments in general relativity - Static and stationary solutions -*, Forts. Phys. **38**, 733 (1990).
- [162] O. Luongo and H. Quevedo, *Toward an invariant definition of repulsive gravity*, in Proceedings of the 12-th Marcel Grossman Meeting on General Relativity and Gravitation (2010).
- [163] R. P. Kerr, H. Quevedo, and R. Ruffini, *On the minimum size of astrophysical compact objects*, in preparation